UNIVERSITY OF OKLAHOMA

GRADUATE COLLEGE

SIMULATION OF POLARIMETRIC PHASED ARRAY WEATHER RADARS

A THESIS

SUBMITTED TO THE GRADUATE FACULTY

in partial fulfillment of the requirements for the

Degree of

MASTER OF SCIENCE

By

ANDREW DAVID BYRD
Norman, Oklahoma
2016

SIMULATION OF POLARIMETRIC PHASED ARRAY WEATHER RADARS

A THESIS APPROVED FOR THE
SCHOOL OF ELECTRICAL AND COMPUTER ENGINEERING

BY

Dr. Robert D. Palmer, Chair

Dr. Bradley M. Isom

Dr. Igor R. Ivić

Dr. Tian-You Yu

Dr. Mark B. Yeary

Acknowledgements

First, I would like to thank my advisors, Dr. Robert Palmer, Dr. Bradley Isom, and Dr. Igor Ivić, for their exceptional guidance and mentorship in the completion of this thesis. Thanks as well to Dr. Mark Yeary and Dr. Tian-You Yu for making available their time and effort in order to serve as members of my committee. Thanks to Dr. Boon-Leng Cheong, for providing the source code that served as the foundation for the software developed for this work, and to Dr. Alexander Schenkman for furnishing the ARPS data that gave my simulated radars something to look at. Thanks also to Dr. Caleb Fulton for his constant willingness to make his expert advice available in service of this thesis. Finally, enormous gratitude is due to my mother, Janet Byrd, whose love and support have been instrumental to all of my successes, and to Suzanne Cisneros, whose presence at my side has made the completion of this work a considerably lighter burden.

This work was supported by the NOAA National Severe Storms Laboratory under Cooperative Agreement NA11OAR4320072.

Table of Contents

List Of Tables

List Of Figures

Abstract

Polarimetric phased array radars (PPARs) are a rapidly developing area of research interest in weather radar. However, they present intrinsic challenges for calibration and operation. Foremost among these are the adverse effects of copolar radiation pattern mismatch as well as cross-polar fields on polarimetric measurement accuracy. Characterization of the impact these effects have on weather radar observations and the effectiveness of proposed methods for mitigation of those impacts can be time-consuming and costly if conducted using radar hardware. Furthermore, few operational PPARs exist to serve as testbeds. Alternatively, the effects of copolar and cross-polar fields can be studied using numerical simulations. In that regard, this work outlines a simulation method that allows for the characterization of PPAR performance and the prototyping of techniques to mitigate cross-polar biases. To achieve this, a simulation volume is populated by thousands of scattering centers, whose movement and scattering characteristics at any point in space and time are governed by a high-resolution numerical weather prediction model. Each of these scattering centers has its own individually calculated Doppler spectrum in both the horizontal (H) and vertical (V) polarizations. These spectra are used to determine instantaneous scattering parameters that are combined with a highly flexible radar system model in order to compose time-series signals in H and V. This simulation method is used to evaluate and compare the performance of several bias mitigation techniques that have been previously proposed.

Chapter 1

Introduction

Since their inception, weather radars have been constantly evolving. From frequency modulated continuous wave, to pulsed Doppler, to polarimetry, the technology of radar systems is constantly moving forward in order to better serve the intertwined goals of attaining better understanding of the atmosphere and better protection of lives and property. One of the most promising directions for the next step in this development process is the polarimetric phased array radar (PPAR). The PPAR offers all benefits of polarimetry for weather observation, as well as the agile scanning capabilities of the phased array radar. These unique capabilities of the phased array can be brought to bear on the problem of weather observation, as well as potentially allowing PPARs to perform the functions currently delegated to civil air surveillance radars. To make this vision a reality, there are technical challenges intrinsic to PPARs that must be overcome. Accurate numerical simulations offer a powerful tool for the reduction of both cost and risk in this development process. This work develops a simulation method that can be used to evaluate the performance of PPAR systems in observing fields of weather phenomena, as well as to prototype solutions to the technical challenges these systems face. These capabilities are utilized to evaluate and compare several techniques for the mitigation of antenna cross-coupling biases (i.e., biases caused by the cross-polar fields) in polarimetric measurements.

1.1 A Brief History of Weather Radar

The term radar is an acronym for **ra**dio **d**etection **a**nd **r**anging, originating as an agreed-upon term amongst the Allied powers during the second world war. Radio, in this context, refers to any electromagnetic radiation between the wavelengths of approximately 20 km and a few fractions of a millimeter (Doviak and Zrnić 2006). The first description of radar can be attributed to Nikola Tesla, who, in 1900, described the potential for a system that utilizes the reflection of electromagnetic waves off of distant objects to determine their position and speed (Tesla 1900). The first actual use of radar for the detection of objects is credited to Christian Hulsmeyer, who successfully utilized continuous waves to detect riverboats at the Hohenzollern bridge in Cologne, Germany on May 18, 1904 (Swords 1986). The first example of simultaneous detection and ranging using radio waves was actually in service of atmospheric science. It was accomplished some 20 years after Hulsmeyer's experiment by Appleton and Barnett at Cambridge University (Doviak and Zrnić 2006). They used continuous wave interferometry to determine the heights of the ionosphere. The first use of pulsed radio waves to perform detection and ranging, also in order to detect ionospheric heights, was performed by G. Breit and M.A. Tuve at the department of Terrestrial Magnetism of the Carnegie Institution (Breit and Tuve 1926).

The 1930's saw an international surge in radar development efforts for military applications (Doviak and Zrnić 2006). Particularly notable among these were the efforts of Robert A. Watson-Watt in Britain (Watson-Watt 1957). Formerly employed by the Meteorological Office to research the localization of storms through

radio emissions from lightning, Watson-Watt would develop the proposal that led to the "Chain-Home" radar network that served to provide early warning of incoming German air attacks during the Battle of Britain. The development of the multiresonant cavity magnetron in early 1940 made the use of microwaves for long range detection practical, leading to the first observations of precipitation, which likely can be attributed to J.W. Ryde in late 1940 (Doviak and Zrnić 2006). However, the earliest dedicated meteorological radars were not used for observing precipitation, but were rather profilers dedicated to studying the structure of the clear troposphere. The first use of pulsed-Doppler radar to study weather is attributable to Ian Browne and Peter Baratt of Cavendish Laboratories at Cambridge University (Barratt and Browne 1953). They used a vertically pointing radar directed into a rainshower to study the Doppler spectrum of observed precipitation.

Operational weather radar use in the United States originated from the military during World War II, during which air traffic control and defense radars were used by specially trained officers for observing and forecasting weather. These efforts led to the post-war deployment of repurposed military radars by the Weather Bureau (now the National Weather Service) as an early weather radar network, as well as the Army Signal Corps development of the AN/CPS-9 (the first purpose-built weather radar). A spate of hurricanes in the 1950's created a favorable legislative environment for the funding of the WSR-57, which would remain the NWS's flagship radar until the introduction of the WSR-88D in the 1990s (Whiton et al. 1998a). The WSR-88D is the first widely deployed pulsed-Doppler weather radar used to collect the invaluable information about wind fields (provided by the mean Doppler velocity and Doppler

spectrum width) which is widely available today. The Terminal Doppler Weather Radar (TDWR) was developed in the 1980s to improve observations of low-level wind shear near airports in order to improve safety (Whiton et al. 1998b). Together, these two systems comprise the national weather radar network in operation in the United States today.

The most recent major improvement of the network of WSR-88D radars was the addition (beggining in 2011) of dual-polarization capability. Early studies of polarization diversity in meteorological radar applications began in the first half of the twentieth century and are summarized by Newell and Geotis (1955). These early studies were focused primarily on circular and linear depolarization ratios (used to measure the depolarization of the electromagnetic waves by the scattering media). While work continued in the study of both numerical calculations of wave scattering by nonspherical raindrops and the use of polarization diversity in weather radars through the 1960's and early to mid 1970s, the concepts began to gain more momentum with papers by Seliga and Bringi (1976, 1978) on rain rate estimation through differential reflectivity (Z_{DR}) and differential propagation phase. A few years later, Sachidananda and Zrnić (1986, 1989) proposed the measurements of differential phase (ϕ_{DP}) and copolar correlation coefficient ($|\rho_{\mathrm{HV}}(0)|$). Zahrai and Zrnić (1993) obtained the first real-time full set of measurements (differential reflectivity, differential phase, and both the co-polar and cross-polar correlation coefficients). Over the next several decades, a large body of work would be produced in service of developing and

demonstrating the applications of dual-polarization measurements. These applications include quantitative precipitation estimation (QPE) (Seliga et al. 1986; Sachidananda and Zrnić 1987; Ryzhkov and Zrnić 1995; Brandes et al. 2002; Ryzhkov et al. 2005; Giangrande and Ryzhkov 2008), hydrometeor classification algorithms (HCAs) (Vivekanandan et al. 1999; Straka et al. 2000; Zrnić et al. 2001), and attenuation correction (Testud et al. 2000; Bringi et al. 2001; Snyder et al. 2010). This body of work would provide an impetus for the dual-polarization WSR-88D upgrade that brought the national weather radar network to its current state (Doviak et al. 2000).

1.2 Polarimetric Phased Array Radars

The phased array is not a recent technological development. While the major impetus for its development from World War II onward would be radar applications, it was first researched for short wave radio applications (Sarkar et al. 2006). Friis (1925) first demonstrated a non-steerable array of loop antennas. Friis and Feldman (1937) demonstrated the first scanning array. That array, like all other scanning arrays until the 1950's, relied on electromechanical methods to produce phase shifts. The 50's saw the advent of ferrite phase shifters (followed closely by diode phase shifters in the ensuing decade) that allowed for the first electronically scanning arrays (Button 1984). This development, combined with printed circuit antennas (first described by Deschamps (1953)), and solid state modules (developed through the 50's and first applied to arrays in the 60's (Sarkar et al. 2006)) gave us electronically scanning active phased arrays in the form that is recognizable today.

Until recently, the use of phased arrays in radar has primarily been confined to defense and civil air surveillance applications. The widespread study of possibilities for their use in meteorological applications is a recent development. There are numerous clear advantages to the use of phased arrays to observe weather, most of which stem in one way or another from the ability to scan electronically. Parabolic dish radars suffer from the need to scan mechanically in several ways. It constrains the speed at which scanning occurs as well as the spatial pattern of a scan. Further, the mechanical rotation of the antenna introduces beam smearing effects which increase the effective beamwidth and negatively impact the ground clutter detection and mitigation (Doviak and Zrnić 2006). Electronic scanning allows a near instantaneous change in beam position to an arbitrary angle, making possible very rapid scanning unconstrained by any particular spatial pattern, as well as a constant beam position during each dwell time.

The ability to obtain scan volumes rapidly is advantageous for several reasons. It allows for the observation of short-lived atmospheric phenomena with high temporal resolution, which is particularly important when observing severe weather. It provides better input to numerical weather prediction (NWP) models, and could potentially even allow for the use of radar to precisely map lightning channels (Zrnić et al. 2007). The ability to maintain a stationary beam during a dwell time improves data quality through the elimination of beam smearing, as well as improving measurements of rainfall and refractivity (Cheong et al. 2008a) through improved repeatability. The phased array may also offer the possibility of transverse wind retrieval through the spaced antenna method (Zrnić et al. 2007). Finally, the lack of spatial constraints on

scan patterns offers the tantalizing possibility of multifunctionality as well as adaptive weather-surveillance. This possibility of multifunctionality has become a key driver in the development of PPARs. The multimission phased array radar (MPAR) program is a multi-agency governmental effort to develop a single radar that will serve as the platform for the next generation of not only the national weather radar network, but also the national airport and air-route surveillance networks (Weber et al. 2007). In order to perform both the aviation and meteorological facets of this ambitious mission to modern standards, this radar will necessarily need to be a PPAR.

Unfortunately, the PPAR is subject to considerable technical challenges (Zrnić et al. 2012). Obtaining accurate polarimetric measurements from an operational phased array is a difficult problem for several reasons. The first is matching of the copolar H and V radiation patterns of the radar, as these patterns can differ in both the shape and amplitude. It is desirable to minimize the differences between the H and V pattern shapes through antenna design and mitigate any remaining differences in operation through adjustment of transmit and receive weightings based on characterization of the actual radiation characteristics of the array. Additionally, the H and V radiation patterns are not perfectly isolated. This is because excitation of the H port always causes some amount of radiation in the V plane (i.e., cross-polar radiation), and vice-versa. These cross-polar fields arise to some extent at every scan angle. When electronically steering the transmitted beam away from the principal planes of the array, they can reach levels capable of severe interference with meteorological measurements. These effects exist regardless of the particular antenna design (at least for the microstrip patches most often used in modern phased arrays).

There are several proposed methods for the mitigation of these effects, however, they are largely untested. Complicating efforts to resolve these issues is the challenge of maintaining the accuracy of data collected by a phased array during its operation (Fulton 2011). This is because the amplitudes and phases of the transmit and receive channels of the radar will change over time (primarily due to changes in temperature).

1.3 Motivation for Robust Numerical Simulation

Currently, few operational phased array weather radars exist. Notable non-polarimetric phased array weather radars include the National Weather Radar Testbed (Forsyth et al. 2005), a repurposed naval radar developed as a collaborative effort between several U.S. government agencies and private companies and used to study the potential of phased arrays to improve the quality of weather observations, and the MWR-05XP (Bluestein et al. 2010), an Army tactical radar modified by ProSensing, Inc., for weather observation applications. Another example is the Atmospheric Imaging Radar (Isom et al. 2013), a mobile radar operated by the University of Oklahoma's Advanced Radar Research Center (although it should be noted that, as an imaging radar, it is not a traditional phased array). Even fewer polarimetric phased arrays exist. Several examples of existing PPARS include the phase-tilt radar (Orzel 2015) developed and operated at the University of Massachusetts, Amherst, the Cylindrical Polarimetric Phased-Array Radar Demonstrator (Fulton et al. 2016) developed and operated at the University of Oklahoma, and the Ten-Panel Demonstrator (Ivić

and Byrd 2015) currently under evaluation by the National Severe Storms Laboratory. There is a scarcity of platforms available for quantifying the impact of copolar calibration issues and cross-polar biases experimentally, as well as for prototyping potential solutions to these problems. Furthermore, construction of PPARs is costly and time consuming. This makes simulation an attractive approach for expediting and guiding the development of these systems.

There are several simulator features necessary for it to be useful in quantifying the performance of PPAR systems and methods for the mitigation of the effects of cross-polar biases on weather observations. The first of these is an accurate model of the dual-polarization radiation properties of an array. The simulator must also operate on a realistic weather model, because while the actual radiated fields are determined entirely by the radar system, the effect they have on polarimetric measurements is determined in large part by the properties of the hydrometeors under observation. Finally, in order to allow for prototyping of a wide variety of solutions to the challenges faced by PPARs, the system model must be highly configurable and flexible. Taken together, these requirements form an extremely specific simulation challenge that the method presented in this paper has been designed to meet.

1.4 Outline of Thesis

Chapter 2 provides a brief overview of the technical principles fundamental to the operation of polarimetric phased arrays. This includes the set of basic principles common to the operation of all pulsed-Doppler radar systems, as well as particulars of

distributed targets, polarimetry, and phased arrays. Chapter 3 discusses the details of how cross-coupling biases arise and provides a survey of the many proposed techniques for their mitigation. In Chapter 4, the PPAR simulation method is described in detail. Chapter 5 is a quantitative comparison of the performance of two proposed cross-coupling bias mitigation techniques. Conclusions and recommendations for future work on these topics are provided in Chapter 6.

Chapter 2

Fundamentals of Polarimetric Phased Array Radars

In order to examine the simulation of PPARs it is first necesary to develop some understanding of the basic principles underlying their operation. The objective of this chapter is to provide a condensed treatment of those principles. Section 2.1 provides a simplified overview of signal transmission and reception in a pulsed-Doppler radar system, as well as a basic discussion of how the recovered signals are processed in order to retrieve information about meteorological targets. Section 2.2 covers the fundamentals of weather radar polarimetry, discussing what wave polarization is and how polarization diversity can be exploited to gain additional information about hydrometeors. Finally, Section 2.3 gives a brief overview of the fundamental operating principles of phased array antennas and how they are described mathematically.

2.1 Weather Radar Systems and Signals

This section seeks to provide a summary of the process of transmitting and receiving a signal in a pulsed-Doppler radar system. While a detailed discussion of how these systems are implemented is beyond the scope of this work, a simplified model is utilized to provide a basic understanding of the method by which pulsed-Doppler

radars are able to observe their environment. Equally important are the methods by which the recorded signals are processed in order to retrieve information about the physical characteristics of targets. This section discusses the ways in which pulsed-Doppler radar signals in general may be related to the range, radar cross-section, and velocity of point targets, as well as some of the processing concepts unique to the observation of distributed targets such as weather.

2.1.1 Fundamentals of Weather Radar Systems

Put simply, the function of a weather radar is to transmit a signal into the atmosphere as a pulse of electromagnetic energy and recover the backscattered signal from any scatterers that may be present. From that point, the received signal is compared to the transmitted signal, and the observed differences are used to recover information about the scatterers. A simplified block diagram of a typical system architecture used to carry out this process is shown in Figure 2.1.

The genesis of a weather radar signal occurs at the stabilized local oscillator (STALO). This module generates a continuous sinusoidal wave at the desired carrier frequency f_0. This signal can be expressed as

$$f(t) = \cos(2\pi f_0 t + \psi_\mathrm{t}), \tag{2.1}$$

where ψ_t is the initial phase of the signal. This signal is then modulated by a pulse which can be described by the following function:

$$U(t) = \begin{cases} 1 & 0 \leq t \leq \tau, \\ & \\ 0 & \text{otherwise.} \end{cases}, \tag{2.2}$$

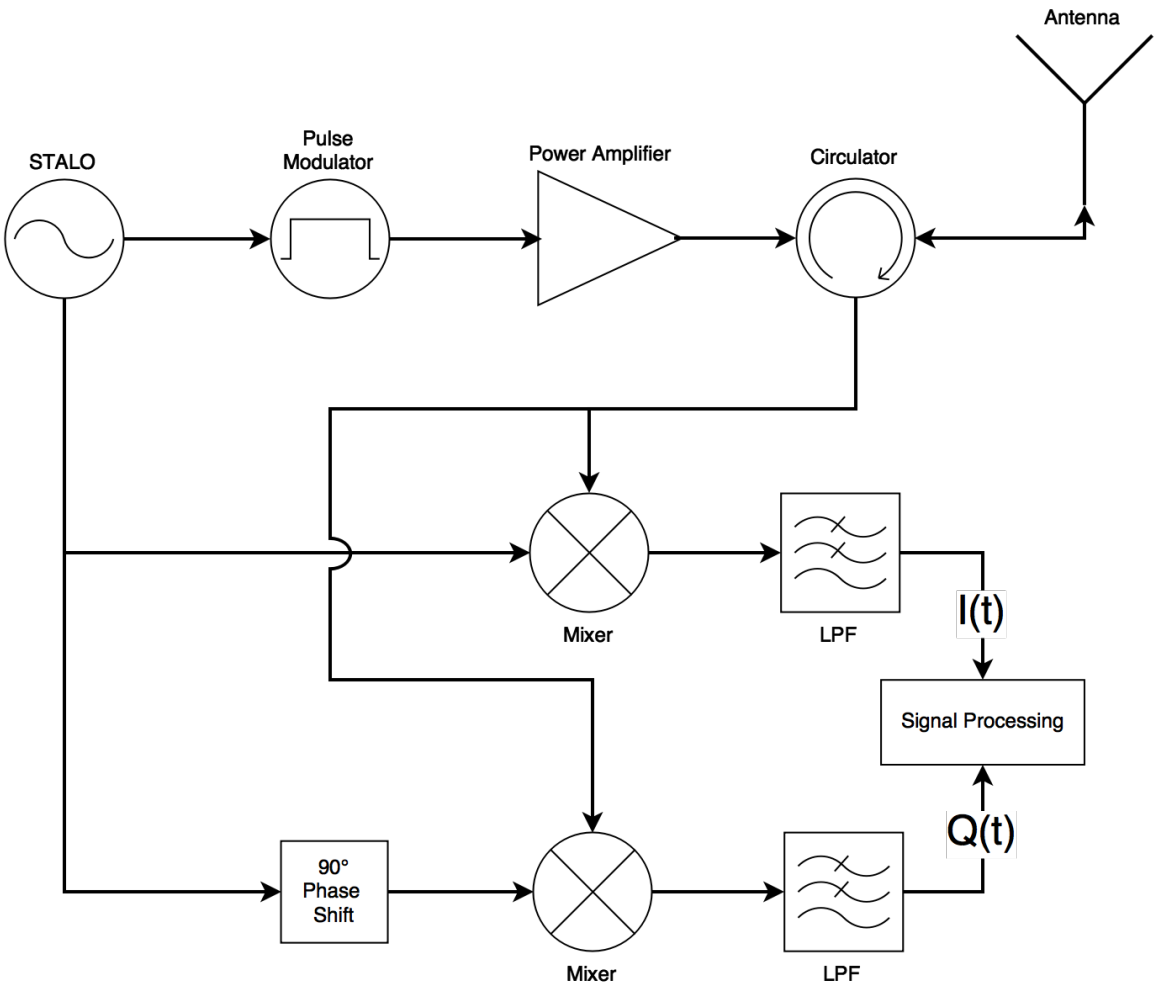

Figure 2.1: Simplified block diagram of a pulsed-Doppler radar. A continuous wave at the operating frequency is generated by the STALO. This signal is then modulated, amplified, and transmitted through the antenna. The received signal is mixed with the signal from the STALO and low-pass-filtered in order to generate an in-phase (I) baseband signal. It is also mixed with a copy of the STALO signal that has been phase-delayed by 90° to form the quadrature (Q) baseband signal. These two signals are then processed to retrieve target characteristics. This diagram is adapted from Doviak and Zrnić (2006).

where τ is the length of the pulse. The resulting pulsed signal is then passed through a high power amplifier, at which point it can be expressed as:

$$f'(t) = A_{\mathrm{t}} \cos(2\pi f_0 t + \psi_{\mathrm{t}}) U(t), \tag{2.3}$$

where A_{t} is the signal amplitude (Doviak and Zrnić 2006). The connection between the amplifier and the antenna can be made through a T/R switch, which briefly connects the antenna to the amplifier during signal transmission and switches it back to the receiver during signal reception, or a circulator, which transmits excitations on one port to the next port forward in rotation. The antenna can have any of a wide variety of possible designs. Most currently operational weather radars (such as the WSR-88D) use a parabolic dish antenna. The antenna may also consist of one or more elements of a phased array, which for radar applications are typically microstrip patches. Once transmitted from the antenna, the pulsed electromagnetic waves will travel through the atmosphere at speeds just slightly less than the speed of light. A small fraction of the transmitted energy will reflect from hydrometeors and any other targets in the environment back toward the antenna. This energy from a single target, when received by the antenna composes a signal:

$$V(t, r) = A \cos\big(2\pi f_0 (t - 2r/c) + \psi_{\mathrm{t}} + \psi_{\mathrm{s}}\big) U(t - 2r/c), \tag{2.4}$$

where r is the range from the radar to the target, c is the speed of light in a vacuum, which assumes that the small decrease in propagation speed in the atmosphere can be neglected, and ψ_{s} is the phase rotation introduced through reflection. This signal can, alternatively, be represented in phasor notation as

$$V(t, r) = A \exp\left[j 2\pi f_0 (t - 2r/c) + \psi_{\mathrm{t}} + \psi_{\mathrm{s}}\right] U(t - 2r/c). \tag{2.5}$$

For signal processing purposes, it is useful to demodulate the signal in order to remove the carrier and decompose it into two constituent components, one which is aligned in phase with the signal produced by the STALO, and another which is at a phase delay of 90° relative to the same signal. These are referred to as the in-phase (I) and quadrature (Q) signals respectively, and they correspond to the real and imaginary components of the signal as represented by a phasor:

$$V(t,r) = I(t,r) + jQ(t,r), \tag{2.6}$$

$$I(t,r) = \frac{|A|}{\sqrt{2}}\cos(\psi_{\mathrm{e}})U(t-2r/c), \tag{2.7}$$

$$Q(t,r) = -\frac{|A|}{\sqrt{2}}\sin(\psi_{\mathrm{e}})U(t-2r/c), \tag{2.8}$$

where

$$\psi_{\mathrm{e}} = \frac{-4\pi r}{\lambda} + \psi_{\mathrm{t}} + \psi_{\mathrm{s}} \tag{2.9}$$

is the total phase of the signal at baseband. This decomposition process is performed digitally in most modern radar systems.

2.1.2 Time Series Signals

The first step in analyzing the I and Q signals to recover information about targets is the process of sampling. The time interval between pulses transmitted by a radar is commonly referred to as the pulse repetition time or PRT. Over the duration of each PRT the signal received by the radar is sampled at some interval denoted by τ_{s}. The range corresponding to the nth time sample is given by

$$r_0 = n\frac{c\tau_{\mathrm{s}}}{2}. \tag{2.10}$$

This range corresponds to the center of a "range gate," a range interval in which any target illuminated by the radar will contribute to the sampled signal. The width of these range gates, equivalent to the range resolution of the radar, is given by

$$\Delta r = \frac{c\tau}{2}, \tag{2.11}$$

where τ is the pulse width (in time). It should be noted that this relationship is actually a consequence of the more fundamental relationship

$$\Delta r = \frac{c}{2\beta}, \tag{2.12}$$

where β is the bandwidth of the transmitted signal. In the case of a square pulse transmitted at constant frequency, this is equivalent to Equation 2.11. However, a long pulse that sweeps over some frequency band can be used to achieve the same range resolution as a shorter, constant frequency pulse. This is known as pulse compression, and it allows radars to achieve a higher average transmit power (and therefore a higher level of sensitivity) than possible through transmission of a constant frequency pulse at some given peak transmit power and range resolution. The three-dimensional analog to the range gate is the resolution volume, which is the three-dimensional volume in space inside which targets make significant contributions to a signal. It is defined by Equation 2.11 in the range dimension and by the two-way beamwidth (typically out to the 6dB point) of the antenna in elevation and azimuth. Using the simple relation in Equation 2.10, the range of a target to within Δr can be determined based on the time delay at which its reflected signal is received. A critical concept is that the maximum distance an electromagnetic wave can travel within a PRT (T_s) defines a maximum unambiguous range (r_a). Echoes from targets beyond this range will

be interpreted by the radar as having arisen from some pulse transmitted after the one which produced them, causing an incorrect estimate of target range. This range threshold is given by

$$r_{\mathrm{a}} = \frac{cT_{\mathrm{s}}}{2} \tag{2.13}$$

Typically, a radar will sample the received echo from each resolution volume along a given azimuth many times before transmitting at a new angle. However, it should be noted that for a constantly rotating antenna these samples are taken at angles that are only approximately the same, which results in "beam-smearing" effects. Each of these larger intervals composed of many PRTs is referred to as a dwell time or coherent processing interval (CPI). By calculating the time derivative of the phase of the received signal at a given resolution volume, information about target velocity can be retrieved. This time derivative is:

$$\frac{d\psi_{\mathrm{e}}}{dt} = -\frac{4\pi}{\lambda}\frac{dr}{dt} = -\frac{4\pi}{\lambda}v_{\mathrm{r}} = 2\pi f_{\mathrm{d}} = \omega_{\mathrm{d}} \tag{2.14}$$

where v_r is the radial velocity of the target, and f_{d} and ω_{d} are the Doppler frequency in Hertz and radians per second, respectively. Much like range measurements, estimates of Doppler frequency (and therefore of radial velocity) have a maximum unambiguous value. In this case, the value is defined by the Nyquist-Shannon sampling theorem, which states that in order for a signal to be completely determined it must be sampled at a frequency twice that of the highest frequency component of the signal. If this criterion is not met, it will result in aliasing, in which high frequency signals are erroneously measured as signals with frequencies less than half the sampling frequency. In this instance, the sampling frequency (f_{s}) is the pulse repetition frequency (PRF),

which is the reciprocal of the PRT. Applying the Nyquist-Shannon theorem yields the following expressions for the maximum unambiguous frequency (f_a) and velocity (v_a):

$$f_\mathrm{a} = \frac{f_\mathrm{s}}{2} = -\frac{2v_\mathrm{a}}{\lambda}, \tag{2.15}$$

$$v_\mathrm{a} = \pm\frac{\lambda}{4T_\mathrm{s}}. \tag{2.16}$$

It should be noted that the inverse dependencies of v_a and r_a on T_s create a tradeoff space in PRT selection between the ability to accurately detect targets at distant ranges and the ability to accurately measure high radial velocities. This is a pivotal problem of radar design commonly known as the Doppler dilemma (Doviak and Zrnić 2006).

2.1.3 Radar Range Equation

Information about the radar cross section (RCS) of a target may be retrieved from the power of the received signal. RCS is a measure of the detectability of an object via radar. It depends on the size, shape, composition, and orientation of the object relative to the incident radiation. For the purposes of this work we will assume that RCS refers to the backscatter cross-section, which corresponds to the case of a colocated transmitter and receiver. Particles also have bistatic radar cross-sections which correspond to cases win which the transmitter and receiver are at separate locations. The radar cross-section of a single target is related to the received power by the radar range equation:

$$P_\mathrm{r} = \frac{P_\mathrm{t} g^2 \lambda^2 \sigma_\mathrm{b} f^4(\theta,\phi)}{(4\pi)^3 r^4 l^2}, \tag{2.17}$$

where P_r is the received power, g is the antenna gain, σ_b is the RCS, $f^2(\theta, \phi)$ is the normalized antenna power density pattern value in the scatterer direction and l is a loss factor representing attenuation of the signal during propagation as well as any losses due to the radar system.

Weather radars, however, are not intended to observe single targets. Rather, they observe a set of distributed targets (hydrometeors) scattered throughout each resolution volume. To approximately describe this scenario, it is necessary to modify the radar range equation as follows:

$$\overline{P}_\mathrm{r}(r_0) = \frac{P_\mathrm{t} g^2 \eta c \tau \pi \theta_1^2 \lambda^2}{16(4\pi)^3 r_0^2 l^2 \ln(2)} \tag{2.18}$$

Where θ_1 is the one-way 3 dB beamwidth of an antenna with an assumed Gaussian radiation pattern, and η is reflectivity, a distributed target analog to RCS defined as:

$$\eta = \int_0^\infty \sigma_\mathrm{b}(D) N(D) dD, \tag{2.19}$$

where $N(D)$ is a drop-size distribution (DSD), a function that gives the number of drops (N) for any diameter (D) per unit volume. Assuming that reflectivity is constant throughout the resolution volume and that Rayleigh scattering is a valid approximation (the scatterer diameters are much smaller than the radar wavelength), the reflectivity can be expressed as:

$$\begin{aligned} \eta &= (\pi^5/\lambda^4)|K_w|^2 \int_0^\infty N(D) D^6 dD \\ &= (\pi^5/\lambda^4)|K_w|^2 Z, \end{aligned} \tag{2.20}$$

where $|K_w|$ is the dielectric factor for water and Z is the reflectivity factor in units of $\mathrm{mm^6 m^{-3}}$. Often, reflectivity factor is expressed is in a logarithmic scale, where $10 \log_{10} Z$ gives the reflectivity in dBZ

2.1.4 Weather Radar Equation

Doppler analysis of radar signals reflected from distributed targets has some additional complexities as compared to the analysis of signals from point targets. Rather than having a single observable Doppler frequency, the signal has Doppler frequencies distributed over some band. This is a result of the fact that the signal is composed of returns from targets with many different radial velocities. The power-weighted distribution of these radial velocities is referred to as the Doppler spectrum, and its properties can be analyzed in order to retrieve useful information about meteorological targets. The Doppler spectrum is defined mathematically as the discrete-time Fourier transform (DTFT) of the auto-correlation function (ACF) of the time-series collected from a resolution volume. Because the overall Doppler spectrum of the returns from a resolution volume is composed by the convolution of many independent spectra, it can be shown through the central limit theorem to have an expected Gaussian shape (Doviak and Zrnić 2006). Under this Gaussian assumption, the spectrum can be described completely by its first three moments.

The zeroth moment corresponds to signal power and can be defined as follows:

$$S \equiv \int_{-\infty}^{\infty} S(v)\mathrm{d}v, \tag{2.21}$$

where S is the signal power and $S(v)$ is the Doppler spectrum. Its magnitude is a function of the number, size, and composition of the hydrometeors within a resolution volume. The signal power can be converted to a reflectivity factor in dBZ through

the weather radar range equation (Equation 2.18). The first moment is the mean Doppler velocity, which can be expressed as

$$\overline{v}_{\mathrm{r}} \equiv \frac{1}{S}\int_{-\infty}^{\infty} vS(v)\mathrm{d}v. \tag{2.22}$$

This quantity reflects the power-weighted mean radial velocity of the hydrometeors within the resolution volume, which corresponds approximately to the mean wind velocity. The Doppler spectrum width is given by the square root of the second central moment of the Doppler spectrum:

$$\sigma_{\mathrm{v}}^2 \equiv \frac{1}{S}\int_{-\infty}^{\infty} [v-\overline{v}_{\mathrm{r}}]^2 S(v)\mathrm{d}v. \tag{2.23}$$

This quantity describes the diversity of radial velocities within the resolution volume and, therefore, the shear and turbulence in the volume. In practice, however, time-domain estimators of these key observable quantities are oftern preferable to the direct use of their integral definitions. Total signal power is estimated as follows:

$$\hat{P} = \frac{1}{M}\sum_{m=0}^{M-1} |V(m)|^2 + \mathcal{N}. \tag{2.24}$$

where $\mathcal{N}$ is the mean noise power. Mean radial velocity can be estimated through the phase of the lag-one autocorrelation of the time-series signal. Assuming a Gaussian Doppler spectrum, the ACF of the signal at some integer multiple of T_{s} can be expressed as

$$R(lT_{\mathrm{s}}) = S\exp[-8(\pi\sigma_{\mathrm{v}}lT_{\mathrm{s}}/\lambda)^2]\mathrm{e}^{-j4\pi\overline{v}_{\mathrm{r}}lT_{\mathrm{s}}/\lambda} + \mathcal{N}\delta_{\mathrm{l}}, \tag{2.25}$$

The ACF at any lag l can be estimated from the time series signal as

$$\hat{R}_l = \frac{1}{M}\sum_{m=0}^{M-1-|l|} V^*(m)V(m+l). \tag{2.26}$$

This allows the mean radial velocity to be estimated as

$$\hat{v}_{\mathrm{r}} = -\frac{\lambda}{4\pi T_{\mathrm{s}}} \arg \hat{R}_1 \tag{2.27}$$

and, similarly, for the spectrum width to be estimated as

$$\hat{\sigma}_{\mathrm{v}} = \frac{\lambda}{2\pi T_{\mathrm{s}}\sqrt{2}} \left| \ln\left(\frac{\hat{S}}{\hat{R}_1} \right) \right|^{1/2} \tag{2.28}$$

where $\hat{S}$ is the estimated signal power minus some estimated noise power. Or, alternatively,

$$\hat{\sigma}_{\mathrm{v}} = \frac{\lambda}{2\pi T_{\mathrm{s}}\sqrt{6}} \left| \ln\left(\frac{\hat{R}_1}{\hat{R}_2} \right) \right|^{1/2}. \tag{2.29}$$

While these products alone reveal a considerable amount of useful information about the observed regions of the atmosphere, these metrics also have limitations. Their inability to provide information about hydrometeor shape handicaps their usefulness in applications such as precipitation estimation and hydrometeor classification. The ability of radar to assist in those endeavors is significantly bolstered through the technique of polarimetry.

2.2 Weather Radar Polarimetry

Polarimetry is a powerful tool for improving the accuracy and expanding the capabilities of meteorological radar measurements. It has applications in quantitative precipitation estimation, hydrometeor classification, drop size distribution retrieval and attenuation correction. It has become a standard feature of operational weather radars. Therefore, it is critical for the proliferation of phased array weather radars

that solutions be found to the considerable challenges inherent in effective implementation of this technology in phased array systems. This section provides a brief discussion of the physical principles of electromagnetic wave polarization, the polarimetric properties of hydrometeors, and the primary polarimetric products produced by weather radars.

2.2.1 Polarized Waves

A wave is a propagating vibration. Electromagnetic waves (propagating oscillations of electric and magnetic fields) are transverse waves. This means that the oscillation of the wave is orthogonal to the direction of propagation. The polarization of an electromagnetic wave is a description of the vibration direction of the electric field, given by a trace of the motion of the tip of the electric field vector $\vec{E}$ in the plane normal to the propagation direction of the wave. This motion can be linear, elliptical,

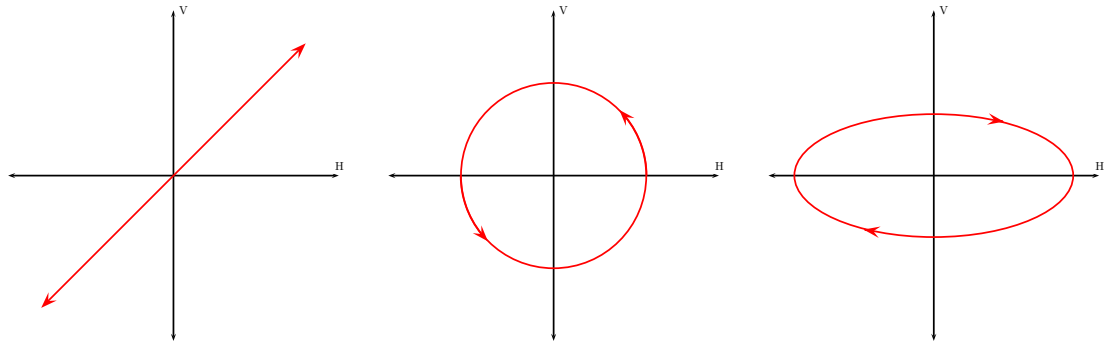

(a) (b) (c)

Figure 2.2: Traces of the electric field vector tip for (a) linear, (b) right-hand circular, and (c) left-hand elliptical polarizations. Handedness assumes wave propagation outward normal to the page.

or circular with right- or left-handed direction,(as shown in Figure 2.2) depending on the relative phases of the orthogonal components of the vector. Antennas may be designed to selectively radiate and receive some desired polarization. This allows the design of radar systems that an additional set of independent information about targets through the use of polarization diversity.

2.2.2 Polarimetric Characteristics of Precipitation

The utility of polarimetry in characterizing hydrometeors is contingent on the fact that hydrometeors have properties that cause differences in scattering behavior between polarizations. Broadly speaking, these properties are shape, orientation and composition. Before entering a short discussion of the various ways in which these properties affect polarimetric scattering behavior, it is useful to note the standard conventions for describing polarization in a weather radar context. First, while transmission and reception in a circular polarization basis has been used in weather radar polarimetry applications, the most widely used modern polarimetric products are based on a linear polarization basis. As such, all further discussion within this work will assume transmission and reception in a linear basis. The linear polarization directions used in weather radar applications are designated horizontal (H), which lies parallel to the surface of the earth and orthogonal to the direction of signal propagation, and vertical (V) which is orthogonal to the earth's surface and to the direction

of signal propagation. A simplified model of backscatter by a single particle can be expressed as follows:

$$\begin{bmatrix} E_{\mathrm{rh}} \\ E_{\mathrm{rv}} \end{bmatrix} = \begin{bmatrix} s_{\mathrm{hh}} & s_{\mathrm{hv}} \\ s_{\mathrm{vh}} & s_{\mathrm{vv}} \end{bmatrix} \begin{bmatrix} E_{\mathrm{ih}} \\ E_{\mathrm{iv}} \end{bmatrix}, \tag{2.30}$$

where E_{rh} and E_{rv} are the reflected electric fields in the H and V polariztions back toward the direction of arrival of the incident radiation, s_{hh}, s_{hv}, s_{vh}, and s_{vv} are the scattering parameters of the particle. The first letter of the subscript represents the polarization of the incident radiation and the second letter is the polarization to which it is scattered. E_{ih} and E_{iv} are the incident electric fields in the H and V polarizations. Each of these quantities can be expressed as a phasor with some amplitude and phase.

In order to understand how the shape, size, orientation and composition of a particle affects these scattering parameters, we will first make several simplifying assumptions. The first is that particle shapes can be reasonably approximated by

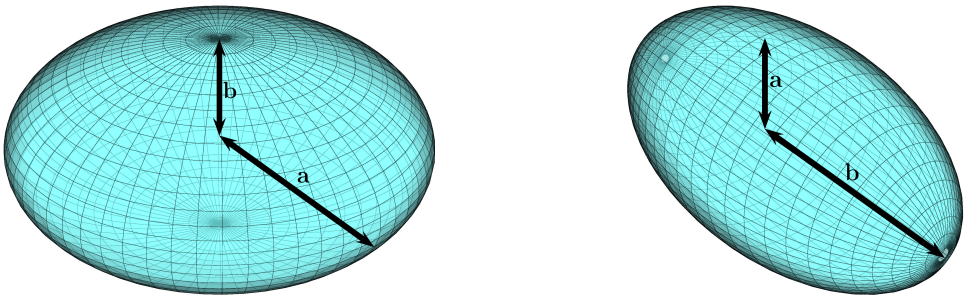

(a) (b)

Figure 2.3: Examples of the two possible spheroid configurations. An (a) oblate spheroid is formed by revolution of an ellipse about its minor axis, while a (b) prolate spheroid is formed by revolution about the major axis.

spheroids. While actual hydrometeors can have widely varying shapes, particularly when considering those composed of ice, this approximation works well for explaining much of the polarimetric behavior of precipitation. The second assumption we will make is that the hydrometors are sufficiently electrically small (typically, $D < \lambda/50$) that the electric fields induced within the hydrometeor by incident radiation are appoximately uniform. This is known as the Rayleigh assumption, and it allows us to treat the the reflection of an incident wave as re-radiation by a dipole. This leads to the Rayleigh-Gans scattering model for spheroids (Bringi and Chandrasekar 2001). Let the spheroid be formed by the revolution of an ellipse about one of its axes. The axis about which the ellipse is rotated is designated b, and the orthogonal axis is a. Figure 2.3 shows diagrams of both prolate (most often used to model some types of ice crystal) and oblate spheroids (used to model raindrops and most other forms of precipitation). As shown in Section 6.32 of Van de Hulst (2012), we can define a set of shape parameters L_x, L_y and L_z for each of these cases:

$$L_x = L_y = \frac{1}{2}(1 - L_z) \tag{2.31}$$

With L_z for an oblate spheroid ($a > b$) being equal to

$$L_z = \frac{1+g^2}{g^2}\left(1 - \frac{1}{g}\arctan(g)\right), \tag{2.32}$$

$$g^2 = \left(\frac{a}{b}\right) - 1, \tag{2.33}$$

and for a prolate spheroid ($a < b$) being equal to:

$$L_z = \frac{1-e^2}{e^2}\left(-1 + \frac{1}{2e}\ln\frac{1+e}{1-e}\right), \tag{2.34}$$

$$e^2 = 1 - \left(\frac{b}{a}\right)^2. \tag{2.35}$$

Using these definititions the scattering parameter s for the polarization aligned with the a or b axis of the spheroid can be expressed as

$$s_{\mathrm{a,b}} = k^2 a^2 b \frac{\epsilon_{\mathrm{r}} - 1}{3[1 + L_{\mathrm{a,b}}(\epsilon_{\mathrm{r}} - 1)]}, \tag{2.36}$$

where ϵ_{r} is the complex relative dielectric constant of the particle and k is the wavenumber. From this expression it can be shown that the greater the value of a, the greater the amplitude and phase of the associated scattering parameter, and likewise for the b axis. This allows information about the dimensions of the spheroid to be inferred from its scattering behavior. However, there is a caveat:

$$\frac{s_{\mathrm{a}}}{s_{\mathrm{b}}} = \frac{[1 + L_{\mathrm{b}}(\epsilon_{\mathrm{r}} - 1)]}{[1 + L_{\mathrm{a}}(\epsilon_{\mathrm{r}} - 1)]}, \tag{2.37}$$

$$\lim_{\epsilon_r \to 1} \frac{s_{\mathrm{a}}}{s_{\mathrm{b}}} = 1. \tag{2.38}$$

In other words, the closer the complex relative dielectric constant of the particle to 1 (corresponding to free space) the less pronounced the differences in scattering behavior between the two spheroid axes become. Therefore, the composition of a particle, as well as its shape, plays a role in determining its polarimetric characteristics. If we consider a scenario in which a aligns with the conventional H polarization direction and b aligns with V, we will obtain the expression:

$$\begin{bmatrix} E_{\mathrm{rh}} \\ E_{\mathrm{rv}} \end{bmatrix} = \begin{bmatrix} s_{\mathrm{a}} & 0 \\ 0 & s_{\mathrm{b}} \end{bmatrix} \begin{bmatrix} E_{\mathrm{ih}} \\ E_{\mathrm{iv}} \end{bmatrix} = \mathbf{SE_i} \tag{2.39}$$

with the zeros along the off-diagonal of the scattering matrix indicating that no mixing between the incident fields is induced during the scattering process. However, things are not always this simple. If the a and b axes of the spheroid are rotated by some

angle (θ,ϕ) as represented in Figure 2.4, projection of the H/V coordinate basis onto the axes of the spheroid giving us an effective scattering matrix (Zhang 2016) $\mathbf{S}'$ as:

$$\mathbf{S}' = \begin{bmatrix} -\big(s_{\mathrm{a}}(\cos^2\theta\sin^2\phi + \cos^2\phi) + s_{\mathrm{b}}\sin^2\theta\sin^2\phi\big) & (s_{\mathrm{a}} - s_{\mathrm{b}})\sin\theta\cos\theta\sin\phi \\ (s_{\mathrm{a}} - s_{\mathrm{b}})\sin\theta\cos\theta\sin\phi & s_{\mathrm{a}}(\sin^2\theta + \cos^2\phi) + s_{\mathrm{b}}\cos^2(\theta) \end{bmatrix}. \tag{2.40}$$

Accordingly, scattering from a spheroid whose axes of symmetry are tilted off of the H/V polarization basis will result in depolarization due to the non-zero off-diagonal terms of the scattering matrix. Thus, a particle's orientation also plays a role in determining its polarimetric properties. An important concept is that scattering does not occur only in the backward direction. A scattering matrix exists for every possible direction relative to the direction of arrival of the incident radiation, including forward along the path of the wave's propagation. Under the Rayleigh assumption, this forward scattering matrix is equal to the backscattering matrix. This results in an increasing differential phase delay and attenuation between the H and V polarized waves as they move along the propagation path. This is less pronounced for smaller, more sphericle particles.

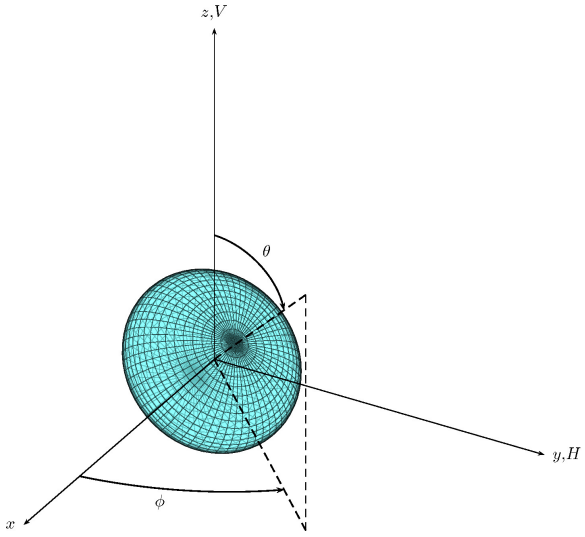

Figure 2.4: Illustration of an oblate spheroid scatterer oriented at some arbitrary angle (θ, ϕ) relative to the H/V polarization basis.

2.2.3 Polarimetric Variables

Polarimetric radars are able to transmit and receive signals in the H and V polarizations. The corresponding time-series for each polarization can be used to derive products that reflect the aggregate polarimetric properties of the scatterers within a resolution volume. The most widely used of these products are H reflectivity (Z_{H}), V reflectivity (Z_{V}), differential reflectivity (Z_{DR}), differential phase (ϕ_{DP}), specific differential phase (K_{DP}) and copolar correlation coefficient ($|\rho_{\mathrm{HV}}(0)|$). The remainder of this section will be devoted to an explanation of how these parameters relate to the shape and orientation of spheroidal hydrometeors (Zhang 2016) as well as how they are estimated from time-series signals (Bringi and Chandrasekar 2001). Z_{H} and Z_{V} can be expressed in terms of the scattering parameters within a volume as follows:

$$Z_{\mathrm{hh,vv}} = \frac{4\lambda^4}{\pi^4 |K_{\mathrm{w}}|^2} \langle n | s_{\mathrm{hh,vv}} |^2 \rangle, \tag{2.41}$$

where n is the number of scatterers in the volume and the dielectric factor for water is:

$$K_{\mathrm{w}} = \frac{\epsilon - 1}{\epsilon + 2}, \tag{2.42}$$

where ϵ is the dielectric constant of water. The polarimetric reflectivity values are calculated from the H and V time-series data $V_{\mathrm{h}}(m)$ and $V_{\mathrm{v}}(m)$ by using Equation 2.24 to estimate the average power of each signal and then using the radar range equation to convert each power to a reflectivity. The Z_{DR} is simply the ratio of the H and V reflectivities expressed in decibels:

$$Z_{\mathrm{DR}} = 10 \log \left(\frac{Z_{\mathrm{hh}}}{Z_{\mathrm{vv}}} \right). \tag{2.43}$$

This quantity is estimated by computing the ratio of power estimates in H and V. Z_{DR} is closely related to the average H/V aspect ratio of the hydrometeors within a volume. One key application for Z_{DR} is rain rate estimation. Using reflectivity alone, it is difficult to distinguish between rainfall scenarios with many small drops and those with a few large drops. These two scenarios may produce identical reflectivities, but drastically different rainfall rates. Z_{DR} is useful for distinguishing the scenarios because large drops tend to become more "flattened" by the effects of drag, and therefore have greater dimensions in H, resulting in higher Z_{DR}.

Another quantity closely related to the aspect ratio of precipitation is K_{DP}, which can be calculated from scattering parameters (Zhang 2016) as:

$$K_{\mathrm{DP}} = \frac{180}{\pi}\mathrm{Re}\left[\frac{2\pi}{k}\langle n(s_{\mathrm{a}} - s_{\mathrm{b}})\rangle\frac{1}{2}\left(1 + e^{-2\sigma_\theta^2}\right)e^{-2\sigma_\phi^2}\right]. \tag{2.44}$$

where σ_θ^2 and σ_ϕ^2 are the variances of the two canting angles among the hydrometeors in the volume. K_{DP} is a measure of the differential phase shift between H and V accumulated per unit length along the propagation path. However, it is not measured directly. It is estimated from ϕ_{DP} which is related by the expression:

$$\phi_{\mathrm{DP}} = 2\int_0^{r_0} K_{DP}\ \mathrm{d}r. \tag{2.45}$$

In order to discuss how ϕ_{DP} is calculated from time-series data, it is necessary to briefly describe the two different modes of radar operation most commonly used to collect polarimetric data, as the procedure is slightly different for each. The first mode is simultaneous horizontal and vertical (SHV). In this mode a signal is transmitted on both H and V simultaneously on each PRT. By contrast, in alternating horizontal and vertical (AHV) mode, the polarization of the transmitted signal alternates between

H and V on each PRT. In simultaneous mode, the $\phi_{\rm DP}$ may be estimated from the zero-lag covariance $\hat{R}_{vh}[0]$:

$$\hat{\phi}_{\rm DP} = \angle \hat{R}_{\rm vh}[0] \tag{2.46}$$

$$\hat{R}_{\rm vh}[0] = \frac{1}{M}\sum_{m=0}^{M-1} V_{\rm v}[m]V_{\rm h}^{*}[m]. \tag{2.47}$$

Whereas in AHV mode we do not have the zero-lag covariance available. Therefore, we calculate $\phi_{\rm DP}$ from two single-lag covariances:

$$\hat{\phi}_{\rm DP} = \frac{1}{2}\Big[\arg\big(\hat{R}_{\rm vh}[1]\big) - \arg\big(\hat{R}_{\rm hv}[1]\big)\Big], \tag{2.48}$$

$$\hat{R}_{\rm vh}[1] = \frac{1}{N}\sum_{n=1}^{N} V_{\rm v}[2n]V_{\rm h}^{*}[2n-1], \tag{2.49}$$

$$\hat{R}_{\rm hv}[1] = \frac{1}{N}\sum_{n=1}^{N-1} V_{\rm h}[2n+1]V_{\rm v}^{*}[2n]. \tag{2.50}$$

As $\phi_{\rm DP}$, much like attenuation, is a path-integrated quantity, it is particularly useful for attenuation correction applications.

The final major parameter is $|\rho_{\rm HV}(0)|$. It is related to the scattering parameters of the particles within the resolution volume by

$$|\rho_{\rm hv}(0)| = \frac{|\langle n s_{\rm hh} s_{\rm vv}\rangle|}{\big(\langle n|s_{\rm hh}|^2\rangle\langle n|s_{\rm vv}|^2\rangle\big)^{1/2}}. \tag{2.51}$$

Like $\phi_{\rm DP}$ it must be calculated differently for SHV and AHV operation modes. In SHV, $|\rho_{\rm HV}(0)|$ is estimated as

$$|\hat{\rho}_{\rm hv}(0)| = \frac{\hat{R}_{\rm vh}[0]}{(\hat{S}_{\rm h}\hat{S}_{\rm v})^{1/2}}, \tag{2.52}$$

$$\hat{R}_{\rm vh}[0] = \frac{1}{N}\sum_{n=1}^{N} V_{\rm v}[n]V_{\rm h}^{*}[n]. \tag{2.53}$$

and in AHV mode the estimator is

$$\hat{\rho}_{\mathrm{hv}} = \frac{|\hat{\rho}_{\mathrm{hv}}[1]|}{|\hat{\rho}[2]|^{0.25}}, \tag{2.54}$$

$$\hat{\rho}_{\mathrm{hv}}[1] = \frac{\hat{R}_{\mathrm{hv}}[1]}{\sqrt{\hat{S}_{\mathrm{h}}\hat{S}_{\mathrm{v}}}}, \tag{2.55}$$

$$\hat{\rho}[2] = \frac{1}{N}\sum_{n=1}^{N-1} V_{\mathrm{h}}[2n+1]V_{\mathrm{h}}^{*}[2n-1]. \tag{2.56}$$

$|\rho_{\mathrm{HV}}(0)|$ is fundamentally an estimator of the diversity of the polarimetric characteristics of the scatterers within a resolution volume. It plays a particularly important role in hydrometeor classification, as well as in more specialized applications such as identifying tornado debris.

Now that the basic foundations for pulsed-Doppler radar and polarimetry have been established, the fundamental principles of the phased array antenna are the major remaining component in our summary of the basic underpinnings of PPAR operation.

2.3 Phased Arrays

The use of phased array antennas in radar applications offers a number of advantages in exchange for an increase in cost and complexity. Among the most important are agile beamsteering, multifunctionality, and the potential for adaptive array processing. This section will provide an overview of the basic operating principles and mathematical description of phased arrays, initially for a simple linear array and eventually for an arbitrary array configuration.

2.3.1 Linear Phased Arrays

In order to demonstrate the basic operating principle of a phased array, it is instructive to first consider a uniform linear array (ULA). A ULA is defined as consisting of a set of sensors arranged in a straight line with some uniform spacing. We will consider a ULA consisting of M antennas with a uniform spacing d as illustrated in Figure 2.5. Next, consider a monochromatic plane wave with temporal variation Ae^{jkt} impingent on the array from some angle θ with respect to the y-axis. In this scenario, the received signal at the mth element can be expressed as:

$$y_m(t) = Ae^{j[k(t-md\sin(\theta)/c)+\phi_0]} \tag{2.57}$$

Where ϕ_0 is the measured phase of the received signal at the element corresponding to $m = 0$ (hereafter refered to as the reference element). Let $y_m[t_0]$ be a single time sample taken at the mth element at time t_0. Arranging the samples from each element at time t_0 into a vector $\mathbf{y}$, we can write (Richards 2005):

$$\mathbf{y} = \begin{bmatrix} y_0[t_0] & y_1[t_0] & ... & y_{M-1}[t_0] \end{bmatrix} \tag{2.58}$$

$$= Ae^{jkt_0+\phi_0} \begin{bmatrix} 1 & e^{-jkd\sin(\theta)} & ... & e^{-(M-1)jkd\sin(\theta)} \end{bmatrix} \tag{2.59}$$

$$= \hat{A} \begin{bmatrix} 1 & e^{-jK_\theta} & ... & e^{-j(M-1)K_\theta} \end{bmatrix} \tag{2.60}$$

$$\equiv \hat{A}\mathbf{a}_s(\theta) \tag{2.61}$$

We now have K_θ, a spatial frequency which represents the differential phase in the received signal between adjacent elements, $\hat{A}$, a complex amplitude representing the amplitude of the impingent plane wave and its phase at element $m = 0$ and $\mathbf{a}_s(\theta)$ a vector containing the phase delay (in phasor form) between each element and the

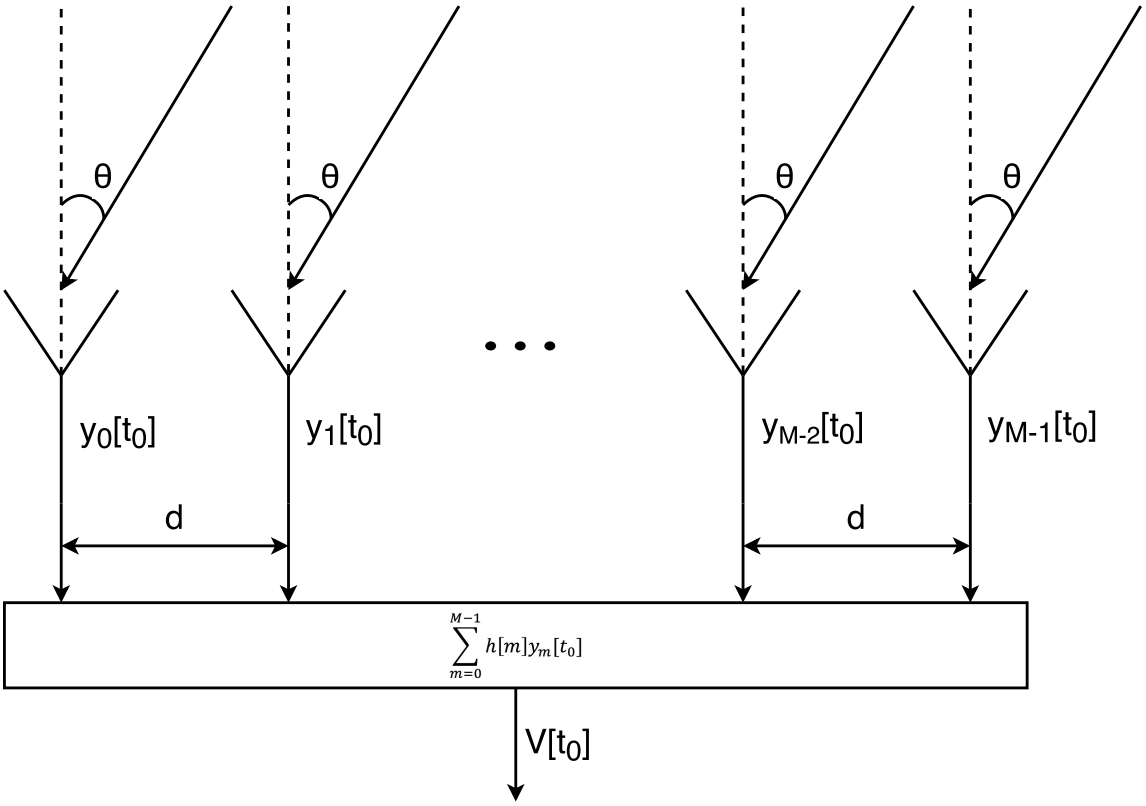

Figure 2.5: A diagram of the beamforming process for a uniform linear array. The signal of interest arrives at angle θ from the direction normal to the array. The signal received by each element is designated y_m, where m is the element index. The signal is sampled at time t_0 and summed over all elements after application of the beamforming weights in vector $\mathbf{h}$. This yields the time series sample at time t_0. This diagram is adapted from Richards (2005)

reference element. This vector is referred to as the spatial steering vector. Next consider the weighted summation of the samples at each element using weights chosen such that the samples are aligned in phase. This operation can be expressed as:

$$z = \mathbf{h^T y}, \tag{2.62}$$

$$\mathbf{h} = \begin{bmatrix} w_0 & w_1 e^{jK_\theta} & ... & w_{M-1} e^{j(M-1)K_\theta} \end{bmatrix} \tag{2.63}$$

where w_m is an amplitude weight for the mth element. This weighting results in a situation where a signal with wavenumber $k = 2\pi/\lambda$ impingent upon the array from θ will be summed constructively. This effectively "steers" the receive beam of the array to that angle. The amplitude weights can be used to apply a taper for the purpose of suppressing the sidelobes of the radiation pattern of the antenna. From the principle of reciprocity, we can state that that applications of these same weights to the element excitations on transmit will steer the transmitted radiation in the same direction. For a beamformer steered to some angle θ_0, the response of that beamformer to an impingent wavefront from some angle θ can be obtained as follows:

$$z(\theta) = \mathbf{h'y} = \hat{A} \sum_{m=0}^{M-1} w_m e^{-j(K_\theta - K_{\theta_0})m} \tag{2.64}$$

This response, which is simply the DTFT of the sequence of complex weights, is the array factor.

2.3.2 Arbitrary Array Geometry

We can generalize this simple superposition-based beamforming process to multiple dimensions and arbitrary array geometries by calculating the spatial phase for each element separately (Wang and He 2010):

$$\Phi_m(\theta, \phi) = k(\hat{\mathbf{r}}_{\theta,\phi} \cdot \mathbf{R_m}) \tag{2.65}$$

Where $\hat{\mathbf{r}}_{\theta,\phi}$ is the unit vector from the coordinate system origin to the observation direction (θ,ϕ), θ and ϕ are defined as angles from each of the array's principle planes, and $\mathbf{R_m}$ is a position vector from the origin to the mth element. From this generalized spatial phase expression we can arrive at a generalized form of $\mathbf{y}$, the value of $\mathbf{h}$ necessary to steer the beam to some angle (θ_0,ϕ_0), as well as an array factor $z(\theta, \phi)$:

$$\mathbf{y} = \hat{A} \begin{bmatrix} 1 & e^{-j\Phi_1(\theta,\phi)} & ... & e^{-j\Phi_{M-1}(\theta,\phi)} \end{bmatrix}, \tag{2.66}$$

$$\mathbf{h} = \begin{bmatrix} w_0 & w_1 e^{-j\Phi_1(\theta_0,\phi_0)} & ... & w_{M-1} e^{-j\Phi_{M-1}(\theta_0,\phi_0)} \end{bmatrix}, \tag{2.67}$$

$$z(\theta, \phi) = \mathbf{h}'\mathbf{y} = \hat{A} \sum_{m=0}^{M-1} w_m e^{j[\Phi_m(\theta_0,\phi_0) - \Phi_m(\theta,\phi)]}. \tag{2.68}$$

This array factor is not a complete description of the radiation characteristics of an array. The radiation characteristics of the individual elements must be accounted for. For arbitrary patterns at each element and arbitrary array geometry, the radiated field in any direction $F(\theta, \phi)$ can be calculated as

$$F(\theta, \phi) = \sum_{m=0}^{M-1} z(\theta, \phi) f_m(\theta, \phi), \tag{2.69}$$

where $f_m(\theta, \phi)$ is the complex-valued radiated field pattern of the mth element in the direction (θ, ϕ). For the special case of a planar array with identical radiation

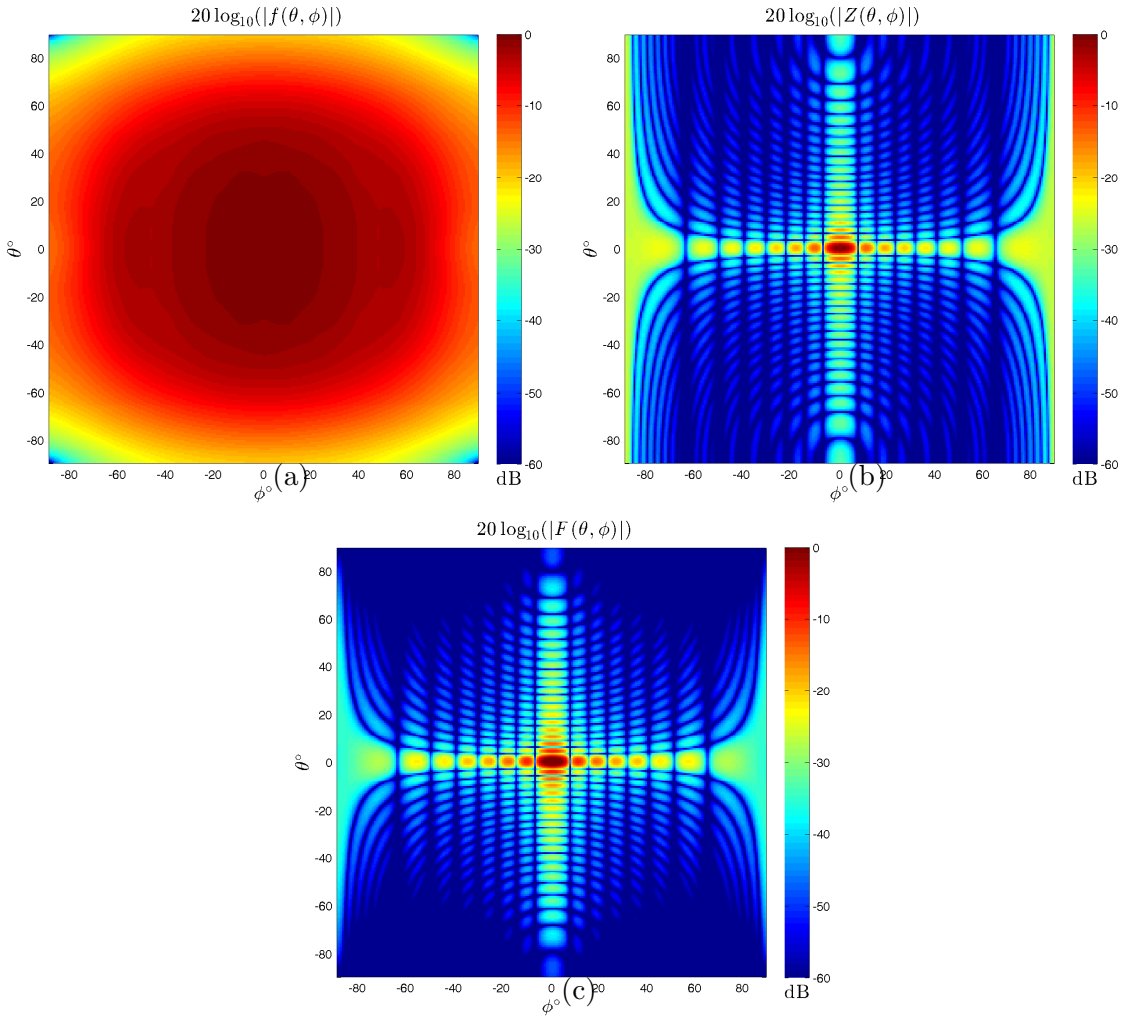

Figure 2.6: Example of the calculation of an array radiation pattern through multiplication of an element pattern and array factor. The element pattern (a) is for a simulated H-polarized microstrip patch, and the array factor (b) is for a 16 × 40 element planar array. Multiplication of the two at each angle yields the array radiation pattern (c).

patterns at each element, which can be a reasonably valid assumption for large arrays, the expression can be simplified (Bhattacharyya 2006):

$$F(\theta,\phi) = z(\theta,\phi)f(\theta,\phi). \tag{2.70}$$

An example of the results of this calculation is shown in Figure 2.6.

Before concluding the discussion of phased arrays, it should be noted that there are a number of possible architectures for phased array implementation (Skolnik 2001). The oldest architecture is the passive array, in which the entire beamforming process is carried out by analog electronics and the radar system has only a single transmitter and receiver (T/R module). Other possible implementations are the subarray architecture, in which the radar has several sets of T/R modules, each paired with some subsection of the array through an analog beamformer. This allows for more flexible and more adaptive scan strategies than the passive array, but it is not so flexible as the fully active array, in which each individual element has its own T/R module. In the most recent arrays, these T/R modules may even entirely eschew phase shifters and attenuators, performing those functions instead in the digital-to-analog conversion process. With that, our discussion of the theoretical components underlying PPAR operation is complete, and we can turn our attention to the unique problems encountered when polarimetry and electronic beam steering are combined in a single system.

Chapter 3

Cross Coupling Biases and Techniques for Mitigation

3.1 Mechanisms of Cross Coupling Bias

Now that the basic principles of both phased array radars and of polarimetry have been discussed, it is possible to examine the problems that arise when attempts are made to combine these technologies. First, it is necessary to establish a model for dual-polarization antennas generally and for dual-polarization arrays in particular. Then, the issue of precisely defining a polarization basis will be discussed. This will include an overview of the different bases commonly used when characterizing the polarization properties of antennas as well as the H/V polarization basis as typically defined in the context of weather radar polarimetry. Next, the chapter will discuss the physical origins of cross-polar fields due to electronic beam steering, using several common types of radiating elements as example cases. An explanation of the effects of mechanical elevation on cross-polar fields will also be provided. Finally, the chapter will conclude with a review of the methods that have been proposed in the literature for the mitigation of the effects of cross-polar fields on estimates of polarimetric weather radar products.

3.1.1 A Model for Dual-Polarization Arrays

The first step toward a model for dual-polarization arrays is a model for an individual dual-polarization radiating element. Chapter 2 introduced the concept of a radiation pattern, which defines the amplitude and phase of the electric field radiated from an antenna at any angle (θ, ϕ). The radiative behavior of a dual-polarization antenna is not described by a single radiation pattern. The antenna has two ports, one corresponding to each polarization. Let the two polarizations be designated H and V for ease of discussion. An excitation on the H port produces radiation primarily in the H polarization, but it also produces some (generally undesirable) radiation in the V polarization as well. The inverse is true for the V port. Therefore, it requires a set of four patterns to completely describe the antennas behavior, representing the radiation produced in each polarization by an excitation on each port. These patterns will be designated $f_{\mathrm{hh}}(\theta, \phi)$, $f_{\mathrm{hv}}(\theta, \phi)$, $f_{\mathrm{vh}}(\theta, \phi)$, and $f_{\mathrm{vv}}(\theta, \phi)$, where the first letter of the subscript indicates the polarization of the radiation described by the pattern and the second letter of the subscript indicates the port excited in order to produce that radiation. Additionally, as a consequence of reciprocity, this same phenomenon occurs as the antenna receives incident radiation. Incident H polarized radiation produces some signal on the V port as well as the H port, and incident V polarized radiation behaves likewise. The process for calculating polarimetric array radiation patterns is identical to that used in the calculation of single-polarization array radiation, except that it must be performed separately for each of the four patterns. A desired electronic steering angle (θ_0, ϕ_0) is chosen and for each element

pattern, a corresponding array radiation pattern is calculated through either the general weight-and-sum process (Equation 2.69) or through array factor multiplication in the simplified case of a planar array with identical elements (Equation 2.70). In the case of an array with identical element weighting on transmit and receive, this yields a set of dual polarization array radiation patterns designated $F_{\mathrm{hh}}(\theta_0, \phi_0, \theta, \phi)$, $F_{\mathrm{hv}}(\theta, \phi, \theta_0, \phi_0)$, $F_{\mathrm{vh}}(\theta, \phi, \theta_0, \phi_0)$, and $F_{\mathrm{vv}}(\theta, \phi, \theta_0, \phi_0)$. Combining this model of radiation and reception with the general model for dual-polarization scattering (Equation 2.30) and the radar range equation (Equation 2.17), we can write a matrix-based model for the relationship between the excitation on each antenna port of a radar and the signal received due to scattering from a point target:

$$\begin{bmatrix} V_{\mathrm{h}}^{Rx} \\ V_{\mathrm{v}}^{Rx} \end{bmatrix} = \frac{e^{-2jkr}}{r^2} \begin{bmatrix} F_{\mathrm{hh}}(\theta, \phi, \theta_0, \phi_0) & F_{\mathrm{vh}}(\theta, \phi, \theta_0, \phi_0) \\ F_{\mathrm{hv}}(\theta, \phi, \theta_0, \phi_0) & F_{\mathrm{vv}}(\theta, \phi, \theta_0, \phi_0) \end{bmatrix} \begin{bmatrix} s_{\mathrm{hh}} & s_{\mathrm{hv}} \\ s_{\mathrm{vh}} & s_{\mathrm{vv}} \end{bmatrix} \begin{bmatrix} F_{\mathrm{hh}}(\theta, \phi, \theta_0, \phi_0) & F_{\mathrm{hv}}(\theta, \phi, \theta_0, \phi_0) \\ F_{\mathrm{vh}}(\theta, \phi, \theta_0, \phi_0) & F_{\mathrm{vv}}(\theta, \phi, \theta_0, \phi_0) \end{bmatrix} \begin{bmatrix} V_{\mathrm{h}}^{\mathrm{Tx}} \\ V_{\mathrm{v}}^{\mathrm{Tx}} \end{bmatrix}. \quad (3.1)$$

Normalizing for the phase and amplitude effects of target range and condensing the notation, we obtain a simplified expression for the effects of dual-polarization patterns on the measured fields scattered from a target:

$$\mathbf{V'_{Rx}} = \mathbf{F^T S F V_{Tx}}, \quad (3.2)$$

where the $'$ denotes the normalization for target range. As shown in Figure 3.1, the magnitude of the cross-polar fields radiated from an array is largely controlled by the magnitude of cross-polar fields of the array elements in the electronic steering direction (θ_0, ϕ_0). This however, does not explain the physical reasons why these

cross-polar fields radiate from the elements in the first place. In order to explain the physical origins of this phenomenon, however, it is necessary to first rigorously define cross-polarization.

3.1.2 Defining Cross-Polarization for Weather PPARs

In modeling weather radar polarimetry, it is necessary to take great care in ensuring that the polarization basis used to describe antenna characteristics matches that used to describe radiation incident on a hydrometeor, and if it does not, to transform the measurement basis appropriately in any attempt to calculate the effects of antenna patterns on polarimetric measurements. Ludwig (1973) describes three distinct definitions (illustrated in Figure 3.2) of co- and cross-polarization that have historically been used in the literature on antennas. The first definition, commonly referred to as Ludwig I, defines one unit vector in a rectangular coordinate system to represent the reference polarization, and another to represent the cross-polarization. The second, Ludwig II, defines the co- and cross-polarization directions using the tangential unit vectors of a spherical coordinate system with the antenna under test (AUT) located at the origin. The third definition, Ludwig III, is defined as "what one measures when antenna patterns are taken in the usual manner" (Ludwig 1973). More precisely, a reference polarization cut is obtained when one aligns a single-polarization probe in azimuth and polarization with the AUT, which may be tilted at some elevation angle, and then rotates the AUT in azimuth in order to obtain a cut. The procedure is identical to obtain a cross-polarization cut, except for the single difference that when

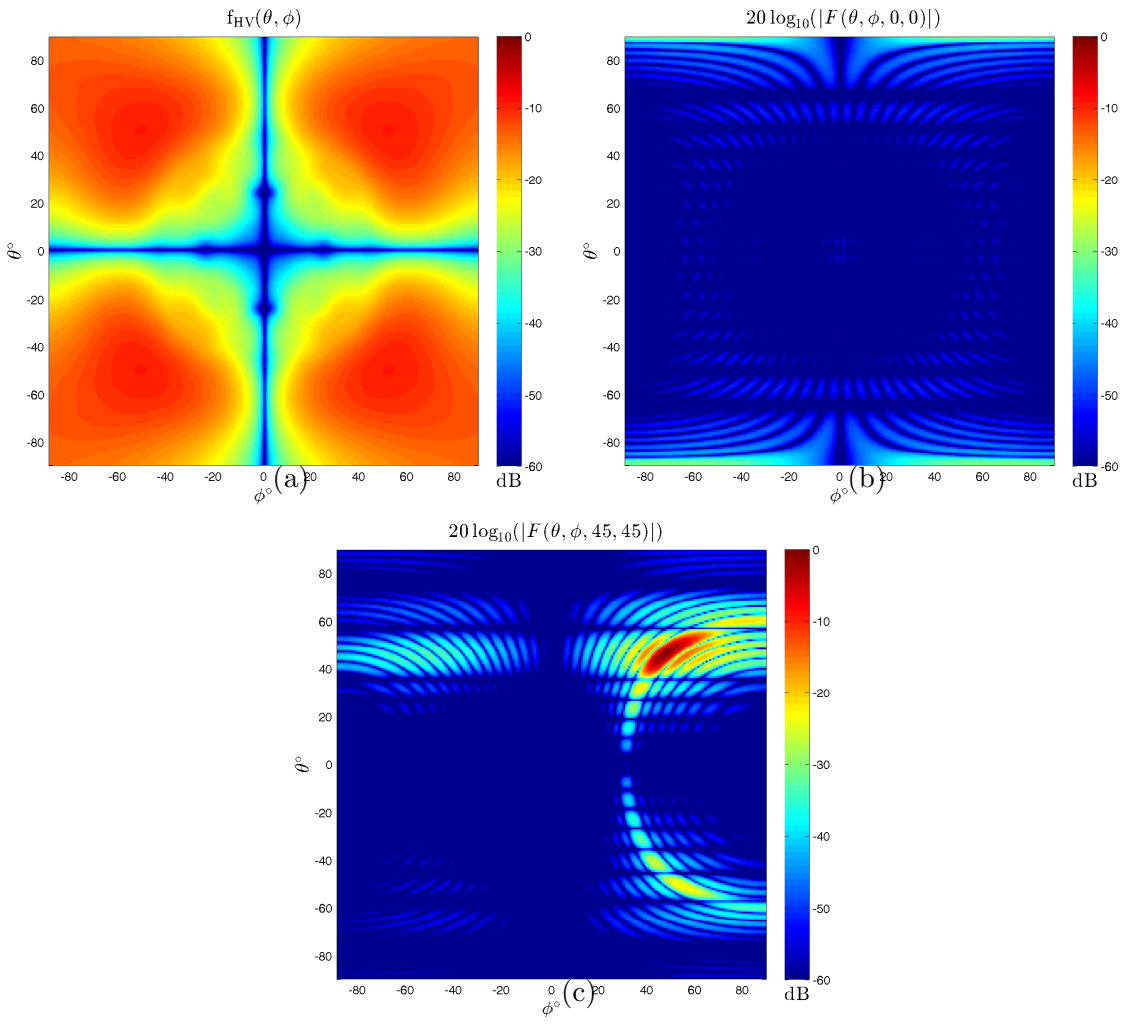

Figure 3.1: a) Cross-polar element pattern. b) Corresponding cross-polar radiation pattern for an array composed of those elements steered to broadside. c) Cross-polar radiation pattern for the same array steered to $(45°, 45°)$. The array patterns correspond to a 16×40 element S-band array with $\lambda/2$ inter-element spacing. The patterns shown here are untapered, leading to a 3dB beamwidth of approximately $2.5° \times 6.4°$.

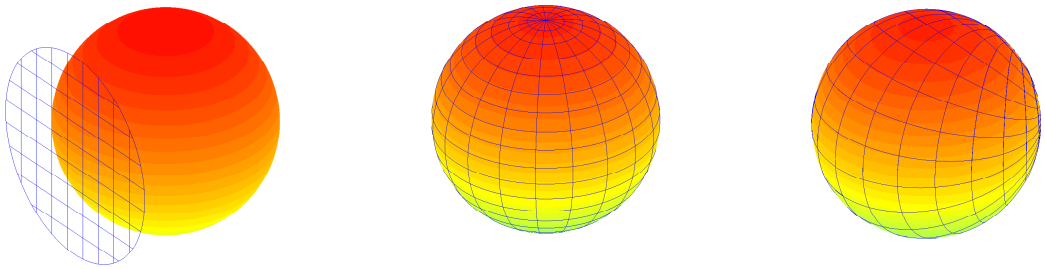

(a) (b) (c)

Figure 3.2: The Ludwig I (a), II (b), and III (c) definitions of co- and cross-polarization. The blue grid in each figure illustrates the polarization basis for each definition relative to a spherical surface centered on the antenna under test. This diagram is adapted from Ludwig (1973).

the two antennas are initally aligned in azimuth, the probe is rotated such that its polarization is orthogonal to that of the AUT.

Let us define a spherical coordinate system such that:

$$\hat{\mathbf{r}} = \sin\theta\cos\phi\hat{\mathbf{i}} + \sin\theta\sin\phi\hat{\mathbf{j}} + \cos\theta\hat{\mathbf{k}}, \tag{3.3}$$

$$\hat{\boldsymbol{\theta}} = \cos\theta\cos\phi\hat{\mathbf{i}} + \cos\theta\sin\phi\hat{\mathbf{j}} - \sin\theta\hat{\mathbf{k}}, \tag{3.4}$$

$$\hat{\boldsymbol{\phi}} = -\sin\phi\hat{\mathbf{i}} + \cos\phi\hat{\mathbf{j}}, \tag{3.5}$$

and place a theoretical weather radar at the origin, assuming the xy plane to be tangent to the surface of the earth at the position of the radar. In this setup, the H/V polarization basis that is of interest in weather radar polarimetry can defined as follows (Zhang et al. 2009):

$$\hat{\mathbf{h}} = \hat{\boldsymbol{\phi}}, \tag{3.6}$$

$$\hat{\mathbf{v}} = -\hat{\boldsymbol{\theta}}, \tag{3.7}$$

where $\hat{\mathbf{h}}$ is the horizontal polarization unit vector $\hat{\boldsymbol{\phi}}$ is the azimuthal unit vector, $\hat{\mathbf{v}}$ is the vertical polarization unit vector and $\hat{\boldsymbol{\theta}}$ is the zenith unit vector. This results in the H polarization direction lying in a plane parallel to the surface of the earth, with a V polarization that is approximately normal to the surface of the earth given that the radar is steered to a small elevation angle. This definition of polarization is chosen in order to directly correlate polarimetric measurements with hydrometeor properties such as canting angle and drop size. It can be immediately noted that the H/V polarization unit vectors are colinear to those that define the Ludwig II definition of cross-polarization, and the two bases are therefore equivalent. As such, the Ludwig II antenna patterns are those that are actually relevant to the performance of polarimetric weather radars.

3.1.3 Origins of Bias Due to Electronic Beam Steering

Now that cross-polarization has been rigorously defined for our purposes, we may examine the physical origins of bias due to electronic beam steering. First, let consider a pair of crossed Hertzian dipoles placed at the origin of a Cartesian coordinate system. The horizontal dipole oriented along the x axis radiates when the H port of the antenna is excited. The vertical dipole oriented along the z axis radiates when the V port of the antenna is excited. The electric field radiated by a dipole can be expressed as:

$$\mathbf{E}(\mathbf{r}) = -\frac{k^2 e^{-jkr}}{4\pi\epsilon r}\big[\hat{\mathbf{r}} \times (\hat{\mathbf{r}} \times \mathbf{M})\big], \tag{3.8}$$

where $\mathbf{r}$ is the position vector of the point at which the field is measured, ϵ is the permittivity of free space, and $\mathbf{M}$ is the moment of the dipole (Ishimaru 1978). The vectors giving the directions of the electric field components normal to the wave propagation direction (along $\hat{r}$) from each dipole can be expressed as follows:

$$\mathbf{e_{d1}} = \hat{\mathbf{j}} - (\hat{\mathbf{i}} \sin\theta\cos\phi + \hat{\mathbf{j}} \sin\theta\sin\phi + \hat{\mathbf{k}} \cos\theta)\sin\theta\sin\phi, \tag{3.9}$$

$$\mathbf{e_{d2}} = \hat{\mathbf{k}} \sin^2\theta - (\hat{\mathbf{i}} \cos\phi + \hat{\mathbf{j}} \sin\phi)\sin\theta\cos\theta, \tag{3.10}$$

where $\mathbf{e_{d1}}$ is the vector corresponding to radiation from the horizontal dipole and $\mathbf{e_{d2}}$ corresponds to radiation from the vertical dipole (Zhang et al. 2009). Projection of these unit vectors onto the H/V polarization basis yields the following results:

$$\hat{\mathbf{h}} \cdot \mathbf{e_{d1}} = \hat{\boldsymbol{\phi}} \cdot \mathbf{e_{d1}} = \cos\phi, \tag{3.11}$$

$$\hat{\mathbf{v}} \cdot \mathbf{e_{d1}} = -\hat{\boldsymbol{\theta}} \cdot \mathbf{e_{d1}} = -\cos\theta\sin\phi, \tag{3.12}$$

$$\hat{\mathbf{h}} \cdot \mathbf{e_{d2}} = \hat{\boldsymbol{\phi}} \cdot \mathbf{e_{d2}} = 0, \tag{3.13}$$

$$\hat{\mathbf{v}} \cdot \mathbf{e_{d2}} = -\hat{\boldsymbol{\theta}} \cdot \mathbf{e_{d2}} = \sin\theta. \tag{3.14}$$

Note that the "H" dipole does not radiate exclusively into the H direction of our polarization basis. To better visualize this effect, a spherical grid corresponding to the radiated polarization directions for the dipoles has been superimposed on a second spherical grid depicting the H/V polarization directions (i.e., the Ludwig II basis) that we have defined for weather radars in Figure 3.3a. Observe that in the principal planes of our crossed dipole antennas ($\theta = 0$ or $\phi = 0$) the radiated field aligns exactly with the H/V basis, but the radiation from the horizontally oriented dipole bends away from the H polarization direction as one moves further away from those

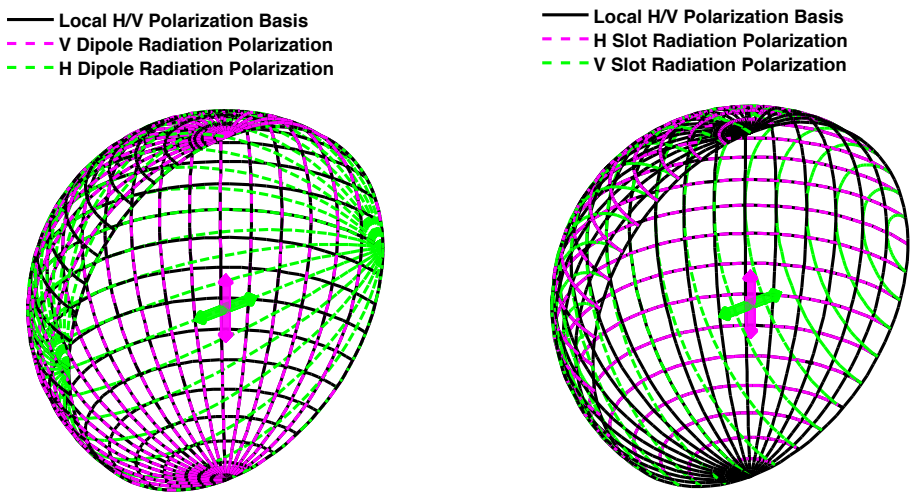

(a) (b)

Figure 3.3: Overlaid spherical grids representing the H/V polarization basis and and the polarization of the radiation from a pair of elements, represented by the pair of crossed arrows.In (a) the elements are dipoles and in (b) they are complementary apertures.

planes. Meanwhile, the V dipole radiation aligns with the V polarization direction at any angle. This translates to the normalized crossed-dipole element patterns shown in Figure 3.4. While the crossed-dipole model is appealing for its simplicity in conveying the basic idea of how polarimetric bias might arise, it does not describe the exact mechanism through which this bias arises in the microstrip patch arrays that are used in most modern phased array radars. In order to understand the biases that arise in microstrip patch arrays, it is instructive to first examine how biases arise in aperture antennas. From Babinet's principle, as modified for electromagnetics (Booker and Others 1946), it can be shown that an aperture complementary to a dipole will radiate with transposed electric and magnetic field oscillation directions

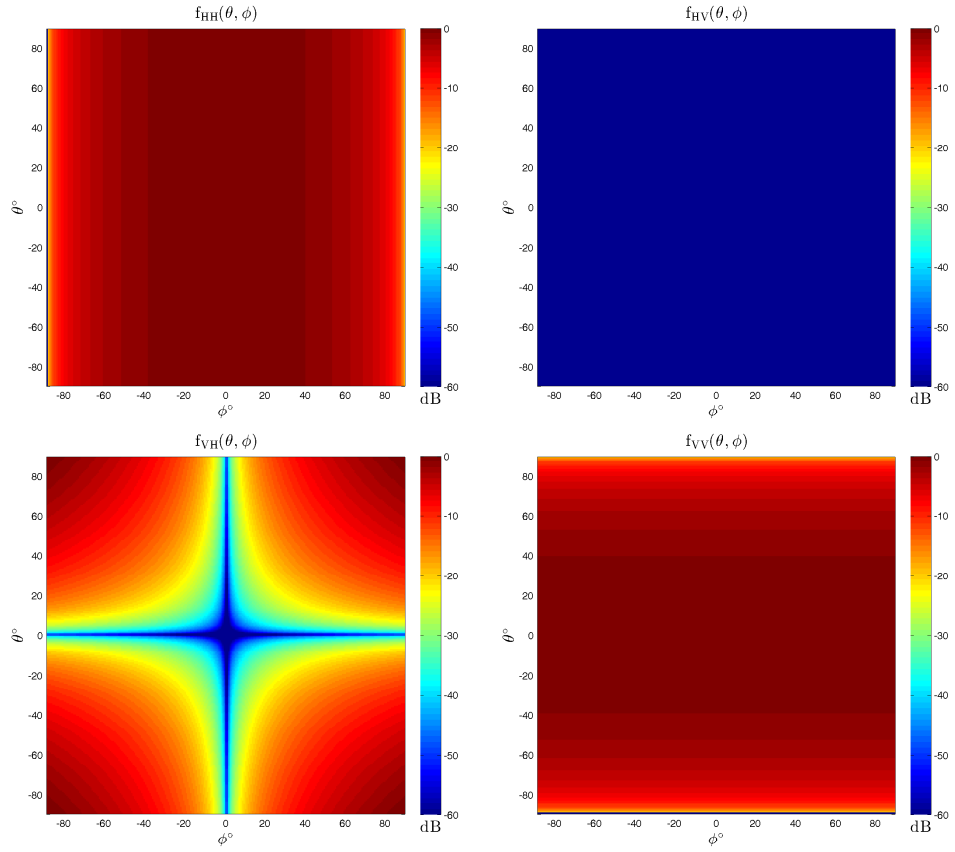

Figure 3.4: Normalized element patterns for a pair of crossed Hertzian dipoles. Note that the radiation from the vertically oriented dipole corresponds exactly with V polarization direction, yielding $f_{\mathrm{HV}}(\theta, \phi) = 0$. Meanwhile, the cross-polar radiation from the horizontally oriented dipole increases in magnitude with distance from the principal planes of the radiating element.

relative to the original dipole. A similar set of e vectors in (θ,ϕ) can be constructed normal to those derived for crossed dipoles and projected onto a (θ, ϕ) surface (Lei et al. 2013):

$$\hat{\mathbf{h}} \cdot \mathbf{e_{s1}} = \hat{\boldsymbol{\phi}} \cdot \mathbf{e_{s1}} = \cos\theta \sin\phi, \tag{3.15}$$

$$\hat{\mathbf{v}} \cdot \mathbf{e_{s1}} = -\hat{\boldsymbol{\theta}} \cdot \mathbf{e_{s1}} = \cos\phi, \tag{3.16}$$

$$\hat{\mathbf{h}} \cdot \mathbf{e_{s2}} = \hat{\boldsymbol{\phi}} \cdot \mathbf{e_{s2}} = \sin\theta, \tag{3.17}$$

$$\hat{\mathbf{v}} \cdot \mathbf{e_{s2}} = -\hat{\boldsymbol{\theta}} \cdot \mathbf{e_{s2}} = 0, \tag{3.18}$$

where $\mathbf{e_{s1}}$ corresponds to the horizontally aligned aperture, which is excited by the V port of the antenna, and $\mathbf{e_{s2}}$ corresponds to the vertically aligned aperture, which is excited by the H port of the antenna. The properties of the H and V radiating elements are reversed. The H radiation is now perfectly aligned with the H polarization direction at any angle, and the V radiation is misaligned with the V polarization direction to an increasing degree as one moves away from the principal planes of the antenna. This effect is shown in Figure 3.3b, and corresponding element patterns are shown by Figure 3.5. Now that we have developed some understanding of the polarization characteristics of idealized apertures, we are well equipped for a qualitative discussion of the polarization characteristics of microstrip patch antennas. A microstrip patch radiates from the fringing fields at its edges, as illustrated in Figure 3.6. For a mode excited within the patch corresponding to a given polarization, one pair of edges will have uniform fringing fields that will actually radiate, while the other two edges will have sinusoidally varying fringing fields that interfere with each other destructively in the principal planes of the patch (Balanis 2016). In contrast

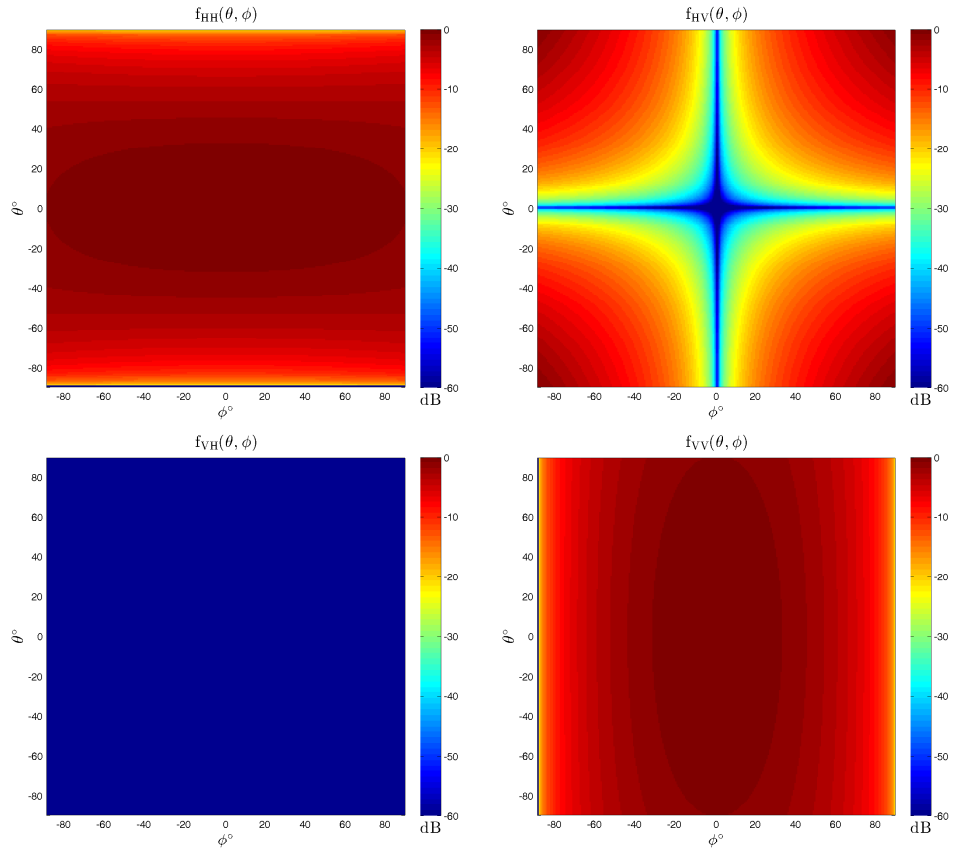

Figure 3.5: Normalized element patterns for a pair of crossed infitesimal apertures, obtained through the application of Babinet's principle. The H and V radiation properties are essentially transposed. Here, $f_{\mathrm{VH}}(\theta,\phi) = 0$ due to the radiation from the horizontally radiating aperture existing entirely in the H polarization direction. The cross-polar fields from the vertically radiating aperture increase in magnitude with distance from the principal planes.

to the non-radiating edges, the effective apertures at the radiating edges interfere constructively at broadside, resulting in a more focused pattern than that of a single aperture. For the H and V radiating modes of the patch, one can perform a similar projection to that used in finding the polarization characteristics of dipoles and apertures (Lei et al. 2013):

$$\hat{\mathbf{h}} \cdot \mathbf{e_{p1}} = \hat{\boldsymbol{\phi}} \cdot \mathbf{e_{p1}} = \cos\theta \sin\phi f_v(\theta, \phi), \tag{3.19}$$

$$\hat{\mathbf{v}} \cdot \mathbf{e_{p1}} = -\hat{\boldsymbol{\theta}} \cdot \mathbf{e_{p1}} = \cos\phi f_v(\theta, \phi), \tag{3.20}$$

$$\hat{\mathbf{h}} \cdot \mathbf{e_{p2}} = \hat{\boldsymbol{\phi}} \cdot \mathbf{e_{p2}} = \sin\theta f_h(\theta, \phi), \tag{3.21}$$

$$\hat{\mathbf{v}} \cdot \mathbf{e_{p2}} = -\hat{\boldsymbol{\theta}} \cdot \mathbf{e_{p2}} = 0, \tag{3.22}$$

where $\mathbf{e_{p1}}$ corresponds to the horizontally aligned edges of the patch, which are excited by the V port of the antenna, and $\mathbf{e_{p2}}$ corresponds to the vertically aligned edges of the patch, which are excited by the H port of the antenna. One may note that these expressions are identical to those for a single aperture except for the terms $f_v(\theta, \phi)$ and $f_h(\theta, \phi)$, which are introduced to account for both the fact that we are now modeling an aperture pair, rather than a single aperture, and to account for finite dimensions, as we are no longer discussing something so idealized as the complementary aperture to a Hertzian dipole. These functions are given as follows (Lei et al. 2013):

$$f_h(\theta, \phi) = \frac{\sin\left(\frac{k_0 L}{2}\cos\theta\right)}{\frac{k_0 L}{2}\cos\theta} \cos\left(\frac{k_0 L_e}{2}\sin\theta\sin\phi\right), \tag{3.23}$$

$$f_v(\theta, \phi) = \frac{\sin\left(\frac{k_0 L}{2}\sin\theta\sin\phi\right)}{\frac{k_0 L}{2}\sin\theta\sin\phi} \cos\left(\frac{k_0 L_e}{2}\cos\theta\right), \tag{3.24}$$

where k_0 is the free-space wavenumber, L is the physical length of the patch edges, and L_e is an effective patch length that accounts for the extent of the fringing fields past the physical patch edges. It should also be noted that the above expression neglects the contribution of the non-radiating edges, which do in fact radiate to some extent away from the principal planes of the array. When these fields are accounted for, the radiation induced in V by an excitation on the H port will be non-zero. A realistic set of simulated element patterns that includes this contribution is shown in Figure 3.7.

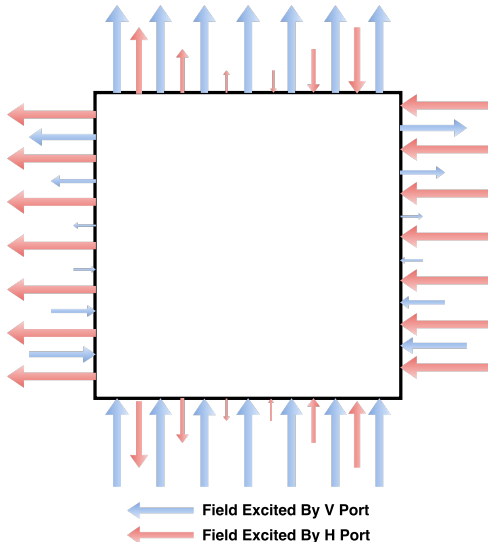

Figure 3.6: Diagram of fringing fields induced at each edge of a microstrip patch when each port is excited. Fringing fields are constant along the radiating edges corresponding to each polarization, while the non-radiating edges are characterized by sinusoidally varying fringing fields.

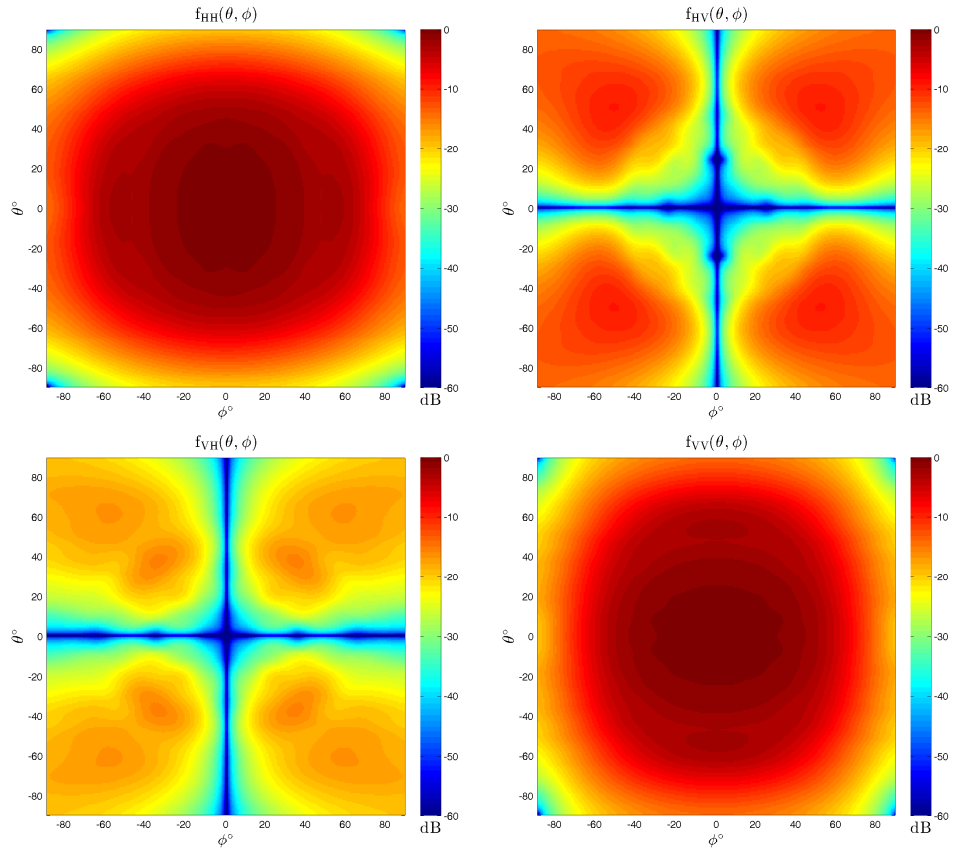

Figure 3.7: Copolar and cross-polar radiated fields of a patch antenna as simulated through HFSS. The effective dual apertures of the patch at each polarization make the copolar patterns more focused than those for an individual aperture. Both cross-polar patterns are non-zero. For $f_{\mathrm{HV}}(\theta,\phi) = 0$, the primary contributor is the radiation behavior intrinsic to apertures. $f_{\mathrm{VH}}(\theta,\phi) = 0$, by contrast, is non-zero primarily due to radiiation from the "non-radiating" edges away from the principal planes of the element. Reprinted from Byrd et al. (2016) © 2016 IEEE.

3.1.4 Mechanical Elevation Tilt

An additional source of cross-polar fields is mechanical elevation tilt. This source of bias was explored in detail by Orzel (2015) for the case of a mechanically tilted array with electronic steering only in the azimuthal direction. His work is expanded on here to encompass the case of an array with two-dimensional electronic beam steering. Assume an array is positioned at the origin of a three-dimensional Cartesian coordinate system xyz with its broadside direction oriented along the x axis. A set of Ludwig II polarization measurements is taken with spherical unit vectors defined using Equation 3.3. These polarization measurements correspond, as previously mentioned, to the meteorological convention for H/V polarization. Now, allow the array to be tilted upward in the $\hat{\boldsymbol{\theta}}$ direction by some angle θ_e. Defining the new broadside direction of the array as the x' axis, a new coordinate system $x'y'z'$ can be defined, as illustrated in Figure 3.8a. Coordinates in this system are related to those in xyz as follows:

$$x' = x\cos\theta_{\mathrm{e}} + z\sin\theta_{\mathrm{e}}, \tag{3.25}$$

$$y' = y, \tag{3.26}$$

$$z' = -x\sin\theta_{\mathrm{e}} + z\cos\theta_{\mathrm{e}}. \tag{3.27}$$

The first effect of this realignment of the array is that steering angles relative to the array (θ', ϕ') no longer correspond to steering angles in the absolute coordinate system (θ, ϕ). The two sets of directions are related as follows:

$$\theta' = \arccos\left(\cos\theta\cos\theta_{\mathrm{e}} - \sin\theta\cos\phi\sin\theta_{\mathrm{e}}\right), \tag{3.28}$$

$$\phi' = \arctan\left(\frac{\sin\theta\sin\phi}{\sin\theta\cos\phi\cos\theta_{\mathrm{e}} + \cos\theta\sin\theta_{\mathrm{e}}}\right). \tag{3.29}$$

Additionally, this new array-relative coordinate system is now the one that corresponds to our polarimetric pattern measurements, as they are necessarily only valid given correct assumptions about orientation with respect to the array face. From the $x'y'z'$ coordinate system, we can calculate a new set of unit vectors $\hat{\theta}', \hat{\phi}'$ that correspond to our measured polarization basis. Assuming that our original xy plane corresponds to the surface of the earth, our measured polarization basis no longer corresponds to the H/V polarization basis $\hat{\boldsymbol{\theta}}, \hat{\boldsymbol{\phi}}$ as defined for hydrometeors. Our measured polarization has now effectively been rotated away from the H/V basis by some angle γ at each angular position. This misalignment of polarization bases is depicted in Figure 3.8b. The angle γ can be calculated as a functon of the elevation angle and the steering angle in both the array-relative and absolute coordinate systems:

$$\gamma = \arccos\left(\cos\theta_{\mathrm{e}}\sin\phi\sin\phi' + \cos\phi\cos\phi'\right). \tag{3.30}$$

With γ known, we can account for the change in polarization basis by projecting our radiated fields into the H/V polarization basis on transmit and back into the measured coordinate system on receive. This is accomplished through the incorporation of a

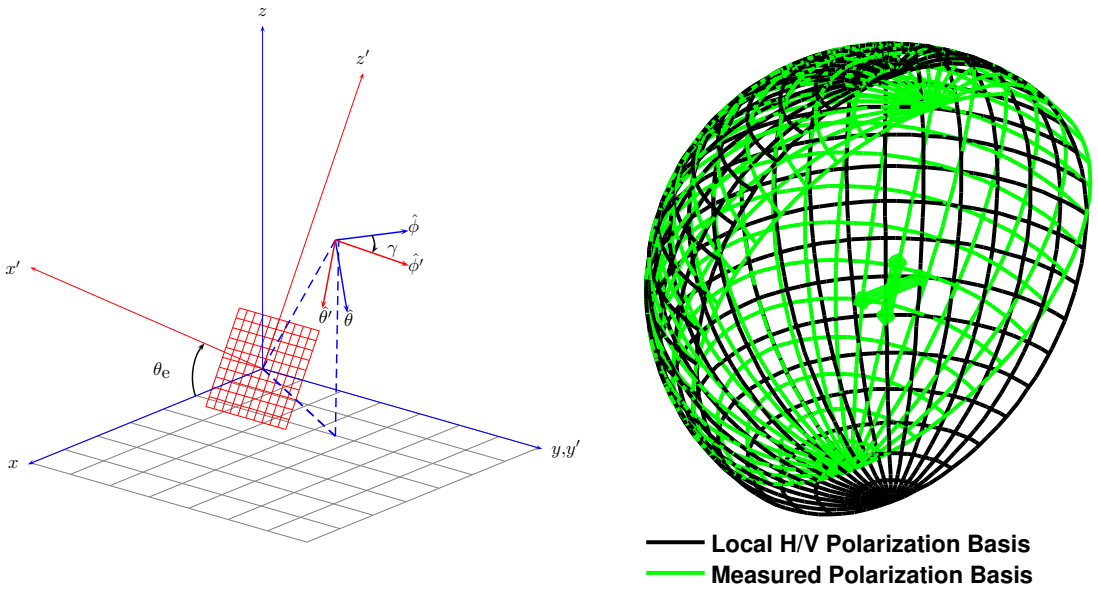

(a) (b)

Figure 3.8: a) Coordinate transformation introduced when a mechanical elevation tilt is applied to the array. xyz is the absolute coordinate space and $x'y'z'$ is the coordinate system transformed by applying the elevation tilt θ_e. ϕ, θ and ϕ', θ' are the tangential unit vectors in the absolute and transformed coordinate spaces respectively. γ is the angle of rotation between the two unit vectors. The red mesh represents the array face. Reprinted from Byrd et al. (2016) © 2016 IEEE. b) Visualization of the misalignment of polarization bases resulting from applying mechanical tilt to an array.

rotation matrix into our model of polarimetric phased array transmission, scattering, and reception. Thus, we modify Equation 3.2 to yield the following:

$$\mathbf{V'_{Rx}} = \mathbf{F^T P^T S' P F V_{Tx}}, \tag{3.31}$$

where:

$$\mathbf{P}(\gamma) = \begin{bmatrix} \cos\gamma & \sin\gamma \\ -\sin\gamma & \cos\gamma \end{bmatrix}, \tag{3.32}$$

$$\mathbf{P}(-\gamma) = \mathbf{P^{-1}}(\gamma) = \mathbf{P^T}(\gamma). \tag{3.33}$$

3.2 Techniques for Mitigation

In anticipation of the proliferation of polarimetric phased arrays, a number of methods have been proposed in the literature for the mitigation of measurement error due to cross-polar fields. These methods span a wide range of approaches to the problem. Some are based around design of the transmitted signal, while others rely on manipulating the geometry of the array or the design of the radiating element. Each method has associated advantages and drawbacks which need to be carefully characterized. This section will provide a brief description of a number of these proposed bias mitigation methods, with a particular focus on those chosen to serve as test cases for the simulator described later in this work.

3.2.1 Correction Matrices

The method of correction matrices (Zhang et al. 2009; Fulton 2011; Lei et al. 2013) was one of the earliest proposed methods for the mitigation of cross-polar biases.

The theoretical foundation of the method is simple. Consider Equation 3.1. If we know the value of the radiation patterns of the array at angle θ_0, ϕ_0 when the array is steered to that same angle (in other words, if we know the value of the radiation patterns at the beam peak) we may construct a pair of correction matrices:

$$\mathbf{C_{Tx}} = \begin{bmatrix} F_{\mathrm{hh}}(\theta_0, \phi_0, \theta_0, \phi_0) & F_{\mathrm{hv}}(\theta_0, \phi_0, \theta_0, \phi_0) \\ F_{\mathrm{vh}}(\theta_0, \phi_0, \theta_0, \phi_0) & F_{\mathrm{vv}}(\theta_0, \phi_0, \theta_0, \phi_0) \end{bmatrix}^{-1} \tag{3.34}$$

$$\mathbf{C_{Rx}} = \begin{bmatrix} F_{\mathrm{hh}}(\theta_0, \phi_0, \theta_0, \phi_0) & F_{\mathrm{vh}}(\theta_0, \phi_0, \theta_0, \phi_0) \\ F_{\mathrm{hv}}(\theta_0, \phi_0, \theta_0, \phi_0) & F_{\mathrm{vv}}(\theta_0, \phi_0, \theta_0, \phi_0) \end{bmatrix}^{-1} . \tag{3.35}$$

We can apply these correction matrices to the transmitted signal before excitation of the antenna ports and, similarly, to the received signal before processing. By modifying Equation 3.2 accordingly, we arrive at the following expression for the range-normalized, corrected measured signal received from as scatter located at θ, ϕ:

$$\mathbf{V_{Rx}} = \mathbf{C_{Rx}}\mathbf{F_{Rx}}\mathbf{S}\mathbf{F_{Tx}}\mathbf{C_{Tx}}\mathbf{V_{Tx}}. \tag{3.36}$$

For a scatterer located at the specified steering direction θ_0, ϕ_0:

$$\mathbf{C_{Tx}} = \mathbf{F_{Tx}}^{-1}, \tag{3.37}$$

$$\mathbf{C_{Rx}} = \mathbf{F_{Rx}}^{-1}, \tag{3.38}$$

$$\mathbf{V_{Rx}} = \mathbf{F_{Rx}}^{-1}\mathbf{F_{Rx}}\mathbf{S}\mathbf{F_{Tx}}\mathbf{F_{Tx}}^{-1}\mathbf{V_{Tx}}, \tag{3.39}$$

$$\mathbf{V_{Rx}} = \mathbf{S}\mathbf{V_{Tx}}. \tag{3.40}$$

Effectively, assuming no errors in the composition or application of the correction matrix, all cross-polar effects are canceled and it is as though the scattering matrix of

a particle at beam peak can be measured directly and without error. This approach to the mitigation of polarimetric biases has several major advantages. The first is that it is inexpensive to implement; mixing the transmit excitations and received signals using the correction matrices is a change that can be implemented entirely in software in many radar systems. Additionally, this process allows for any mismatch in the H and V copolar patterns to be corrected in a single step along with the cross-polar biases. The greatest disadvantage of this method is that it requires detailed knowledge of the complete set of polarimetric antennas patterns for any desired steering angle. In many circumstances, this can be difficult to achieve, even more so given the consideration that the radiation characteristics of arrays are not static, but change over time during the course of system operation, due largely to changes in temperature (Fulton 2011). Additionally, this correction (even disregarding any errors in antenna pattern characterization) can only completely nullify the cross-polar fields at a single angle, but scatterers contribute to the received signals over the entire radiation pattern. Returns from scatterers farther away from the beam peak will contain increasingly strong cross-polar components. Therefore, the performance of this method will degrade with increased beamwidth, or in the presence of strong scatterers away from the peak of the main beam.

3.2.2 Pulse-to-Pulse Phase Coding

Another proposed technipue for the mitigation of cross-polar biases is a pulse-to-pulse phase coded SHV (PCSHV) transmit mode (Chandrasekar and Bharadwaj 2009; Zrnić et al. 2014; Ivić and Doviak 2016). Like the correction matrix method, this

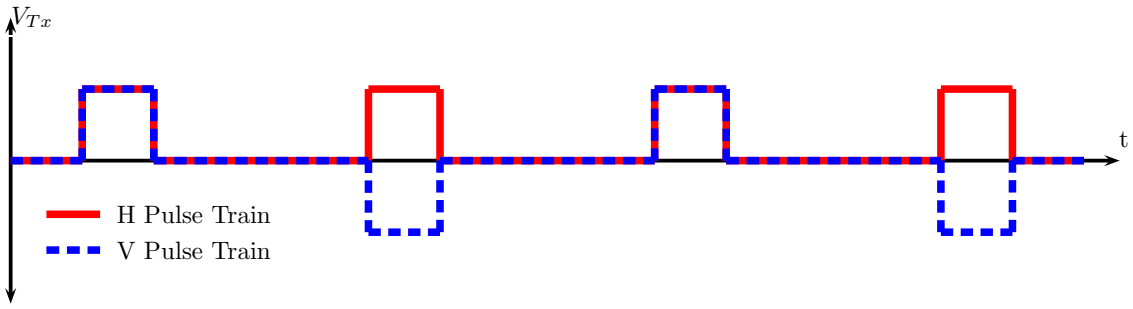

Figure 3.9: Diagram of the H and V transmitted pulse trains for the pulse-to-pulse phase coding implementation described by Zrnić et al. (2014).

method also relies on manipulation of the transmitted and received signals. The basic principal is that the H and V excitations emitted by the transmitter are modulated through multiplication by a pair of orthogonal phase codes $c_h(n)$ and $c_v(n)$, where n is the index of the transmitted pulse. While any pair of orthogonal phase codes could theoretically be utilized, we will consider the simplest possible example as proposed by Zrnić et al. (2014):

$$c_h(n) = 1, \tag{3.41}$$

$$c_v(n) = c(n) = c^*(n) = \exp(jn\pi). \tag{3.42}$$

Put simply, the sign of the excitation on the V port is inverted on each pulse, as shown in Figure 3.9. In this case, we can express the transmit excitations as:

$$V_{\mathrm{h}}^{\mathrm{Tx}}(n) = 1, \tag{3.43}$$

$$V_{\mathrm{v}}^{\mathrm{Tx}}(n) = c_{\mathrm{v}}(n) = c(n)e^{j\beta}, \tag{3.44}$$

where β is the phase of $V_{\mathrm{v}}^{\mathrm{Tx}}(n)$ relative to $V_{\mathrm{h}}^{\mathrm{Tx}}(n)$ prior to phase code application. By inserting these values into Equation 3.1, carrying out the matrix multiplication,

and integrating over some solid angle Ω representing the field of view of the radar, we may express the approximate received signal from all angles as (Zrnić et al. 2014):

$$V_{\mathrm{h}}^{\mathrm{Rx}}(n) \sim \int_{\Omega} [(F_{\mathrm{hh}}^2 s_{\mathrm{hh}} + F_{\mathrm{vh}}^2 s_{\mathrm{vv}}) + (F_{\mathrm{hh}} F_{\mathrm{hv}} s_{\mathrm{hh}} + F_{\mathrm{vv}} F_{\mathrm{vh}} s_{\mathrm{vv}}) e^{j\beta} c(n)] e^{j\psi_{\mathrm{h}}(\theta,\phi)} d\Omega, \quad (3.45)$$

$$V_{v}^{\mathrm{Rx}}(n) \sim \int_{\Omega} [(F_{\mathrm{vv}}^2 s_{\mathrm{vv}} + F_{\mathrm{hv}}^2 s_{\mathrm{hh}}) e^{j\beta} c(n) + (F_{\mathrm{vv}} F_{\mathrm{vh}} s_{\mathrm{vv}} + F_{\mathrm{hh}} F_{\mathrm{hv}} s_{\mathrm{hh}})] e^{j\psi_{\mathrm{v}}(\theta,\phi)} d\Omega, \quad (3.46)$$

where $\psi_h(\theta, \phi)$ and $\psi_h(\theta, \phi)$ represent the phase imposed on the signal through propagation and scattering facts. Note that the dependence of the antennas patterns on angle still applies here, but has been suppressed in the notation for legibility. This expression also assumes that any effects of mechanical elevation tilt have already been accounted for in the antenna pattern values. On receive, the V signal is decoded through multiplication by the conjugate phase code $c^*(n)$ (in this case equivalent to a second multiplication by $c(n)$). The decoded signal is:

$$V_{v}^{\mathrm{Rx}}(n) \sim \int_{\Omega} [(F_{\mathrm{vv}}^2 s_{\mathrm{vv}} + F_{\mathrm{hv}}^2 s_{\mathrm{hh}}) e^{j\beta} + (F_{\mathrm{vv}} F_{\mathrm{vh}} s_{\mathrm{vv}} + F_{\mathrm{hh}} F_{\mathrm{hv}} s_{\mathrm{hh}}) c(n)] e^{j\psi_{\mathrm{v}}(\theta,\phi)} d\Omega. \quad (3.47)$$

At this point it is prudent to discuss the component parts of each of these equations. The first term in each is the pure copolar signal, given for H and V respectively by:

$$F_{\mathrm{hh}}^2 s_{\mathrm{hh}}, \quad (3.48)$$

$$F_{\mathrm{vv}}^2 s_{\mathrm{vv}}. \quad (3.49)$$

For a perfect antenna without cross-polar fields, this would represent the entirety of the received signal. In the H and demodulated V signals it remains unaffected by the phase coding. The next term is the second-order bias:

$$F_{\mathrm{vh}}^2 s_{\mathrm{vv}}, \quad (3.50)$$

$$F_{\mathrm{hv}}^2 s_{\mathrm{hh}}, \quad (3.51)$$

for H and V, respectively. Like the copolar signal, it remains untouched by the phase coding. However, as it is proportional to the square of a cross-polar field, it will most likely be quite small in magnitude compared to the remaining bias terms:

$$(F_{\mathrm{hh}}F_{\mathrm{hv}}s_{\mathrm{hh}} + F_{\mathrm{vv}}F_{\mathrm{vh}}s_{\mathrm{vv}}), \tag{3.52}$$

$$(F_{\mathrm{vv}}F_{\mathrm{vh}}s_{\mathrm{vv}} + F_{\mathrm{hh}}F_{\mathrm{hv}}s_{\mathrm{hh}}), \tag{3.53}$$

once again, for H and V respectively. These first-order bias terms will generally be the dominant source of error. Fortunately, as the term that is actually modulated by the phase code in the final received signals, they may be largely removed using the PCSHV technique. There are several ways to eliminate the first-order biases from the received PCSHV signals. Chandrasekar and Bharadwaj (2009) suggests the use of spectral processing. It should be note that this work uses the technique in order to make simultaneous co- and cross-polar measurements in SHV mode, not to suppress cross-polar biases in PPARs. However, the technique can nevertheless be utilized to that end. In the spectral processing bias removal method, the phase code effectively imposes an additional Doppler shift on the first-order bias signal, which can then be removed through application of a notch filter at the corresponding Doppler frequency. This approach, however, requires sufficiently broad Nyquist interval so that the spectra to be removed is reasonably separated in frequency from the spectra of the copolar signal. The effects of the first-order bias may also be removed from polarimetric products calculated from unfiltered received signals through integration over a number of pulses corresponding to an integer multiple of the phase code length. To observe why this is true, consider the simple length-2 phase code used as an

example here. The sign of the first-order bias term alternates relative to that of the copolar and second-order bias signals on each pulse. Therefore, estimating received power by averaging over an even number of pulses will effectively cancel the influence of the first-order bias term. It should be noted that neither of these processing techniques will mitigate the effects of second-order biases.

3.2.3 Cylindrical Arrays

Another proposed technique for bias mitigation is to utilize a cylindrical, rather than planar, array geometry (Zhang et al. 2011). The use of a cylindrical polarimetric phased array radar (CPPAR) allows for an alternative method of electronic beam steering in the azimuthal direction. Rather than steering in azimuth by applying a phase delay along the azimuthal axis of the array, the CPPAR steers by commuting the set of active elements around the cylinder such that the steering direction is always centered in azimuth relative to the active sector. Electronic steering in elevation is done in the traditional manner, by applying a phase delay along the vertical dimension of the cylinder. However, since the active array is centered in azimuth with respect to the desired steering direction, this steering will take place in the principal elevation plane of the array, which results in minimal cross-polar radiation. Planar arrays maintain low cross-polar fields along their principal planes due to the fact that radiating elements (as shown in the previous discusssion of biases due to electronic beam steering) generally have cross-polar nulls along their principal planes. Since planar array patterns are obtained by directly multiplying the array factor by the element pattern, this property transfers directly to the entire array.

Nonetheless, things are not so simple for a cylindrical array. Recall from Equation 2.69 that the pattern for a conformal array (of which cylindrical arrays are an example) is formed by a weighted sum of the individual element pattern values in the steering direction. While the individual radiating elements for a cylindrical array still have nulls in their cross-polar fields along the principal planes, it should be noted that the elements in the active sector do not all point in the same azimuthal direction due to the curvature of the cylinder. Therefore, the beam steering direction will not lie in the principal elevation plane of the individual elements outside of the center column of the active sector. Why then, does an active sector of a cylindrical array still maintain relatively low cross-polar fields along its principal planes? The answer is that it takes advantage of another property of the cross-polar element patterns. Namely, the cross-polar fields are point-symmetric in phase about the broadside direction of the element. Therefore, the cross-polar fields from the elements offset from the center of the active sector by some angle ϕ will cancel those offset by some angle $-\phi$.

3.2.4 Other Mitigation Techniques

3.2.4.1 Quasi-Simultaneous H/V

There are several other methods for cross-polar bias mitigation that have been proposed. Quasi-simultaneous horizontal and vertical transmission operates by transmitting a separate H and V pulse in near immediate succession on every PRT, as shown in Figure 3.10 (Zrnić et al. 2014). The effect of this technique is that the cross-polar H signal, the cross-polar V signal, and the copolar signals measured at any instant

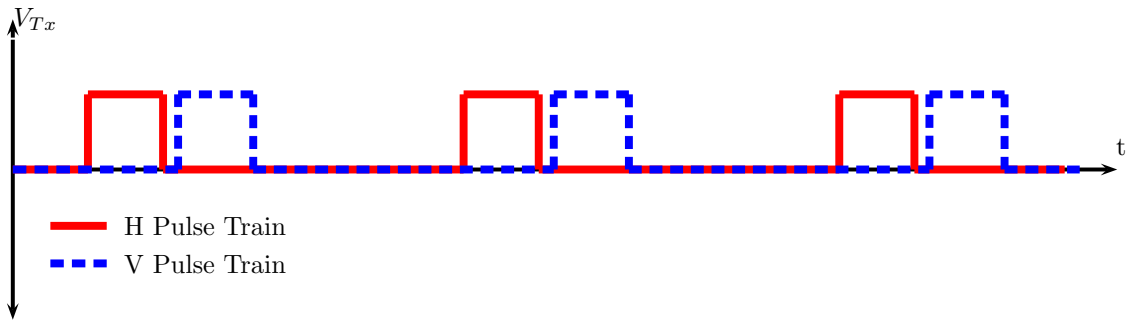

Figure 3.10: Diagram of the H and V transmitted pulse trains for the quasi-simultaneous H/V implementation described by Zrnić et al. (2014).

in time are all contributed by separate range gates. Because the reflections from distributed weather targets are a zero-mean random process (Doviak and Zrnić 2006) and the gates contributing the two cross-polar signals are independent from the copolar gate, the cross-polar contamination should sum incoherently when the measured signal from a gate is integrated over many pulses. These effects result in a significant reduction in the impact of cross-polar bias. However, this technique is vulnerable to sharp reflectivity gradients, which can create scenarios where the cross-polar signal from a high-reflectivity region is able to strongly overwhelm the signal from a nearby low-reflectivity region, regardless of independence. The system would be particularly vulnerable to this pitfall if QSHV were used concurrently with pulse compression. This would result in a scenario where the gates contributing the co- and cross-polar components are not adjacent, but rather offset by some number of gates determined by the pulse compression ratio. The farther apart these gates are, the greater the reflectivity difference that would result from a given reflectivity gradient.

3.2.4.2 Waveform Isolation

Another potential method for obtaining polarization isolation is the use of orthogonal waveforms. This technique was explored for use in parabolic dish antennas in order to allow for the measurement of the cross-polar terms of the scattering matrix in SHV mode when used in conjuction with parabolic dish radars (Giuli et al. 1990, 1993b). However, it also has a clear use-case for the mitigation of cross-polar biases in PPARs. In this mitigation technique, the transmitted waveforms in the H and V polarizations are designed such that they theoretically have zero cross-correlation. This can be achieved through a number of design techniques, such as intra-pulse orthogonal phase coding or opposing frequency chirp directions between the two waveforms. The lack of correlation allows the first-order biases to be filtered from the received signal during the matched filtering process. It should be noted that the second-order biases will not be removed, as those components of the signal actually originate from the same port on which they are received. Because this method removes cross-correlation between H and V at lag-0, it prevents estimation of correlation coefficient and differential phase from lag-0 second order estimates, as noted by Ivić and Doviak (2016).

3.2.4.3 Cross-Polarization Cancellation Elements

One interesting proposal for bias mitigation is setting aside some small proportion of the radiating elements in order to cancel the cross-polar fields (Sánchez-Barbetty et al. 2012). In this method, a small, randomly selected set of the array elements will radiate in the polarization orthogonal to the desired transmit polarization. While the current literature on this technique studies the AHV case in which there is a single

desired polarization, one can imagine that in SHV there would simply be a separate sparse cancellation array for each polarization. The transmitted amplitude and phase of this sparse array must be calculated such that it will cancel the cross-polar fields of the remainder of the array in the desired steering direction. Much like the method of correction matrices, this requires detailed knowledge of the array radiation pattern. This solution is particularly attractive for arrays with all-digital architectures, as they allow for direct control over individual elements at the software level.

3.2.4.4 Hybrid Electronic/Mechanical Scanning

One very simple bias mitigation method for planar arrays is to scan electronically along a single axis, while scanning mechanically along the other (Orzel 2015). This allows the electronic scan to remain in a principle plane of the array at all times, keeping cross-polar radiation at a relative minimum. There are two possible implementations, a mechanical tilt in elevation with electronic scanning, or vice versa. The mechanical elevation tilt has the drawback of inducing cross-polar biases due to rotation of coordinate systems as described earlier in this chapter. Meanwhile, mechanical azimuth scanning has the drawback of inducing the same beam-smearing effects when obtaining PPIs (the most common mode of weather radar operation) that are a drawback of parabolic dish radars

3.2.4.5 Magneto-Electric Dipole Arrays

The final bias mitigation method that we will discuss is the use of a magneto-electric dipole (Wu and Luk 2009; Ge and Luk 2012, 2015) as the radiating element of the

array. This technique attempts to attack the polarization bias problem at the source by using an array element that radiates in the desired polarization basis at all angles. If one were able to radiate in H with an aperture and in V with a dipole, the radiated polarization basis would align with the H/V basis in any beam steering direction. The main drawback to using this method is the increased complexity, difficulty, and cost of antenna fabrication with such a non-traditional design. This is of particular concern for arrays, which for an operational weather radar with beamwidth comparable to the WSR-88D would require many thousands of elements. However, it is possible that new fabrication techniques will reduce the negative impacts of cost and complexity in the near future.

Chapter 4

Simulation of Polarimetric Phased Array Radars

Now that we have discussed the fundamental principles of polarimetric phased arrays, as well as the nature and origins of the unique technical challenges these systems face, it is possible to develop a robust, flexible simulation framework to model their operation. This chapter discusses the details of one possible implementation of such a framework. First, Section 4.1 gives an overview of the current literature on weather radar simulation. Next, the mechanics of the simulator are described. This discussion is divided into two parts. The atmospheric model of the simulator is described in Section 4.2, and the radar system model is described in Section 4.3. The material presented in this chapter adheres closely to format, content, and verbiage of Byrd et al. (2016)

4.1 Prior Work in Weather Radar Simulation

The accuracy of measurements produced by meteorological radars is heavily dependent on the properties of the radar system itself (e.g., operating frequency, radiation fields), as well as accurate calibration and continuous maintenance. Moreover, the relationship between radar measurables and physical characteristics of precipitation (e.g., rainfall rate) depends on the assumed model of observed phenomena and therefore is not unique. For these reasons, weather radar simulators are useful because they

provide complete control of a synthetic weather environment as well as properties of radar used to survey this environment. Such a level of control allows for separation and evaluation of the effects of sensor characteristics (e.g., operating frequency, radiation patterns, etc.) on the radar measurables as well as variation of the microphysical parameters of precipitation (physical state, size, shape, and number density of the hydrometeors).

Weather radar simulators may be classified by whether they produce time series data or directly simulate products such as Doppler moments and polarimetric variables. The latter type of simulator has been used for a number of applications such as rain rate measurement (Krajewski et al. 1993; Giuli et al. 1993a; Anagnostou and Krajewski 1997; Haase and Crewell 2000), sensitivity studies (Caumont et al. 2006), tornadic signature detection (May et al. 2007), feasibility studies for airborne radars (Lupidi et al. 2011), and polarimetric data assimilation (Augros et al. 2013). They are useful for any application where the only requirement for the desired study is a plausible field of radar observables (often reflectivity only) given some specified set of conditions. They are generally less computationally intensive than those that produce time series data. Unfortunately, several of the techniques that are of principal interest to studies of polarimetric bias mitigation, such as phase coded simultaneous horizontal and vertical (PCSHV) (Chandrasekar and Bharadwaj 2009; Zrnić et al. 2014; Ivić and Doviak 2016) and quasi-simultaneous horizontal and vertical (QSHV) (Zrnić et al. 2014; Ivić 2015) transmit modes, require signal modeling at the time series level.

Time series simulators are typically based on the concept of the "scattering center" (SC), which originated with researchers working with wind profilers. SC-based simulators populate the simulation space with artificial scatterers representing some ensemble average of the radar profile of the hydrometeors (or, in the case of wind profilers, refractivity gradients) in the surrounding region of space. Holdsworth and Reid (1995) and, more recently, Venkatesh and Frasier (2013) implemented this concept from a Lagrangian field specification perspective in which the scattering centers moved through the simulation space with the wind field. Later, Muschinski et al. (1999) implemented a similar principle from an Eulerian field specification perspective in which his scattering centers remained fixed in space over the course of the simulation. Time series simulators may be classified based on their fundamental SC mechanics. They can be sorted into two groups based on what each simulated scattering center represents. In the first category of simulator, which uses a homogenous scattering center (HSC) method, each SC represents a group of hydrometeors with single uniform diameter, shape, and orientation. The second type uses a bulk scattering center (BSC) method. In this method each SC represents a group of hydrometeors that follows some specified heterogeneous distribution of diameters, shapes and orientations. HSC-based simulators excel as a tool for studying the effects of physical attributes of precipitation on radar signatures, due to the fact that they allow for fine control of the drop size distribution (DSD), as well as the simulation of precipitation with mixed physical states. However, the emulation of enough SCs to adequately represent the desired distribution of physical characteristics creates heavy computational demands. For this reason, many of them (Chandrasekar and Bringi 1987;

Capsoni and D'Amico 1998; Capsoni et al. 2001) only emulate single resolution volumes. While larger scale simulations based on an HSC method have been developed (Li et al. 2011), computational resources are still a concern for this type of simulation. Particularly if a simulator is to focus primarily on high-fidelity studies of radar system effects, which will require the dedication of a significant amount of computing power, there are clear advantages to making some sacrifices in weather simulation fidelity in order to gain computational efficiency. This can be achieved through BSC based simulations.

One key difference between HSC- and BSC-based simulators is how randomness is introduced at the microphysical level. In HSC systems this occurs through the population of HSCs with random microphysical properties sampled from a distribution based on the weather model. In BSC systems, because each SC has some deterministically calculated set of expected radar observables (generally based on integration of scattering parameters over a DSD calculated from a weather model), randomness is intoduced (if at all) by combining the calculated observables with a weather-like random signal model. Zrnić's seminal work (Zrnić 1975) on the simulation of weather-like signals outlines the basic process of generating single-polarization radar time series as colored Gaussian noise given the preset true values of Doppler moments. In a later paper, Chandrasekar and Bringi (1987) generate the time series through integration of drop size distribution functions and Zrnićs method, taking the first steps toward coupling the statistical time series generation method with physical models of weather. (Galati and Pavan 1995) provided an extension of Zrnić's signal generation method to polarimetric radars in their paper discussing methods for efficient generation of these

signals as well as the mathematical methods to produce horizontal/vertical (H/V) signal pairs with a specified scaling, phase delay, and correlation coefficient.

The dissertation by Torres (2001) is the first example of an SC based simulator that uses a weather-like signal model to emulate a radar signal which consists of contributions from an ensemble of SCs, as opposed to using the model to directly represent the signal received by the radar. The system parameters of the radar such as transmitted waveform specifications were then used to take a weighted average of the scattering center amplitudes and phases, produced using the Zrnić (1975) and Galati and Pavan (1995) methods. Cheong et al. (2004, 2008b), on the other hand, made use of the Lagrangian scattering center framework developed by Holdsworth and Reid by randomly populating the simulation space with BSCs that moved according to the simulated wind field specified by the Advanced Regional Prediction System (ARPS) weather prediction model (Xue et al. 2000, 2001). Rather than implementing Doppler velocities through the parameters of weatherlike signals coupled to the scattering centers, Cheong et al. (2008b) did not simulate any microphysical randomness, instead they modeled the scattering centers as having a deterministic position and allowing the Doppler velocities to emerge through the motion of the scattering centers. This was also the first of the time series simulators to derive its signals from a numerical weather prediction (NWP) model. While this had already been common in simulators that produce Doppler moments and polarimetric variables directly, time series simulators had generally been used for signal processing studies (e.g., evaluation of estimation errors for an arbitrary set of intrinsic radar observable values) in which it was not necessary to realistically simulate a large region of the atmosphere. The BSC

framework (with weatherlike signal based microphysical randomness) was later combined with NWP based atmospheric simulations and used to simulate polarimetric radar returns in works by May (2014) and Lischi et al. (2014).

PPAR technology for weather observations (Weber et al. 2007; Zrnić et al. 2007) demands new considerations for accurate weather radar system simulation. Of particular concern is the problem of cross-polar biases, as discussed in Chapter 3. There has been significant work to characterize these biases using theoretical analysis (Zhang et al. 2008, 2009; Zrnić et al. 2011; Lei et al. 2013) but notably less using simulations (Ivić and Doviak 2016; Ivić 2015, 2016). None of these works, however, evaluates the cross-coupling biases from simulated fields of weather-like radar observables. Because of the dependence of measurement biases on the properties of hydrometeors themselves, it is necessary to simulate observations of realistic weather-like fields in order to estimate the magnitude of the biases that would occur during operation of an actual meteorological PPAR.

Of the simulators surveyed herein, only two claim to be able to emulate phased arrays. The simulator implemented by Li et al. (2011) was designed to simulate airborne polarimetric array radars, but the main subjects of interest in the authors' investigations were the impacts of the airborne platform and various microphysical effects, on the polarimetric signals. Therefore, they were able to simply use an illustrative array factor as the antenna pattern and assumed no presence of system-induced cross-polar fields. The simulator implemented by Cheong et al. (2008b) simulates arrays with greater flexibility, but still with significant limitations. This simulator operates through specification of the element positions rather than an array factor, and it is

capable of generating a time series signal for each individual element. However, it also assumes no presence of cross-polar fields, and only models imaging radars (it does not allow for beamforming on transmit). In addition, it only offers an incomplete polarimetric characterization of scatterers, implementing differential reflectivity, but not differential phase or correlation coefficient. The reasons presented above are the motivation for the development of weather radar simulator capable of modeling polarimetric phased arrays accurately enough to conduct a detailed study of their limitations or the proposed techniques to overcome them.

4.2 Atmospheric Simulation

4.2.1 Parameterization of Radar Observables

The simulator uses the output of the ARPS model (Xue et al. 2000, 2001) to emulate realistic atmospheric conditions. However, this model does not directly provide the radar observables necessary to compose time series data. Rather, it provides meteorological information about the state of the atmosphere. This must be coupled with assumptions about the DSD, drop shape, and scattering regime of the precipitation present in the simulation volume in order to obtain the parameters necessary to compose a simulated radar return.

ARPS is a fully compressible, non-hydrostatic prediction model that has seen prior use in weather radar simulations by May et al. (2007), Cheong et al. (2008b), and Li et al. (2011). It provides information on the physical state of the atmosphere in the form of a 3-dimensional grid including the components of the wind field u,

v, and w, potential temperature θ, pressure p, the mixing ratios for water vapor q_{v}, cloud water q_{c}, rainwater q_{r}, cloud ice q_{i}, snow q_{s}, and hail q_{h}, as well as turbulent kinetic energy (TKE) used by the 1.5-order subgrid-scale turbulent closure scheme (Xue et al. 2000, 2001, 2003). Currently, the simulator only makes use of the Kessler-type warm rain microphysics. The particular ARPS dataset used to generate the simulations presented in this thesis is a prediction of the 8 May 2003 Oklahoma City, Oklahoma. It uses a 50-m grid spacing initialized from a 20-minute forecast based on a 100-m grid spacing ARPS simulation, that was in turn initialized from the 1800 UTC 8 May National Centers for Environmental Prediction Eta Model as well as several in-situ measurements. The simulation includes assimilation of data from the Oklahoma City WSR-88D. Xue et al. (2014) gives further details of the simulation setup and a detailed meteorological analysis of the results.

The foundation for the conversion of the ARPS state variables into polarimetric radar observables is laid out by Jung et al. (2008) as an intermediate step in a study of polarimetric radar data assimilation. Their work assumes a constrained version of the gamma DSD as proposed by Ulbrich (1983) , expressible as

$$\mathrm{N}(D) = N_0 D^{\mu} \exp(-\Lambda D) \quad (0 < D < D_{max}), \tag{4.1}$$

where D is the drop diameter and N_0, Λ, and μ are the DSD parameters. N_0 (assuming only liquid precipitation) is assumed to have a fixed value of 8×10^6 m^{-4}. Λ varies based on q_{r} according to the following expression (Lin et al. 1983):

$$\Lambda = \left(\frac{\pi \rho_{\mathrm{r}} N_0}{\rho q_{\mathrm{r}}} \right)^{0.25}, \tag{4.2}$$

where ρ is the air density calculated based on p, θ and the ideal gas law, and $\rho_{\mathrm{r}} \approx 1000$ kg m^{-3} is the density of liquid water. μ is estimated from Λ based on the following expression derived by Zhang et al. (2001) through polynomial fitting on the results of disdrometer observations:

$$\mu = -0.016\Lambda^2 + 1.213\Lambda - 1.957. \tag{4.3}$$

In addition, Jung et al. uses the following relation between drop diameter (in mm) and axial ratio r derived by Zhang et al. (2001) :

$$\begin{aligned} r = 1.0148 - 2.0465 \times 10^{-2} D - 2.0048 \times 10^{-2} D^2 \\ +3.095 \times 10^{-3} D^3 - 1.453 \times 10^{-4} D^4. \end{aligned} \tag{4.4}$$

This relation is derived by solving the equilibrium expression for raindrop shape presented by Green (1975) and performing a polynomial fit. This set of assumptions regarding DSD and drop shape, coupled with the T-matrix scattering model (Bringi and Chandrasekar 2001), yields the following results for horizontal reflectivity Z_{H}, and vertical reflectivity Z_{V} after integration of the scattering parameters over the DSD:

$$Z_H = \frac{4\lambda^4 \alpha_{\mathrm{a}}^2 N_0}{\pi^4 |K_{\mathrm{w}}|^2} \Lambda^{-(2\beta_{\mathrm{a}}+1)} \Gamma(2\beta_{\mathrm{a}} + 1) \text{ mm}^6\text{m}^{-3} \tag{4.5}$$

$$Z_V = \frac{4\lambda^4 \alpha_{\mathrm{b}}^2 N_0}{\pi^4 |K_{\mathrm{w}}|^2} \Lambda^{-(2\beta_{\mathrm{b}}+1)} \Gamma(2\beta_{\mathrm{b}} + 1) \text{ mm}^6\text{m}^{-3}, \tag{4.6}$$

where λ is the radar wavelength, $\alpha_{\mathrm{a}} = \alpha_{\mathrm{b}} = 4.28 \times 10^{-4}$, $\beta_{\mathrm{a}} = 3.04$, and $\beta_{\mathrm{b}} = 2.77$. Through the same process of integration, the specific differential phase K_{DP} can be expressed as:

$$K_{DP} = \frac{180\lambda}{\pi} N_0 \alpha_{\mathrm{k}} \Lambda^{-(\beta_{\mathrm{k}}+1)} \ ^\circ\text{km}^{-1}, \tag{4.7}$$

where $\alpha_{\mathrm{k}} = 1.30 \times 10^{-5}$ and $\beta_{\mathrm{k}} = 4.63$. Because the simulator does not model propagation effects directly, it is necessary to convert K_{DP} to differential phase ϕ_{DP}. In order to achieve this, the K_{DP} values for the points in the rectangular ARPS grid are linearly interpolated to a spherical grid with the origin located at the center of the simulated array face. These values are then numerically integrated along each radial from the origin to the furthest extent of the simulation volume. The resulting values of ϕ_{DP} are then interpolated back to the rectangular ARPS grid for use in the simulation.

Jung et al. (2008) does not provide a method for determining values of copolar correlation coefficient $|\rho_{\mathrm{HV}}(0)|$ from ARPS data. In order to calculate this parameter the same assumptions about DSD and axial ratio were used as when calculating the other polarimetric parameters. However, the Rayleigh-Gans model, rather than the T-matrix method, was used to calculate the scattering parameters for each drop size, as outlined by May (2014) (Equations 2.23-2.29). Rather than attempting to provide an analytical expression for $|\rho_{\mathrm{HV}}(0)|$, a numerical approach was taken. First, a family of DSDs was calculated over the full range of Λ values present in the ARPS model. For each of these DSDs the following integral expression (Bringi and Chandrasekar 2001) was solved numerically:

$$|\rho_{\mathrm{HV}}(0)| = \frac{|\int_0^{D_{\mathrm{MAX}}} s^{\mathrm{f}}_{\mathrm{HH}}(D) s^{\mathrm{f}*}_{\mathrm{VV}}(D) N(D)\, dD|}{\sqrt{\int_0^{D_{\mathrm{MAX}}} |s^{\mathrm{f}}_{\mathrm{HH}}|^2 N(D)\, dD \int_0^{D_{\mathrm{MAX}}} |s^{\mathrm{f}}_{\mathrm{VV}}|^2 N(D)\, dD}}, \tag{4.8}$$

where $s^{\mathrm{f}}_{\mathrm{HH}}(D)$ and $s^{\mathrm{f}}_{\mathrm{VV}}(D)$ are the horizontally and vertically copolar forward scattering parameters for a raindrop of diameter D. At each point in the ARPS grid, a $|\rho_{\mathrm{HV}}(0)|$ value was then linearly interpolated from the precalculated integrals based

on the value of Λ at that point. One additional parameter that must be calculated from the ARPS table is a partial spectrum width $\tilde{\sigma}_{\mathrm{v}}^2$ which is spectrum width for the small average subregion of a resolution volume occupied by each SC. The square of the spectrum width over a resolution volume σ_{v}^2 can be expressed as a sum of several contributing factors:

$$\sigma_{\mathrm{v}}^2 = \sigma_{\mathrm{s}}^2 + \sigma_{\alpha}^2 + \sigma_{\mathrm{d}}^2 + \sigma_{\mathrm{o}}^2 + \sigma_{\mathrm{t}}^2, \tag{4.9}$$

where σ_{s}^2 is due to shear, σ_{α}^2 is a result of antenna motion, σ_{d}^2 arises from varying speeds of fall for different hydrometeors, σ_{o}^2 is due to hydrometeor oscillation and σ_{t}^2 is the contribution of turbulence (Doviak and Zrnić 2006). σ_{α}^2 is not relevant to electronically scanning arrays, σ_{o}^2 does not apply here as our simulator does not model drop oscillation, and σ_{t}^2 is accounted for by the random component of the scattering center velocities. Therefore, $\tilde{\sigma}_{\mathrm{v}}^2$ can be expressed as (Doviak and Zrnić 2006):

$$\tilde{\sigma}_{\mathrm{v}}^2 = \sigma_{\mathrm{s}}^2 + \sigma_{\mathrm{d}}^2 \tag{4.10}$$

$$\sigma_{\mathrm{d}}^2 = (\sigma_{\mathrm{d0}} \sin\theta_{\mathrm{e}})^2 \tag{4.11}$$

$$\sigma_{\mathrm{s}}^2 = (r_0 \sigma_{\theta} k_{\theta})^2 + (r_0 \sigma_{\phi} k_{\phi})^2 + (\sigma_{\mathrm{r}} k_{\mathrm{r}})^2, \tag{4.12}$$

where r_0 is the range from the radar to the center of the resolution volume, $\sigma_{\mathrm{d0}} \approx 1$ ms^{-1} is the spread in hydrometeor terminal velocity (Doviak and Zrnić 2006), θ_{e} is the angle of elevation of the raindrop, and k_{θ}, k_{ϕ}, and k_{r} are the components of wind shear in each dimension of a spherical coordinate system with the radar at the origin. Calculation of σ_{s}^2 is complicated by the fact that ordinarily σ_{θ} and σ_{ϕ} are the second moments of the antenna pattern beamwidth and σ_{r} is the second moment of the range weighting function. Because we are trying to determine spectrum widths for

some small subregion of the radiation pattern, we must estimate the second moments of the pattern over those regions. First, the average size of the subvolume occupied by each SC is calculated. This is defined as the region surrounding each SC for which it is the nearest SC to any enclosed point. Because the scattering centers are randomly distributed throughout the simulation volume with a uniform probability density function, it can be assumed that this mean subvolume size is uniformly valid throughout the simulation volume. Second, it is assumed that this average subvolume size is sufficiently small such that the hydrometeor properties, the antenna radiation pattern, and the range weighting function can reasonably be approximated as constant within it. Given these assumptions, σ_θ and σ_ϕ may now represent the second moment of a uniform weighting function across each dimension of the solid angle represented by each SC, and σ_r may represent the second moment of a uniform weighting function across the range region represented by each SC. These parameters, Z_H, Z_V, ϕ_{DP}, $|\rho_{HV}(0)|$, and $\tilde{\sigma}_v^2$, together with with the ARPS-specified wind field (used to generate Doppler shifts), comprise all the necessary information to determine the expected parameters of a signal reflected from any point in the simulation volume.

4.2.2 Scattering Centers

A perfectly realistic weather simulator would derive a received signal based on a summation of the reflected signals from every individual hydrometeor in a simulation volume. However, due to the shear number of hydrometeors present in a weather system that spans hundreds or thousands of cubic kilometers, this is computationally intractable for large scale simulations. In order to solve this problem, the proposed

simulator simplifies the calculation by populating the simulation volume with scattering centers, which are point targets with scattering parameters that represent the properties of the entire distribution of hydrometeors within some region in the simulation space.

4.2.2.1 Scattering Center Motion

The scheme used to move the SCs through space is drawn directly from Cheong et al. (2008b). This process is critical to the simulation, as it is the method through which Doppler shifts are introduced to the signals measured by the simulated radar. SCs are initialized at random positions throughout the simulation volume based on some specified sampling density. At every time step corresponding to 1 pulse repetition time (PRT), a received signal is composed through methods discussed later in this chapter. Afterward, the positions of the scatters are updated based on their velocity and the PRT length. This process can be expressed as follows:

$$\mathbf{s}^{(k)}(n) = \mathbf{s}^{(k)}(n-1) + \mathbf{v}^{(k)}(n-1)T_{\mathrm{s}}, \tag{4.13}$$

where $\mathbf{s}^{(k)}(n) = [\, x \; y \; z \,]$ is the postion vector of the kth SC at time step n, $\mathbf{v}^{(k)}(n) = [\, \tilde{u} \; \tilde{v} \; \tilde{w} \,]$ is the velocity vector of the kth SC at time step n, and T_{s} is the PRT length. Each velocity component is obtained from the wind velocities and turbulent kinetic energies of the ARPS grid as follows (Cheong et al. 2008b):

$$\tilde{u} = u + \epsilon\sqrt{\frac{2}{3}\mathrm{TKE}} \tag{4.14}$$

$$\tilde{v} = v + \epsilon\sqrt{\frac{2}{3}\mathrm{TKE}} \tag{4.15}$$

$$\tilde{w} = w + \epsilon\sqrt{\frac{2}{3}\mathrm{TKE}}, \tag{4.16}$$

where ϵ is the output of a normally distributed, unit variance random number generator. SCs that move out of the simulation volume are replaced with new SCs initialized at random positions in the volume. One potential issue with allowing the SCs to move with the wind field is that our effective sampling density can be affected by the divergence of the wind field. If a divergent wind field were allowed to move the SCs for too long without any intervention, it would create a region with few, if any SCs, to return a signal to the simulated radar. To avoid this problem, a small proportion of the SCs are randomly replaced after each PRT.

4.2.2.2 Physical Scattering Center Characteristics

The amplitude and phase of the scattering parameters of each scattering center change in time due to two factors. The first is a pair of unit power weatherlike random signals (one associated with horizontal polarization and the other with vertical) associated with each scattering center. The second is the set of atmospheric conditions at the location of the scattering center at any point in time. The weatherlike signals serve a twofold purpose. First, since each scattering center represents a small region of weather, these signals imbue the reflected signals from the SC with realistic statistical properties consisting of a Rayleigh distributed amplitude and uniformly distributed phase (Doviak and Zrnić 2006). Second, they allow for the correlation coefficient of the H and V signals to be set according to the values calculated from the ARPS model. At the beginning of each simulation the method described by Zrnić (1975) is used to generate two independent random signals with the desired Doppler spectrum, designated $\mathrm{w}_1[n]$ and $\mathrm{w}_2[n]$. The Doppler spectra of these signals have a zero-mean

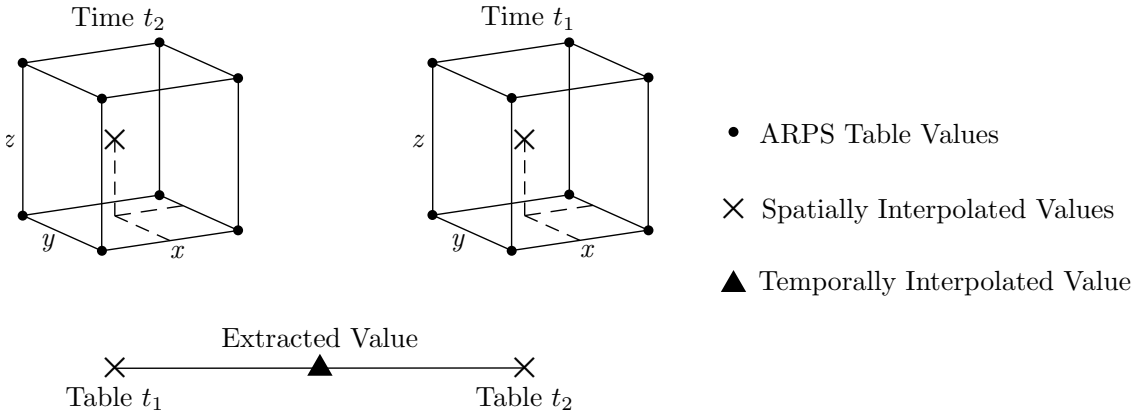

Figure 4.1: This diagram is a representation of the quad-linear interpolation process. To find the radar-observable parameters of an SC at some time point between two ARPS snapshots at times t_1 and t_2, a tri-linear spatial interpolation is first performed at the scatterer's location in each table. Then a linear temporal interpolation is performed between the two results (Adapted from Cheong et al. (2008b).)

Doppler velocity (since this is introduced by the motion of the scattering center in space), unit power, and and a Doppler spectrum width $\tilde{\sigma}$ determined from the ARPS model. $\mathrm{w}_1(n)$ serves as weatherlike signal associated with horizontal polarization. As outlined by Galati and Pavan (1995), $\mathrm{w}_1[n]$ and $\mathrm{w}_2[n]$ are then used to create a third sequence $\mathrm{w}_3[n]$ which will have some desired correlation coefficient $|\rho_{\mathrm{HV}}(0)|$ with $\mathrm{w}_1[n]$. This is done according to the following equation:

$$\mathrm{w}_3[n] = |\rho_{\mathrm{HV}}(0)|\mathrm{w}_1[n] + \sqrt{1 - |\rho_{\mathrm{HV}}|^2}\mathrm{w}_2[n]. \tag{4.17}$$

$\mathrm{w}_3[n]$ becomes the weatherlike signal associated with vertical polarization. The appropriate values of $\mathrm{Z}_{\mathrm{H}}(\vec{r})$, $\mathrm{Z}_{\mathrm{V}}(\vec{r})$, and $\phi_{\mathrm{DP}}(\vec{r})$ for the SC at each time step are found through quad-linear interpolation from the ARPS model as described by Cheong et al.

(2008b) and depicted in Figure 4.1. Once these values have been obtained, they are combined with each SC's associated weatherlike signals to form its final scattering parameters for the current time step:

$$s_{hh}(\vec{r}, n) = \alpha^{-1}\sqrt{Z_H(\vec{r})}w_1[n] \tag{4.18}$$

$$s_{vv}(\vec{r}, n) = \alpha^{-1}\sqrt{Z_V(\vec{r})}w_3[n]\exp(j\phi_{DP}(\vec{r})). \tag{4.19}$$

where α is a scaling factor, equal to the number of scatters per unit volume, introduced to decouple the user-configurable scattering center density from the total returned power, such that the expected reflectivity values at each range gate remain constant regardless of the configured SC density.

4.3 Radar System Model

The primary objective of this simulator is to model the effects of PPAR design on weather observations. As such, the level of detail and flexibility offered by the simulated system model is critical. The simulator incorporates the basic system parameters of center wavelength λ, pulse width τ, and PRT. In order to simulate arrays, it allows for customizable element radiation patterns, positions, and amplitude weights, as well as adjustable transmit polarization. For added realism, it also provides an option to incorporate adjustable random phase and amplitude errors into the array pattern calculation. The mechanical position of the array as well as the beam positions for each scan are also fully configurable. In order to allow for experimentation with advanced beamforming techniques on receive, the simulator provides an option to generate separate time series data for each array element. Transmitted waveforms

are also fully configurable, with their effects modeled through conversion to a range weighting function that accounts for quantization effects (e.g., the effects of generating waveforms through the use of a direct digital synthesizer with a finite number of possible phase and amplitude states). Similarly, the waveform characteristics from pulse to pulse, such as transmit phase and relative amplitude of the H and V pulses, are entirely customizable.

4.3.1 Antenna

A detailed description of the basic model for radiation, scattering, and reception from a dual-polarization array is given in Section 3.1.1. This simulation architecture uses a slightly modified version of that basic model. The first difference between the basic scattering model and the one utilized by the simulator is that we may no longer assume that the constraint of identical element weighting on transmit and receive is valid. It is not uncommon for operational phased arrays to transmit at maximum power across all elements on transmit in order to maximize sensitivity while applying a taper on receive for sidelobe reduction. As such, rather than having four patterns to completely describe the properties of the array, we have eight. Let us introduce a pair of new matrices to the model:

$$\mathbf{F_{Tx}} = \begin{bmatrix} \mathrm{F_{hh}}(\theta,\phi,\theta_0,\phi_0)_{\mathrm{Tx}} & \mathrm{F_{hv}}(\theta,\phi,\theta_0,\phi_0)_{\mathrm{Tx}} \\ \mathrm{F_{vh}}(\theta,\phi,\theta_0,\phi_0)_{\mathrm{Tx}} & \mathrm{F_{vv}}(\theta,\phi,\theta_0,\phi_0)_{\mathrm{Tx}} \end{bmatrix}, \tag{4.20}$$

$$\mathbf{F_{Rx}} = \begin{bmatrix} \mathrm{F_{hh}}(\theta,\phi,\theta_0,\phi_0)_{\mathrm{Rx}} & \mathrm{F_{vh}}(\theta,\phi,\theta_0,\phi_0)_{\mathrm{Rx}} \\ \mathrm{F_{hv}}(\theta,\phi,\theta_0,\phi_0)_{\mathrm{Rx}} & \mathrm{F_{vv}}(\theta,\phi,\theta_0,\phi_0)_{\mathrm{Rx}} \end{bmatrix}, \tag{4.21}$$

allowing us to modify Equation 3.2 to yield:

$$\mathbf{V'_{Rx}} = \mathbf{F_{Rx}} \mathbf{S} \mathbf{F_{Tx}} \mathbf{V_{Tx}}. \tag{4.22}$$

Furthermore, the simulator accounts for the rotation of polarization bases due to mechanical tilt, as described in Section 3.1.4. Therefore, we may introduce the projection matrix $\mathbf{P}(\gamma)$ as in Equation 3.31, which gives us:

$$\mathbf{V'_{Rx}} = \mathbf{F_{Rx}} \mathbf{P^T} \mathbf{S} \mathbf{P} \mathbf{F_{Tx}} \mathbf{V_{Tx}}. \tag{4.23}$$

It should be noted that the definition of the scattering matrix $\mathbf{S}$ as used here differs from its standard usage. In the simulator, it represents the mean scattering parameters of an ensemble of particles rather than those of an individual hydrometeor. Such a reduction of an ensemble of particles to an equivalent point target that has scattering parameters with weatherlike properties is a well established practice in time series weather radar simulators (Torres 2001; May 2014; Lischi et al. 2014). In this case, elements of each scattering matrix $\mathbf{S}$ (representing a point target) account for the fact that scatterers (within a volume represented by $\mathbf{S}$) have different relative ranges for every pulse transmission due to the motion of particles within, as well as across the boundaries of, each volume. The result is that the elements of $\mathbf{S}$ have random real and imaginary parts that are zero-mean, normally distributed functions of sample time, unlike the unchanging scattering matrix of a single scatterer that is not oscillating (Ivić and Doviak 2016). Consequently, elements of $\mathbf{S}$ are functions of range and are semi-coherent along sample time. Consequently, elements on the main diagonal of so modified scattering matrix can be simulated using the approach described in Zrnić (1975), as well as in Galati and Pavan (1995).

Bearing this in mind, we also make several modifications to the scattering matrix. First, we assume that the hydrometeors represented by each scattering center have a zero-mean canting angle. This allows us to approximate the cross-polar terms of the scattering matrix, s_{hv} and s_{vh}, as equal to 0 (Zrnić et al. 2010) and focus on the depolarization induced by the antenna cross-polar fields rather than the scattering media. Additionally, the simulator utilizes a transmission-modified scattering matrix model. In this case that means that the differential propagation phase ϕ_{DP} is incorporated into the copolar V term of the scattering matrix. In reality this effect occurs gradually along the transmitted pulse's propagation path, but to reduce computational complexity this value is precalculated from the ARPS data and applied at the pulse's point of contact with the scattering center. Thus, we introduce a modified scattering matrix for each scattering center:

$$\mathbf{S}' = \begin{bmatrix} s_{\mathrm{hh}}(\mathbf{r}, n) & 0 \\ 0 & s_{\mathrm{vv}}(\mathbf{r}, n) \end{bmatrix}, \tag{4.24}$$

where $s_{\mathrm{hh}}(\mathbf{r}, n)$ and $s_{\mathrm{vv}}(\mathbf{r}, n)$ are the H and V scattering parameters of the scattering center, calculated as a function of its position $\mathbf{r}$ within the ARPS data and the current sample time step n. As previously noted, s_{hh} and s_{vv} are simulated based on the ARPS data using Zrnić (1975) as well as Galati and Pavan (1995). Then, the final expression for the simulator's model used to compute the signals received by the radar is:

$$\mathbf{V}'_{\mathbf{Rx}} = \mathbf{F_{Rx}} \mathbf{P}^{\mathbf{T}} \mathbf{S}' \mathbf{P} \mathbf{F_{Tx}} \mathbf{V_{Tx}}. \tag{4.25}$$

The radiation patterns for the current steering angle exist as a set of lookup tables in azimuth and elevation. For each scattering center, the value of each pattern at

its precise angle relative to the radar is calculated by a bilinear interpolation on the corresponding table.

4.3.2 Signal Model

The simulator accepts a waveform design as a function $f(t)$, which specifies the base-band frequency at a series of time points over the length of the pulse in Hz. Therefore, it easily accommodates techniques, such as pulse compression, which involve phase modulation on transmission. $f(t)$ is then used to generate a phase function (used by the digital-to-analog converter to generate the transmit waveform) as:

$$\phi(t) = 2\pi \int_0^\tau f(t)dt, \tag{4.26}$$

where the integration is performed numerically. To allow for realistic simulation of a direct digital synthesizer, the simulator allows for specification of phase and amplitude quantization through specification of the number of bits allowed to specify each. At this point, the phase quantization is applied. The simulator generates a list of 2^{n_p} possible phase states between zero and 2π, where n_p is the number of bits allowed to specify phase, and rounds each value in $\phi(t)$ to the nearest possible state. This quantized phase function $\phi_q[t]$ is then used to generate a vector of complex waveform samples:

$$w(t) = e^{j\phi_q(t)}. \tag{4.27}$$

Before applying the amplitude quantization, this waveform is decomposed into its quadrature components:

$$I(t) = \mathrm{Re}\{w(t)\}, \tag{4.28}$$

$$Q(t) = \mathrm{Im}\{w(t)\}. \tag{4.29}$$

The simulator then generates a list of 2^{n_a} allowable amplitude states, where n_a is the number of digital-to-analog converter bits, and the values in $I(t)$ and $Q(t)$ are each rounded to the nearest allowable state. We can then calculate the final waveform:

$$w_q(t) = I_q(t) + jQ_q(t), \tag{4.30}$$

where $I_q(t)$ and $Q_q(t)$ are the quantized quadrature components. The range weighting function that would result from a matched filtering operation performed on this waveform can then be calculated as:

$$W(r) = \begin{cases} R_{\mathrm{ww}}\left(\frac{2(r-r_0)}{c}\right), & -\frac{c\tau}{2} < r - r_0 < \frac{c\tau}{2} \\ 0, & \text{otherwise} \end{cases}, \tag{4.31}$$

$$R_{\mathrm{ww}}(l) = \mathrm{acf}\{w_q(t)\} = \int_{-\infty}^{\infty} w_q(t) w_q^*(t-l)dt, \tag{4.32}$$

where r_0 is the range of the center of the resolution volume being sampled and r is the range of the scatterer. By calculating this range weighting function before the actual simulation, we are able to simulate the the transmitted signals $V_{\mathrm{h}}^{\mathrm{Tx}}$ and $V_{\mathrm{v}}^{\mathrm{Tx}}$ as single complex values. To demonstrate this, consider the transmission of a baseband waveform $p(t)$ with pulse length τ, scaled and phase shifted by some complex scalar excitation V_{Tx}. This gives a total baseband signal:

$$P(t) = V_{\mathrm{Tx}} p(t). \tag{4.33}$$

This signal undergoes an ideal upconversion process to the RF frequency of the radar system, at which point it will be denoted $P'(t)$, and is transmitted from an isotropically radiating antenna. It propagates to some range r_0. Assume a set of N scatterers in the radar's field of view. Each of these scatterers has a scattering parameter s_n, where n represents the index of the scatterer. Assuming the pulse was transmitted at time $t = 0$, it will arrive at each scatterer at time $t_n = \frac{r_n}{c}$, where r_n is the range of the nth scatterer from the radar. The signal reflected from each scatterer is simply the transmitted signal phase shifted and attenuated according to scatterer range and scattering parameter to yield a backscattered signal:

$$P'_{\mathrm{b}}(t) = \sum_{n=0}^{N} \frac{e^{-j2\pi k r_n}}{r_n^2} s_n P'(t - t_n), \tag{4.34}$$

where k is the wavenumber of the RF signal. This backscattered signal is then scaled and phase shifted again according to range as it propagates back to the radar. On reception it passes through an ideal downconversion process, giving:

$$P_{\mathrm{r}}(t) = \sum_{n=0}^{N} \frac{e^{-j4\pi k r_n}}{r_n^4} s_n P(t - 2t_n) \tag{4.35}$$

Upon reception, the received signal is passed through an ideal matched filter with an impulse response defined as:

$$h(t) = p^*(-t) \tag{4.36}$$

The final received voltage $V_{\mathrm{r}}(t)$ is the output of this matched filter, which (neglecting filter delays) can be expressed as follows:

$$V_{\mathrm{r}}(t) = h(t) * P_{\mathrm{r}}(t) \tag{4.37}$$

Because convolution is linear, this can be rewritten as:

$$P_{\mathrm{r}}(t) = \sum_{n=0}^{N} \frac{e^{-j4\pi k r_n}}{r_n^4} s_n h(t) * P(t - 2t_n) \tag{4.38}$$

We can then define a weighting function:

$$W'(t) = h(t) * p(t) \tag{4.39}$$

$$= \frac{h(t) * p(t)}{V_{\mathrm{Tx}}} \tag{4.40}$$

$$= p^*(-t) * p(t) \tag{4.41}$$

The time-shift properties of convolution tell us that:

$$W'(t - 2t_n) = h(t) * p(t - 2t_n). \tag{4.42}$$

Combining this result with a change of variables $r = \frac{ct}{2}$, and evaluating at some sample time t_s, we obtain:

$$P_{\mathrm{r}}(t_s) = \sum_{n=0}^{N} \frac{e^{-j4\pi k r_n}}{r_n^4} s_n V_{\mathrm{Tx}} W'\left(\frac{2(r_s - r_n)}{c}\right). \tag{4.43}$$

Because we know that the pulse $p(t)$ is nonzero only for $0 < t < \tau$, we can proceed as follows starting from the definition of convolution:

$$W'(t) > 0,\ 0 < t < 2\tau \tag{4.44}$$

$$W'(t_s - 2t_n) > 0,\ 0 < t_s - 2t_n < 2\tau \tag{4.45}$$

$$W'\left(\frac{2(r_s - r_n)}{c}\right) > 0,\ 0 < \frac{2(r_s - r_n)}{c} < 2\tau \tag{4.46}$$

$$W'\left(\frac{2(r_0 - r_n)}{c}\right) > 0,\ r_0 = \frac{c\tau}{2} - r_s,\ -\frac{c\tau}{2} < r_n - r_0 < \frac{c\tau}{2} \tag{4.47}$$

From there, we can define a range weighting function $W(r)$ in the same form as the weighting function given in Equation 4.31:

$$W(r) = \begin{cases} W'\left(\frac{2(r_n - r_0)}{c}\right), & -\frac{c\tau}{2} < r_n - r_0 < \frac{c\tau}{2} \\ 0, & \text{otherwise} \end{cases} \tag{4.48}$$

This allows us to write a final expression for the received voltage composed from many scatters as:

$$P_{\mathrm{r}}(t_s) = \sum_{n=0}^{N} \frac{e^{-j4\pi k r_n}}{r_n^4} s_n V_{\mathrm{Tx}} W(r_n). \tag{4.49}$$

As stated before, this function can be precalculated from the transmitted waveform and the appropriate value for each scattering center obtained from a lookup table at each range gate with a center corresponding to range r_0 in Equations 4.31 and 4.48. This process is much less computationally expensive than summing a set of reflected waveforms over all scatterers and performing a matched filtering operation during the simulation runtime.

There are four modes of polarimetric signal transmission implemented in the simulator. They include the two most common modes of signal transmission in polarimetric radars (SHV and AHV), as well as PCSHV and QSHV, transmit modes proposed for the mitigation of cross-polar biases (see Sections 3.2.2 and 3.2.4.1). The SHV, AHV, and PCSHV modes can be implemented very directly in the simulation framework based on their definitions. The SHV mode is implemented by simply allowing $V_{\mathrm{h}}^{\mathrm{Tx}}$ and $V_{\mathrm{v}}^{\mathrm{Tx}}$ to be equal in magnitude on each PRT, with any desired constant phase offset. AHV simply sets one of the transmitted signal values equal to zero on each pulse, alternating between H and V on each PRT. PCSHV operates similarly to SHV

but shifts the phase of $V_{\mathrm{v}}^{\mathrm{Tx}}$ by 180° on each PRT. The QSHV implementation is slightly more complex, because the simulation architecture does not have the capability to directly simulate two separate pulses within the same PRT. This difficulty is circumvented by simulating first an H-only pulse, sampled at one set of range gates, and then a V-only pulse sampled at another set of range gates offset from the H range gates by:

$$\delta r = \frac{c\tau}{2}. \tag{4.50}$$

The two independently collected sets of time-series data are then simply added together to form the complete QSHV time-series signal.

4.3.3 Coherent Integration

At each time step, the simulator composes a time series point for every radar resolution volume in the scan. For each resolution volume, the signal is composed as a coherent integration of signals returned from every scattering center within the range annulus defined by the resolution volume's range and the pulse width. This signal can be expressed as:

$$V_{\mathrm{H}} = \sum_{k=0}^{N'-1} \frac{\mathrm{W}(r^{(k)})}{r^{(k)2}} V_{\mathrm{H}}^{\prime(k)} \exp\left(j\frac{4\pi r^{(k)}}{\lambda}\right) + \mathcal{N}_{\mathrm{H}} \tag{4.51}$$

$$V_{\mathrm{V}} = \sum_{k=0}^{N'-1} \frac{\mathrm{W}(r^{(k)})}{r^{(k)2}} V_{\mathrm{V}}^{\prime(k)} \exp\left(j\frac{4\pi r^{(k)}}{\lambda}\right) + \mathcal{N}_{\mathrm{V}}, \tag{4.52}$$

where N' is the number of SCs present in the range annulus, $\mathrm{W}(r)$ is the range weighting function, $r^{(k)}$ is the range of the kth SC, V'_{H} and V'_{V} are the H and V received voltages calculated through Equation 4.23, and $\mathcal{N}_{\mathrm{H}}$ and $\mathcal{N}_{\mathrm{V}}$ are simulated

thermal noise (assumed to be additive white gaussian noise) added to each channel. This process is illustrated in Figure 4.2.

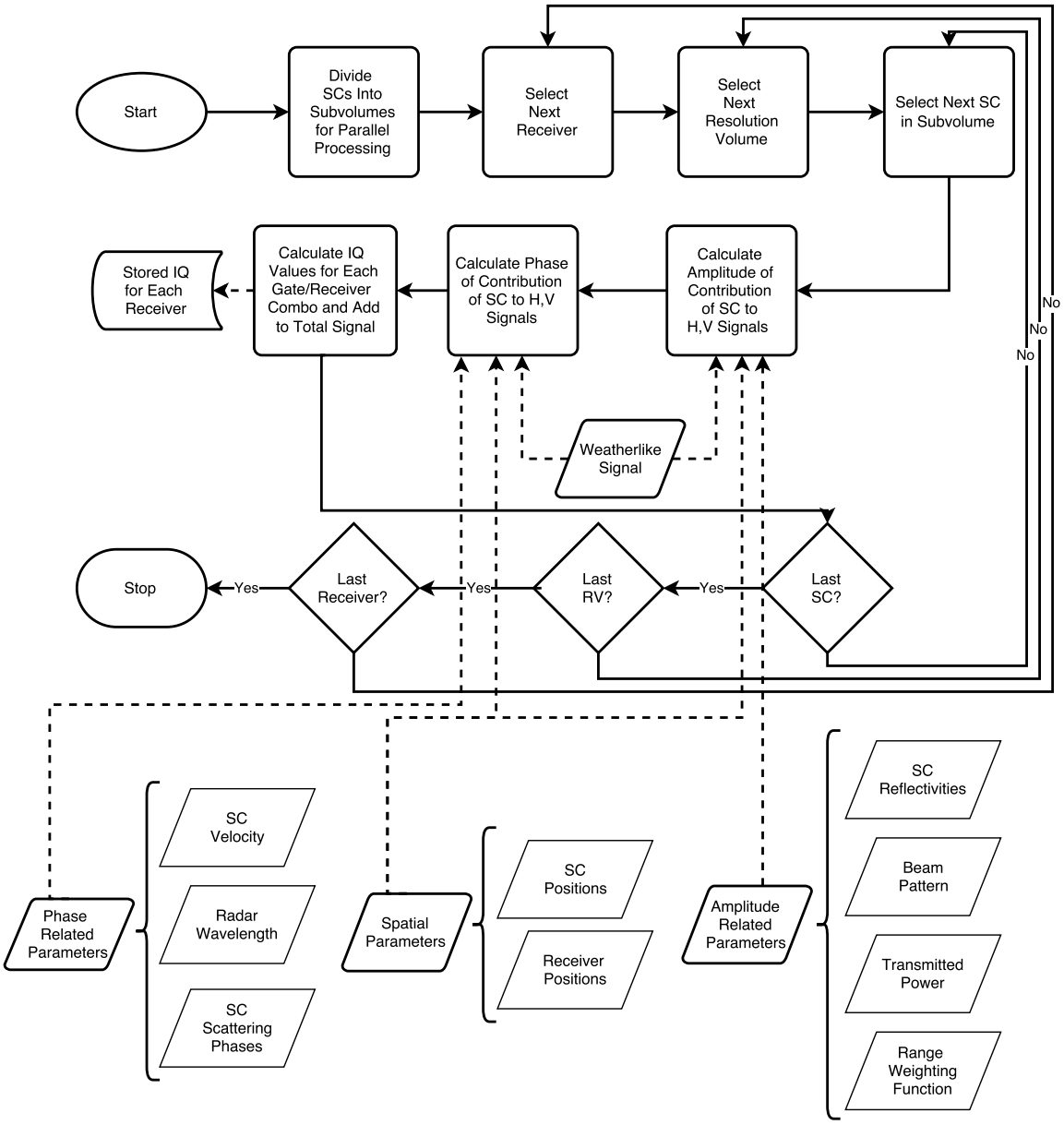

Figure 4.2: Diagram of the coherent integration process. "scattering center" is abbreviated here as SC. The upper portion of the diagram outlines the actual process, while the parallelograms below give a breakdown of the various inputs to the algorithm. Reprinted from Byrd et al. (2016) © 2016 IEEE.

4.4 Current Simulator Implementation

4.4.1 Software Architecture

To perform a simulation, the main emulator program, implemented in MATLAB, first accesses a configuration file, which specifies all of the radar system characteristics as well what ARPS files to use and what subregions of the ARPS data available from those files should be used in the simulation. The emulator then calls an ARPS reader function (also in MATLAB) to extract the data from the .hdf files in which it is stored, calculate the radar observable parameters from the meteorological data, and arrange the results in an easily utilized format. With that done, the emulator initializes the scattering centers and their associated random time-series data, and calculates their initial parameters. At each time series step, the emulator calls the coherent integration function. This function, which is implemented in C as a .mex file, iterates over each resolution volume and composes a time-series sample for each. Once that process is complete, the emulator updates the position and scattering parameters of each scatterer and advances to the next time-series step. Once the simulation is complete, the time-series data is stored in .mat format and can be processed according to the needs of the user. This process is diagrammed in Figure 4.3 The script used to process the data in this work utilizes pulse-pair processing to generate estimates of Z_{H}, Z_{V}, Z_{DR}, v_{r}, $\tilde{\sigma}_{\mathrm{v}}^2$, ϕ_{DP}, and $|\rho_{\mathrm{HV}}(0)|$. It is capable of processing data obtained using any of the four polarimetric transmit modes available in the current simulator software.

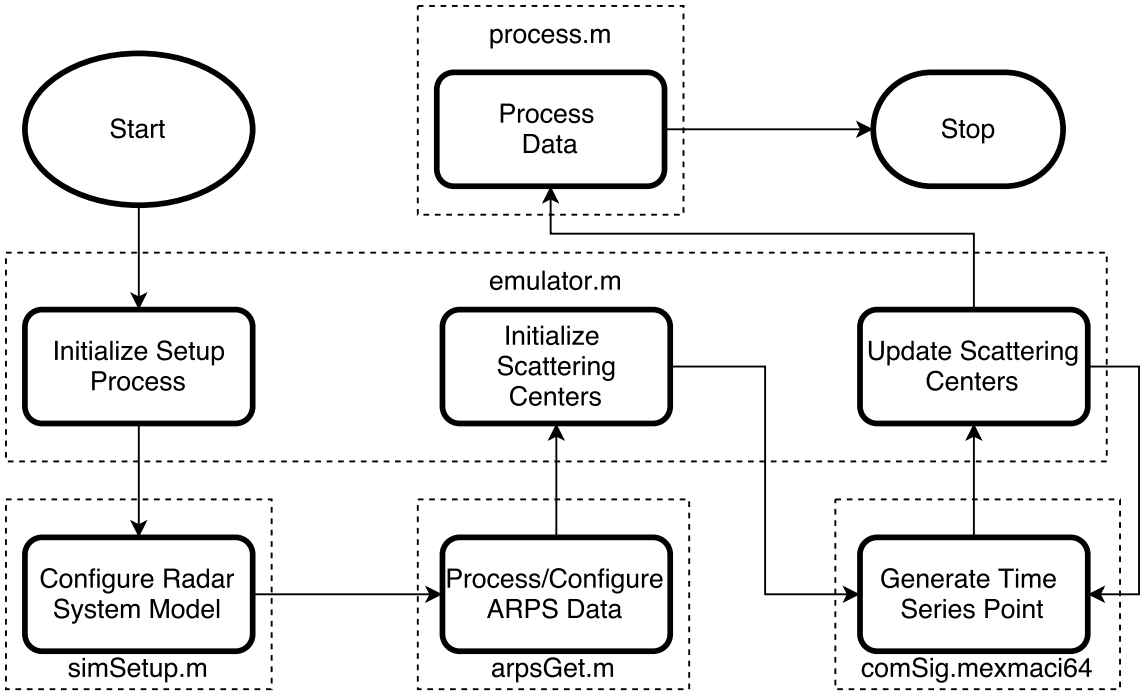

Figure 4.3: This flowchart depicts a high-level view of the simulation process. The processes taking place within each file in the simulation software package are delimited by the dashed boxes.

4.4.2 Simulator Output Examples

In order to demonstrate the basic capabilities of the simulator, a set of illustrative simulations have been carried out. The radar system simulated is a 128×128 element S-band array with a one-degree beamwidth. It uses the element corresponding to the radiation patterns depicted in Figure 3.7. A set of calculated transmit radiation patterns for this array is shown in Figure 4.4 while a set of receive patterns is shown in Figure 4.5. For both simulations the radar system was operated at a 1-ms PRT with an uncompressed 1-μs rectangular pulse, transmitting a linear dual-polarized

signal in SHV mode. For further details on the simulator configuration, see Table 4.1.

Each simulation scans a region from -45 to 45 degrees in azimuth at an elevation of 5°. A set of single-elevation cross-sections of the field of ARPS-derived polarimetric variables used in the simulation is shown in Figure 4.6. The presence of cross-polar fields and the mechanical elevation tilt of the array are varied across the simulations

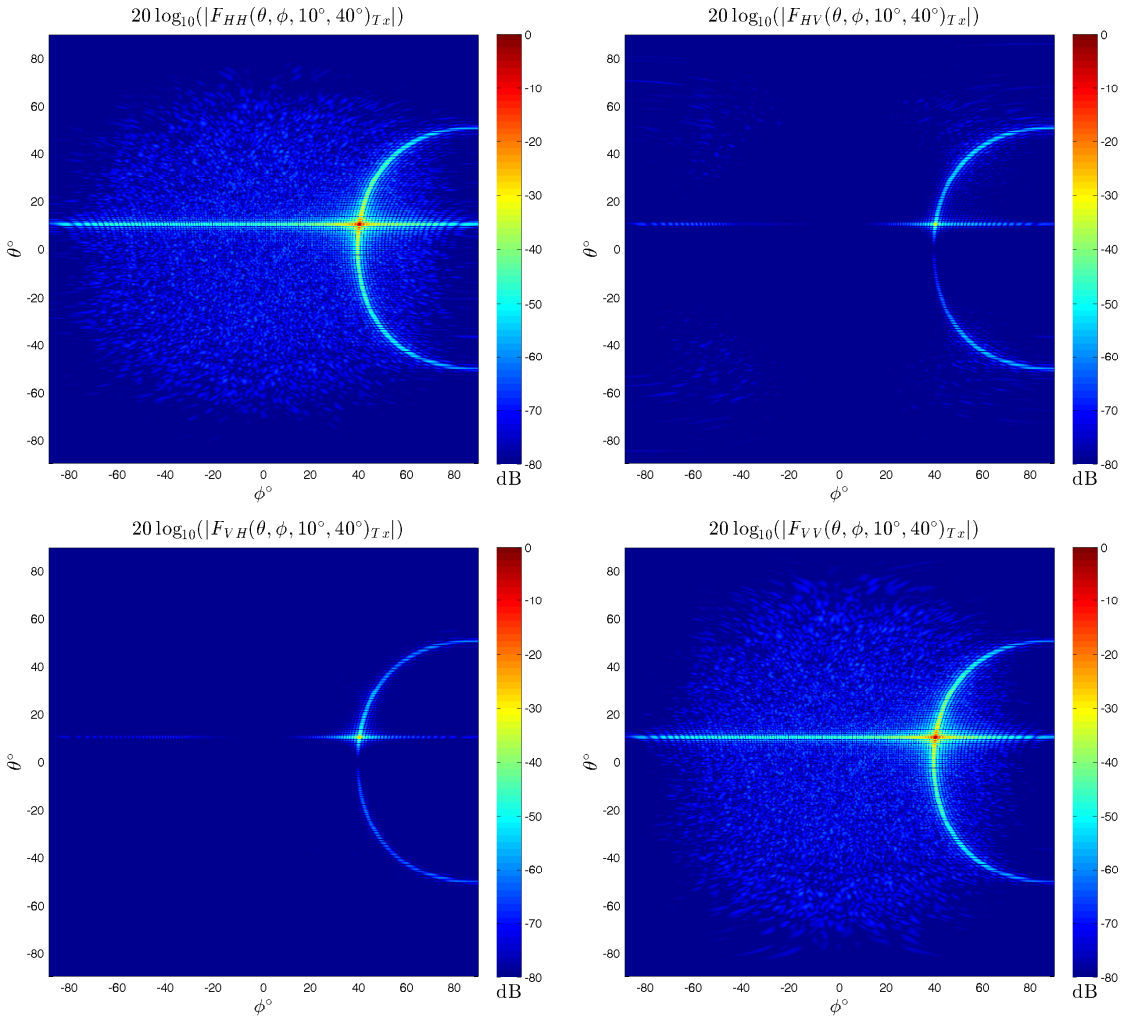

Figure 4.4: Calculated dual-polarization transmit radiation patterns for the simulated array. Spurious sidelobes are a result of random phase and amplitude errors.

to demonstrate the ability of the simulator to model cross-polar biases arising from each of the mechanisms discussed in Chapter 3. The first simulation serves as a reference by which the effects of cross-polar bias can be measured. In this simulation, all cross-polarization effects (due both to antenna pattern and mechanical tilt) were

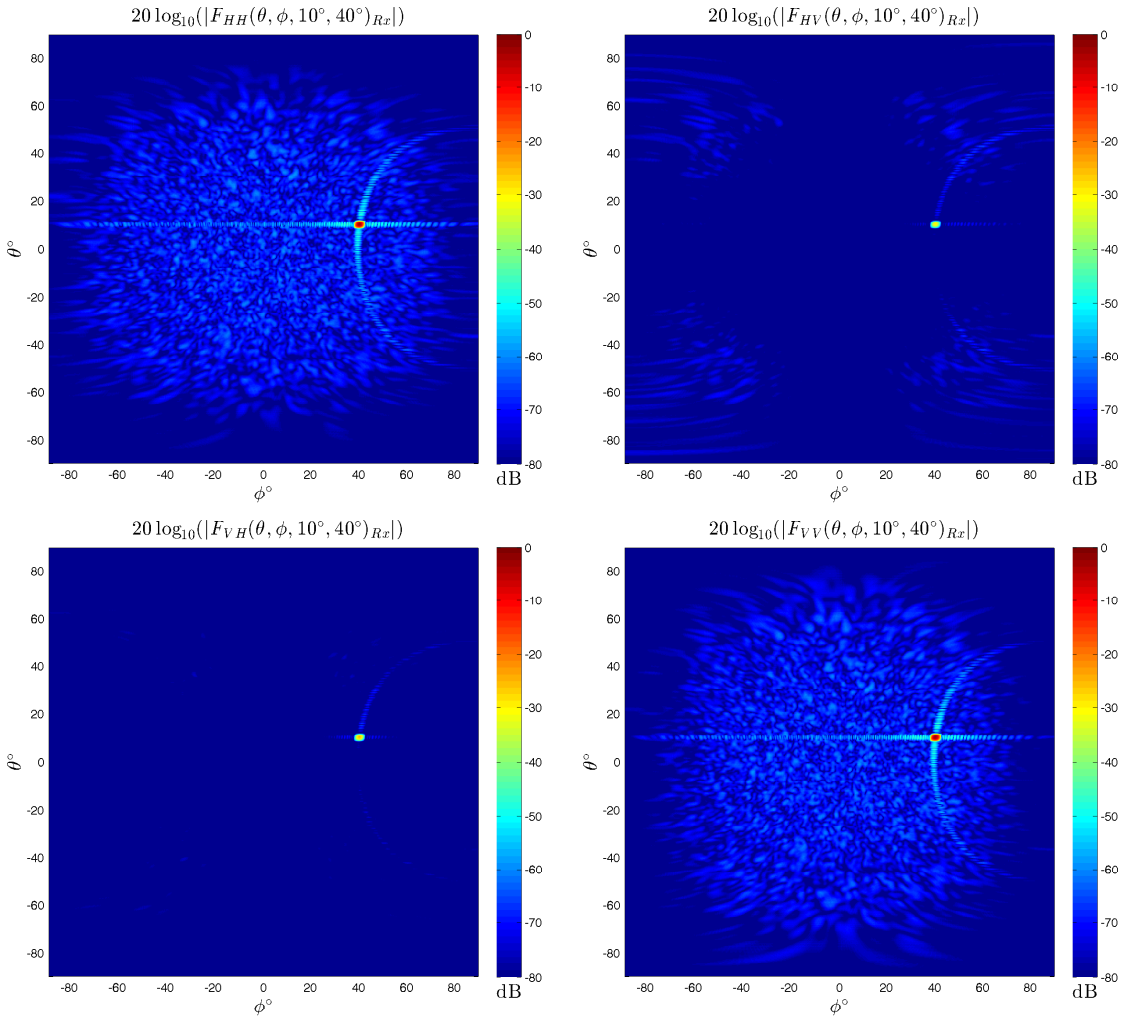

Figure 4.5: Calculated dual-polarization receive patterns for the simulated array. Note the increased mainlobe width and decreased sidelobe levels due to the -47dB Taylor weighting.

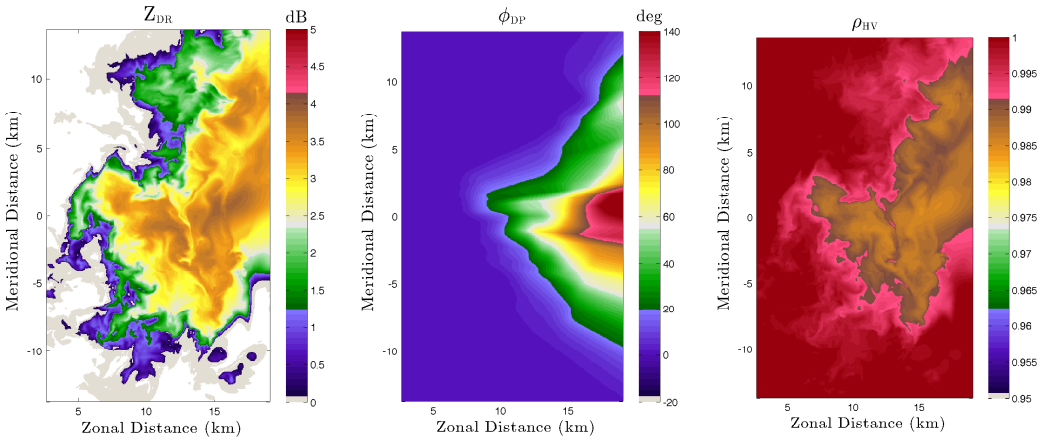

Figure 4.6: Single elevation cross-sections of the polarimetric radar observable values calculated from the ARPS data used in the simulation.

nulled. This results in an ideal radar system free from any cross-polar biases. The results of this simulation are shown in Figure 4.7.

The second simulation is carried out with no mechanical tilt on the array face, but with the cross-polar effects of the antenna pattern included in the simulation. The processed results of this simulation are shown in Figure 4.8. There are significant cross-polar biases induced in this simulation, manifesting themselves primarily in the Z_{DR} measurements. The effects are subtle, but discernible through a direct visual comparison between the Z_{DR} PPIs produced by this scan and the reference scan. However, to show them more clearly, a field PPI of Z_{DR} error (calculated simply by subtracting the Z_{DR}measured by the reference scan from that measured by this scan) is plotted in Figure 4.10a. Here, the biases are extremely clear, increasing in magnitude as the radar steers away from the principal planes in azimuth.

The third simulation scans the same volume, but with a mechanical tilt of 10 degrees on the array face. This introduces significant additional bias due to the effects

of mechanical tilt. The effects of electronic beamsteering are similar to those induced in the previous simulation, as the radar is scanning off of the principle elevation plane by the same angle (although in the opposite direction). The results of this simulation are shown in Figure 4.9. Here, the biases are extremely severe and are evident through visual inspection alone. To allow for an easier inspection of their magnitudes and spatial dependencies, a PPI of Z_{DR} error is also plotted in Figure 4.10b. Once again, the biases increase in magnitude (albeit much more sharply) when steering further away from the principal planes of the array.

Table 4.1: Simulator Demonstration Configuration

Element Configuration	128 x 128
Element Spacing	0.49 λ
Receive Taper	-47 dB Taylor
6 dB Two-Way Beamwidth	1° x 1°
Phase Error	SD=2°
Amplitude Error	SD=0.1dB
Operating Frequency	2.85 GHz
Pulse Repetition Time	1 ms
Pulse Width	1 μs
Frequency Modulation	None
Pulse Window	None
Range Resolution	150 m
Mean SNR	60 dB
Transmit Polarization	Linear

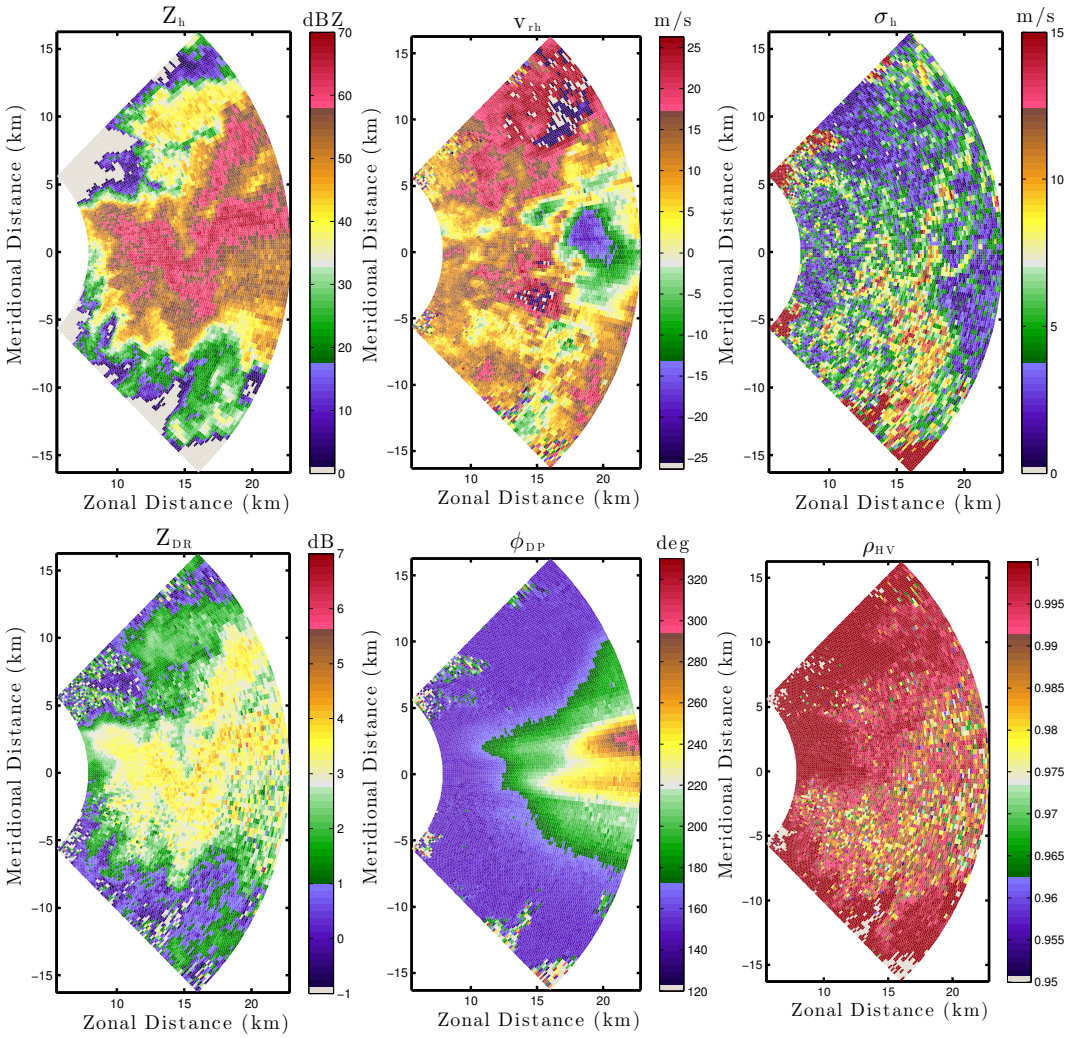

Figure 4.7: Simulated PPIs for an idealized radar system with no cross-polar fields. Measured quantities include H reflectivity (Z_{h}), H radial velocity (v_{rh}), H spectrum width (σ_{h}), differential reflectivity (Z_{DR}), differential phase (ϕ_{DP}), and copolar correlation coefficient (ρ_{HV}).

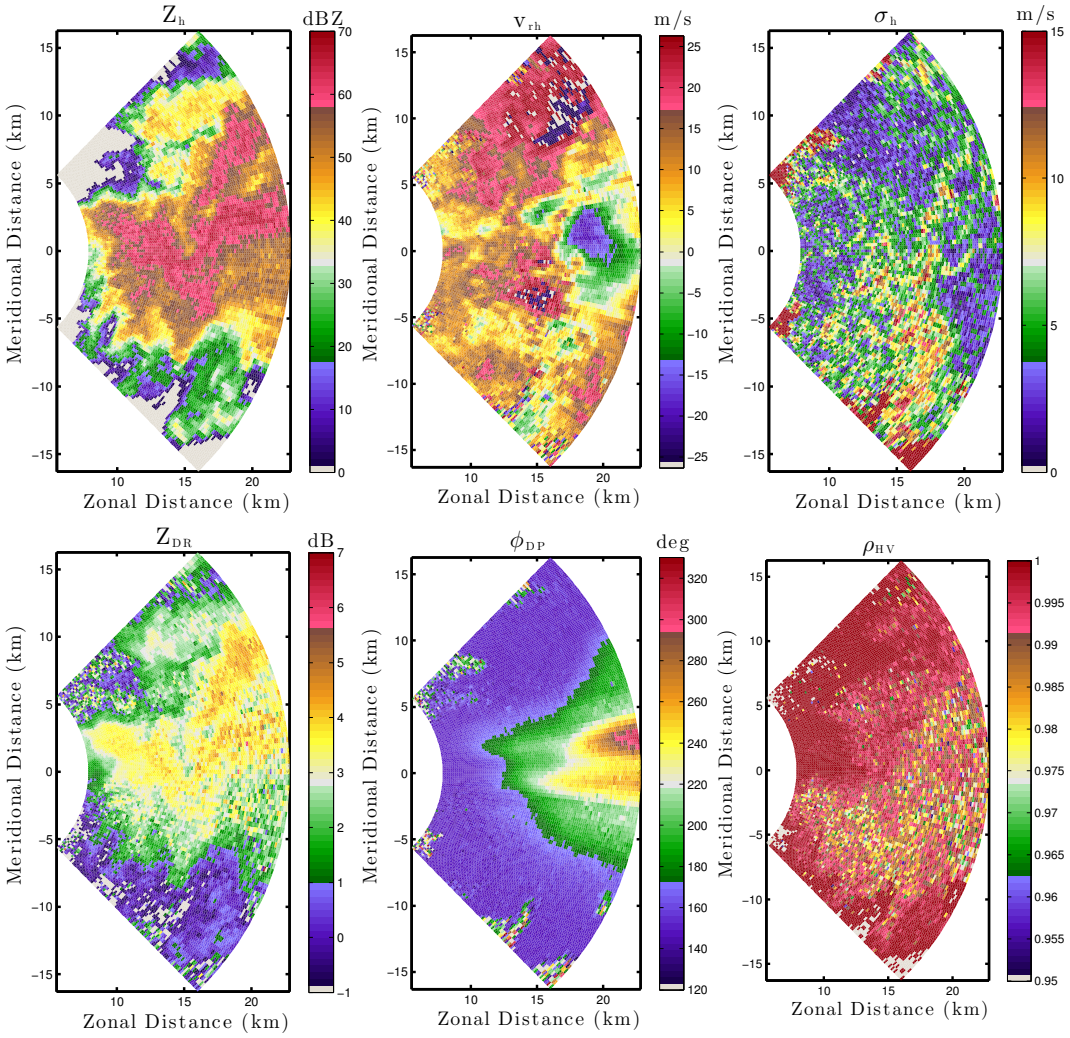

Figure 4.8: Simulated PPIs (depicting exactly the same volume of weather used to generate the results in Figure 4.7) for a radar system with simulated cross-polar fields and no mechanical tilt on the array face. Measured quantities include H reflectivity (Z_{h}), H radial velocity (v_{rh}), H spectrum width (σ_{h}), differential reflectivity (Z_{DR}), differential phase (ϕ_{DP}), and copolar correlation coefficient (ρ_{HV}). Note the subtle errors induced in the Z_{DR} measurements.

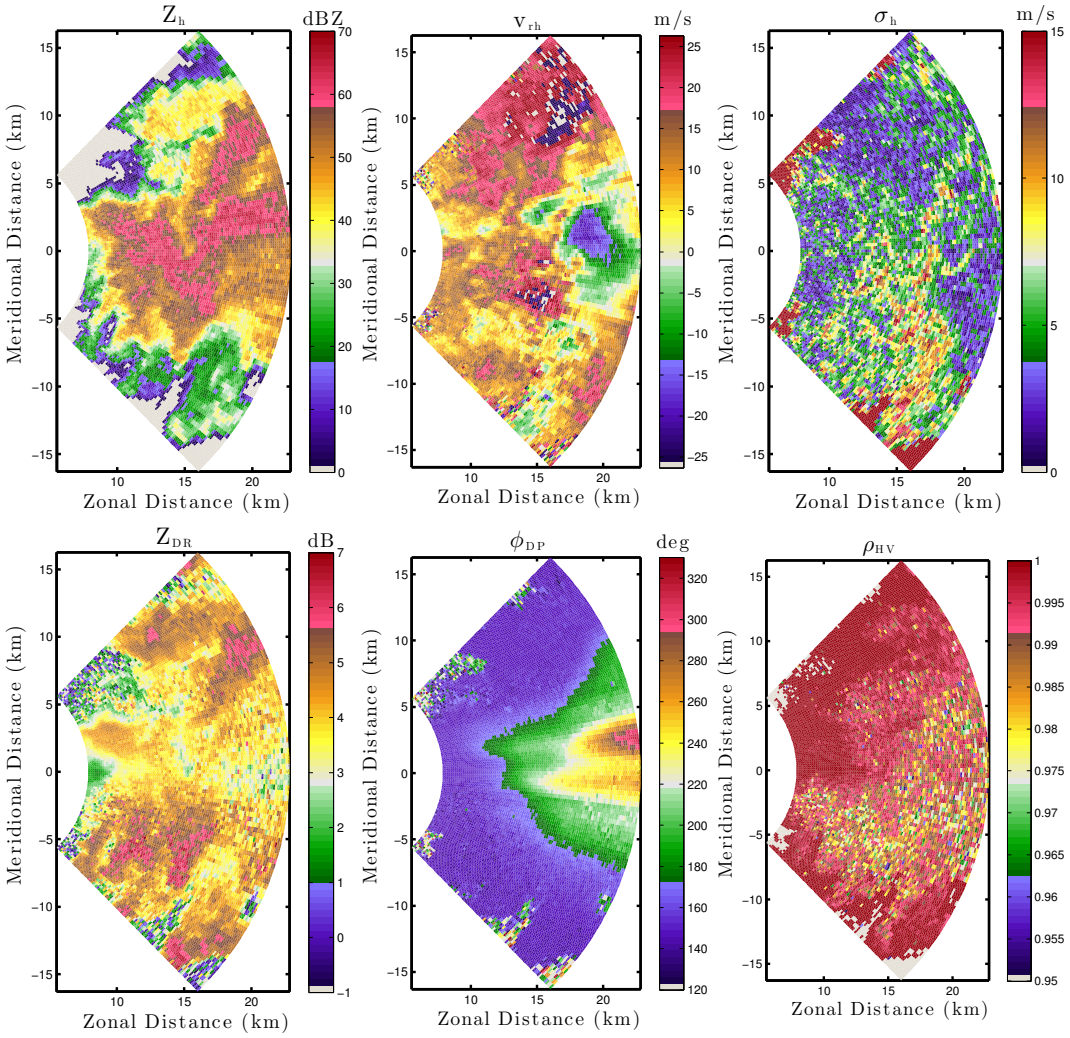

Figure 4.9: Simulated PPIs (depicting exactly the same volume of weather used to generate the results in Figures 4.7-4.8) for a radar system with simulated cross-polar fields and a 10-degree mechanical tilt on the array face. Measured quantities include H reflectivity (Z_{h}), H radial velocity (v_{rh}), H spectrum width (σ_{h}), differential reflectivity (Z_{DR}), differential phase (ϕ_{DP}), and copolar correlation coefficient (ρ_{HV}). Note the severe distortion of the Z_{DR} image.

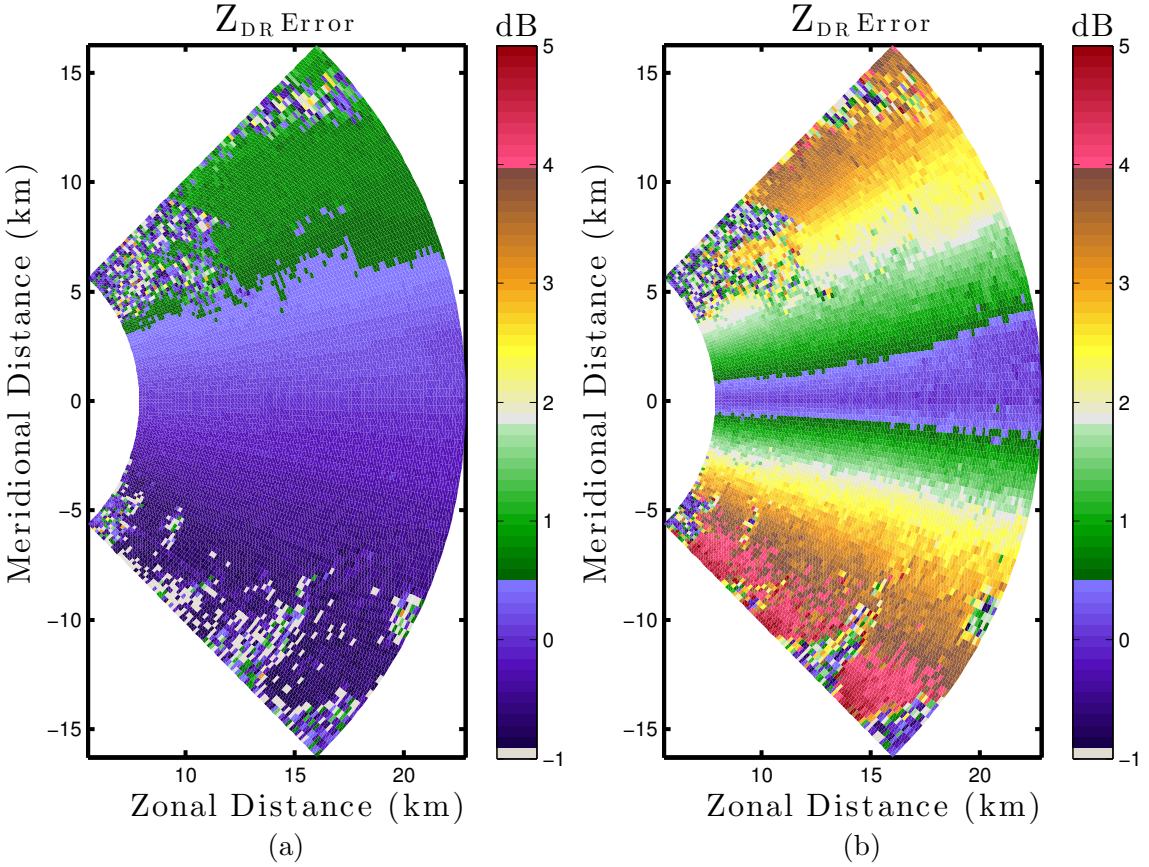

Figure 4.10: Errors in differential reflectivity measurements with respect to the idealized radar with no cross-polar fields, for an array with (a) 0° and (b) 10° of mechanical elevation tilt.

Chapter 5

Quantitative Comparison of Cross Coupling Bias Mitigation Techniques

The objective of this chapter is to utilize the simulation framework described in Chapter 4 to carry out some brief investigations into the effectiveness of polarimetry bias mitigation methods. Specifically, simulations will be carried out in order to compare several aspects of the Z_{DR} bias mitigation performance of the PCSHV and correction matrix methods. These investigations are designed to exercise the capabilities of the simulator for studying mitigation methods while providing some insight into some little-discussed aspects of their performance. They are not designed to be exhaustive in scope with regard to the estimated products, the radar system configuration, or the environmental conditions. While such an analysis would be both interesting and useful, the prospect is complicated by the sheer number of variables (both in terms of the observed weather and the radar system configuration) involved in modeling polarimetric bias. The time and resources required to conduct such a study render it beyond the scope of this work. Therefore, the studies conducted here will be confined exclusively to a comparison of the PCSHV and correction matrix methods, and they will be similarly limited to comparisons of the performance of those methods in estimating Z_{DR} (rather than the full set of polarimetric variables).

5.1 Mechanical Tilt Effects on PCSHV and Correction Matrices

This study seeks to compare the performance of the PCSHV and correction matrix (CM) with respect to mechanical tilt applied to the face of the array. Two tilt angles (0° and 10°) were studied. The 10° tilt was chosen as a typical fixed mechanical tilt for the face of an operational phased array. For example, this is the tilt on the face of the NWRT (Doviak et al. 2011). For each combination of mechanical tilt and bias correction method, a simulation was carried out over the complete range of possible ϕ_{DP0} values (the initial differential phase at the edge of the simulation volume nearest the radar). The simulated ϕ_{DP0} values were varied from $0 - 360°$ in 30° increments, leading to a set of 12 simulations for each configuration. It is necessary to vary this value across all possible angles in order to completely characterize the effectiveness of each method due to the sensitivity of cross-polar bias magnitudes to ϕ_{DP}. In addition to the bias mitigation methods under test, several other scenarios were simulated. In order to quantify the effectiveness of the mitigation methods, it is also necessary to generate a set of ground truth values. This was accomplished by carrying out a reference simulation at each mechanical tilt angle that used the same system parameters as the bias mitigation tests, but with completely nulled cross-polar fields (both due to tilt and element radiation patterns). This isolates the differences between the reference and test simulations to effects of cross-polar bias. Finally, uncorrected SHV simulations were also carried out across the full range of ϕ_{DP0} values to serve as a control group. The complete list of simulations is enumerated in Table

5.1. The radar system configuration used is identical to that used for the simulations

Table 5.1: Mechanical Tilt Test Simulations

Configuration	Mechanical Tilt	Bias Mitigation
1	0°	PCSHV
2	10°	PCSHV
3	0°	CM
4	10°	CM
Control 1	0°	SHV
Control 2	10°	SHV
Reference 1	0°	No X-pol
Reference 2	10°	No X-pol

carried out in Chapter 4, with the exception that no taper was applied to the array on receive. Element patterns are shown in Figure 3.7, sample array radiation patterns are depicted by Figure 4.4. These array radiation patterns are for both transmit and receive, due to the lack of a receive taper. Other system parameters are listed in Table 4.1. The correction matrices used for this experiment are calculated from the actual radiation patterns (i.e., there is no simulated measurement error), and they account for cross-polar biases due both to the element patterns and the mechanical tilt. In other words we can represent the range-normalized received voltage in CM mode as:

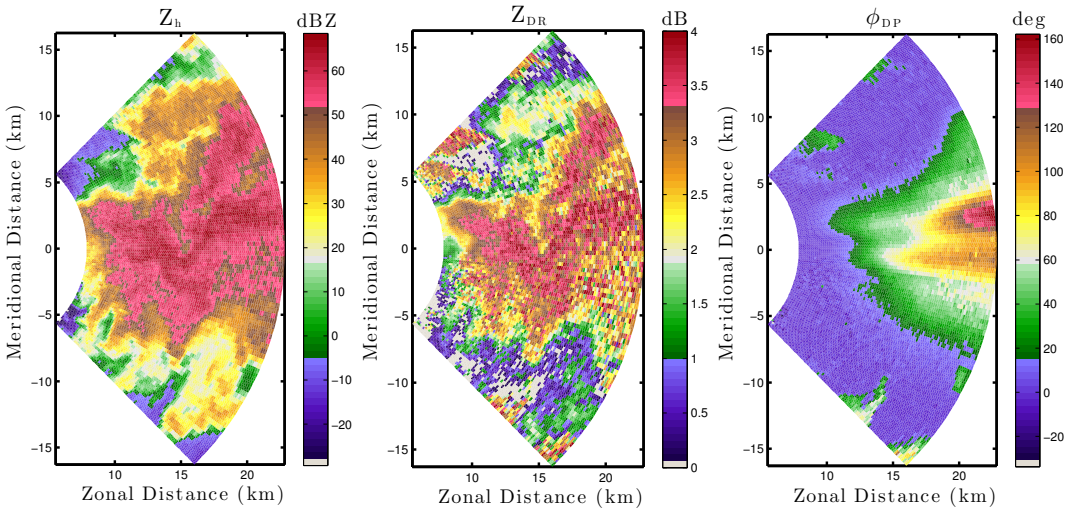

Figure 5.1: Selected polarimetric products calculated from the reference scan (i.e. no cross-polarization) at 0° mechanical elevation tilt. The volume is located at an elevation angle of 5°.

$$\mathbf{V_{Rx}} = \mathbf{C_{Rx}F^{T}P^{T}SPFC_{Tx}V_{Tx}}, \tag{5.1}$$

$$\mathbf{C_{Tx}} = \mathbf{F^{-1}P^{T}}, \tag{5.2}$$

$$\mathbf{C_{Rx}} = \mathbf{P(F^{T})^{-1}}. \tag{5.3}$$

Note that in the case where the transmit and receive radiation patterns are equal (as they are here) $\mathbf{F_{Rx}} = \mathbf{F_{Tx}^{T}}$, hence the subscripts can be dispensed with entirely, as in the above expressions. The simulated region of weather is depicted by selected PPIs of polarimetric products from the 0° mechanical tilt reference scan in Figure 5.1. The scan volume was strategically located at an elevation angle of 5°. This means to scan this volume the 10° mechanical elevation configurations must scan downward electronically by 5° and the 0° mechanical elevation configurations must scan upward

by the same amount. This takes advantage of the symmetry of the simulated element patterns to allow a reasonable direct comparison between the simulated errors at the 0° and 10° mechanical elevation. In summary, 12 simulations were carried out for each configuration listed in Table 5.1. Each of the twelve simulations observed an identical simulated weather scenario, with the only difference being that ϕ_{DP0} was varied from 0-330° in 30° increments over the twelve simulations. The results of this experiment are shown in Figure 5.2. For each simulation carried out, the mean Z_{DR} error at each azimuth was calculated by averaging the absolute value of the difference between the measured Z_{DR}value and that obtained from the reference scan over the range gates in each radial. Gates with an SNR of less than 30 dB were excluded from this average.

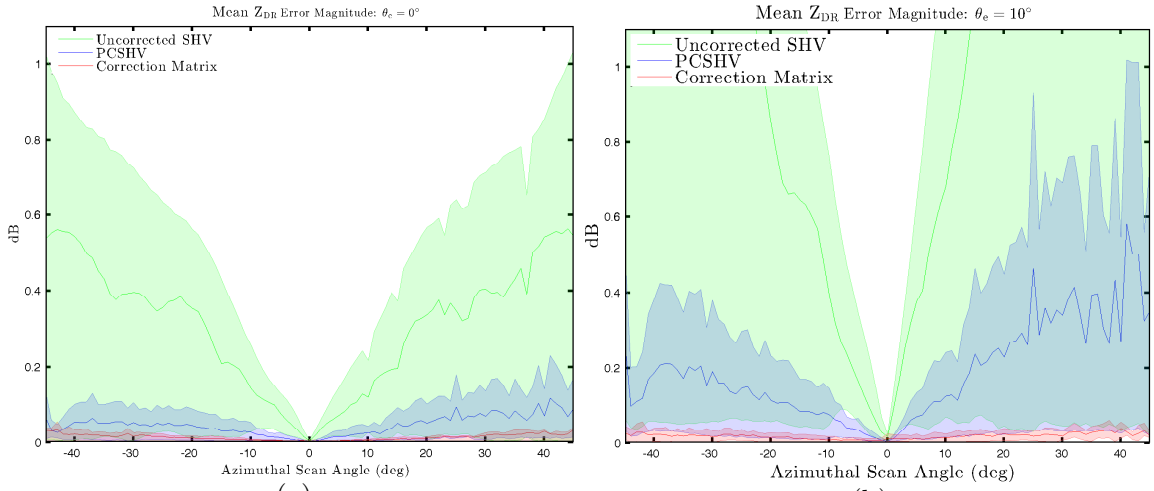

Figure 5.2: For both the 0° mechanical tilt (a) and 10° mechanical tilt (b) simulations, the average Z_{DR} error magnitude for range gates with an SNR greater than 30 dB was calculated along each azimuthal radial. The range of mean error magnitudes over all ϕ_{DP0} values is represented by the shaded regions. The lines represent the median mean error magnitude along each radial.

This yields a set of average Z_{DR} errors at each azimuth for each ϕ_{DP0} value. The line corresponding to each correction method in the figure represents the average of these azimuthal averages over all ϕ_{DP0} values. The upper and lower bounds of the corresponding shaded region indicate the maximum and minimum azimuthal average over the full range of simulated ϕ_{DP0} values. It is clear that at both mechanical tilt angles, both the correlation matrix and phase coding methods represent substantial improvements over the uncorrected SHV data. However, there are some major notable differences in their performance characteristics. First, the correction matrix method results in a smaller bias over the majority of the scan volume. Second, the residual errors from the PCSHV method exhibit a much stronger dependence on steering angle than those from the correction matrix method. Finally, the residual errors from the PCSHV method also exhibit a much stronger dependence on ϕ_{DP}, which manifests itself in the figure as an increased width of the shaded region corresponding to the PCSHV errors.

While a detailed mathematical analysis of the deterioration of PCSHV performance with mechanical tilt is beyond the scope of this work, it is useful to examine our model of the received signals in order to gain a general understanding of the origins of this effect. We begin with the polarimetric matrix model used in the simulator, which incorporates the mechanical tilt of the array in the form of projection matrices (Equation 5.1). Integrating that expression over a solid angle Ω to model an observation of a volume of scatterers we obtain:

$$\mathbf{V_{Rx}} = \int_{\Omega} \mathbf{F^T P^T S' P F V_{Tx}} d\Omega. \tag{5.4}$$

If the H and V signals represented by $\mathbf{V_{Tx}}$ are phase coded using the scheme described by Equations 3.43 and 3.44 and the matrix multiplications are carried out accordingly, we arrive at the following expressions for the received H and V polarized signals IQ signals:

$$V_{\mathrm{h}}^{\mathrm{Rx}}(n) \sim \int_{\Omega} \Bigg(\Big[(F_{\mathrm{hh}}^2 s_{\mathrm{hh}} + F_{\mathrm{vh}}^2 s_{\mathrm{vv}}) \cos^2\gamma + 2F_{\mathrm{hh}}F_{\mathrm{vh}}(s_{\mathrm{hh}} - s_{\mathrm{vv}}) \cos\gamma \sin\gamma + (F_{\mathrm{hh}}^2 s_{\mathrm{vv}} + F_{\mathrm{vh}}^2 s_{\mathrm{hh}}) \sin^2\gamma \Big] + \Big[(F_{\mathrm{hh}}F_{\mathrm{hv}} s_{\mathrm{hh}} + F_{\mathrm{vv}}F_{\mathrm{vh}} s_{\mathrm{vv}}) \cos^2\gamma + 2(F_{\mathrm{hh}}F_{\mathrm{vv}} + F_{\mathrm{hv}}F_{\mathrm{vh}})(s_{\mathrm{hh}} - s_{\mathrm{vv}}) \cos\gamma \sin\gamma + (F_{\mathrm{hh}}F_{\mathrm{hv}} s_{\mathrm{vv}} + F_{\mathrm{vv}}F_{\mathrm{vh}} s_{\mathrm{hh}}) \sin^2\gamma \Big] e^{j\beta} c(n) \Bigg) e^{j\psi_{\mathrm{h}}(\theta,\phi)} d\Omega, \quad (5.5)$$

$$V_{\mathrm{v}}^{\mathrm{Rx}}(n) \sim \int_{\Omega} \Bigg(\Big[(F_{\mathrm{vv}}^2 s_{\mathrm{vv}} + F_{\mathrm{hv}}^2 s_{\mathrm{hh}}) \cos^2\gamma + 2F_{\mathrm{vv}}F_{\mathrm{hv}}(s_{\mathrm{vv}} - s_{\mathrm{hh}}) \cos\gamma \sin\gamma + (F_{\mathrm{vv}}^2 s_{\mathrm{hh}} + F_{\mathrm{hv}}^2 s_{\mathrm{vv}}) \sin^2\gamma \Big] e^{j\beta} c(n) + \Big[(F_{\mathrm{vv}}F_{\mathrm{vh}} s_{\mathrm{vv}} + F_{\mathrm{hh}}F_{\mathrm{hv}} s_{\mathrm{hh}}) \cos^2\gamma + 2(F_{\mathrm{vv}}F_{\mathrm{hh}} + F_{\mathrm{vh}}F_{\mathrm{hv}})(s_{\mathrm{vv}} - s_{\mathrm{hh}}) \cos\gamma \sin\gamma + (F_{\mathrm{vv}}F_{\mathrm{hv}} s_{\mathrm{hh}} + F_{\mathrm{hh}}F_{\mathrm{hv}} s_{\mathrm{vv}}) \sin^2\gamma \Big] \Bigg) e^{j\psi_{\mathrm{v}}(\theta,\phi)} d\Omega. \quad (5.6)$$

It is immediately evident through comparison with the analogous expressions for an untilted array (Equations 3.45 and 3.46) that the mechanical tilt has introduced serious complications. Consider the first bracketed set of terms in Equation 5.5:

$$\Big[(F_{\mathrm{hh}}^2 s_{\mathrm{hh}} + F_{\mathrm{vh}}^2 s_{\mathrm{vv}}) \cos^2\gamma + 2F_{\mathrm{hh}}F_{\mathrm{vh}}(s_{\mathrm{hh}} - s_{\mathrm{vv}}) \cos\gamma \sin\gamma + (F_{\mathrm{hh}}^2 s_{\mathrm{vv}} + F_{\mathrm{vh}}^2 s_{\mathrm{hh}}) \sin^2\gamma \Big]. \quad (5.7)$$

Here, the uncontaminated copolar signal contribution is $F_{\rm hh}^2 s_{\rm hh} \cos^2\gamma$, while all other terms represent an undesired contaminating contribution. The contaminating contributions in this set of terms will occur even in AHV transmission mode, and they cannot be eliminated by phase coding because the bracketed terms do not carry the sign of the phase code. The magnitude of these contaminating terms will be significantly greater than that of the corresponding contaminating term for the untilted array, which is merely $F_{\rm vh}^2 s_{\rm vv}$. Consider next the second bracketed set of terms:

$$\Big[(F_{\rm hh}F_{\rm hv}s_{\rm hh} + F_{\rm vv}F_{\rm vh}s_{\rm vv})\cos^2\gamma + 2(F_{\rm hh}F_{\rm vv} + F_{\rm hv}F_{\rm vh})(s_{\rm hh} - s_{\rm vv})\cos\gamma\sin\gamma + (F_{\rm hh}F_{\rm hv}s_{\rm vv} + F_{\rm vv}F_{\rm vh}s_{\rm hh})\sin^2\gamma\Big]e^{j\beta}c(n). \quad (5.8)$$

Here we have a number of highly damaging bias terms. They are so damaging because the expected value of the magnitude squared of (5.5) (required to compute $Z_{\rm DR}$) contains a pair of cross-products between (5.7) and (5.8). These cross-products, however, carry the alternating sign of the phase code and will therefore vanish when the number of power samples is even (Zrnić et al. 2014). Still, the terms in (5.8) contribute to bias, as the expected value of the magnitude squared of (5.5) also contains a term consisting of the expected value of the magnitude squared of (5.8). It is clear from inspection that the magnitude of this bias will also be significantly greater than the corresponding contribution for untilted arrays, where the contaminating terms are simply $(F_{\rm hh}F_{\rm hv}s_{\rm hh} + F_{\rm vv}F_{\rm vh}s_{\rm vv})$.

While PCSHV was clearly outperformed by the CM method in this experiment, there is a major qualifier to that conclusion. The correction matrices utilized in this

experiment were an ideal implementation in the sense that they utilized perfect knowledge of the radiation patterns. The only source of error for the correction matrices in this simulation was the fact that the cross-polarized fields are only perfectly corrected at the exact peak of the transmitted beam. Therefore, scatterers illuminated by the rest of the mainlobe and the sidelobes will be imperfectly corrected, moreso farther from the mainlobe peak. However, this is not a realistic scenario. Radiation patterns of antennas cannot be perfectly measured, nor are they perfectly static over the duration of the operation of a radar. This leads to the second set of experiments contained in this chapter, an investigation of the resilience of the CM method to errors in the measured patterns used to calculate the correction matrices.

5.2 Correction Matrix Resilience to Antenna Pattern Measurement Error

In this study, a number of simulations were carried out with a radar system configuration identical to that utilized Section 5.1, with the exception that a taper was added to the array on receive as specified in Table 4.1. The resulting receive patterns for the array are shown in Figure 4.5. A set of four scenarios, listed in Table 5.2 were simulated. The overall best and worst case ϕ_{DP0} values (0° and 180°) were estimated from the data obtained in the previous experiment by averaging the Z_{DR} error magnitude over the entire simulated PPI at each value of ϕ_{DP0}. The four configurations used in this experiment consist of each possible combination of these ϕ_{DP0} values with mechanical elevation tilts of 0° and 10°. For each of these configurations a ran-

Table 5.2: Correction Matrix Error Simulations

Configuration	Mechanical Tilt	ϕ_{DP}
1	0°	0°
2	10°	0°
3	0°	180°
4	10°	180°

dom measurement error ϵ_n was added to each antenna pattern value used to calculate the correction matrices. Thus, we can express the correction matrices utilized in the simulation as follows:

$$\mathbf{C'_{Tx}} = (\mathbf{F_{Tx}} + \mathbf{E_{Tx}})^{-1}\mathbf{P^T}, \tag{5.9}$$

$$\mathbf{C'_{Rx}} = \mathbf{P}(\mathbf{F_{Rx}} + \mathbf{E_{Rx}})^{-1}, \tag{5.10}$$

$$\mathbf{E_{Tx}} = \begin{bmatrix} \epsilon_1 & \epsilon_3 \\ \epsilon_2 & \epsilon_4 \end{bmatrix}, \tag{5.11}$$

$$\mathbf{E_{Rx}} = \begin{bmatrix} \epsilon_5 & \epsilon_7 \\ \epsilon_6 & \epsilon_8 \end{bmatrix}. \tag{5.12}$$

ϵ_n represents the nth realization of the random variable ϵ, which is a zero-mean, circularly symmetric, complex Gaussian random variable with a variance specified as some percentage of the copolar H radiation pattern power (this variance will be referred to interchangeably as the average error power). For each configuration, simulations were carried out for error powers ranging from 0-2% of the copolar pattern power. Pang et al. (2016) gives an error of 5% in amplitude (translating to an 0.25% error in power) as a figure "achievable in antenna engineering". However, to allow

for the possibility of less than ideal measurement conditions, as well as consideration of what errors might occur due to drift over time between measurements of a theoretical system, it is useful to observe error levels above and beyond that. The 0-2% power error range evaluated here corresponds to a 0-14% amplitude error range. The mean Z_{DR} error magnitude over the PPI is plotted against average error power for each scenario in Figure 5.3. The mean error magnitude for each error power level was obtained by averaging the Z_{DR} error magnitude over all resolution volumes with an SNR of more than 30 dB. Figure 5.4 shows a set of box plots for each scenario representing the distribution of average Z_{DR} errors over azimuth angle for selected

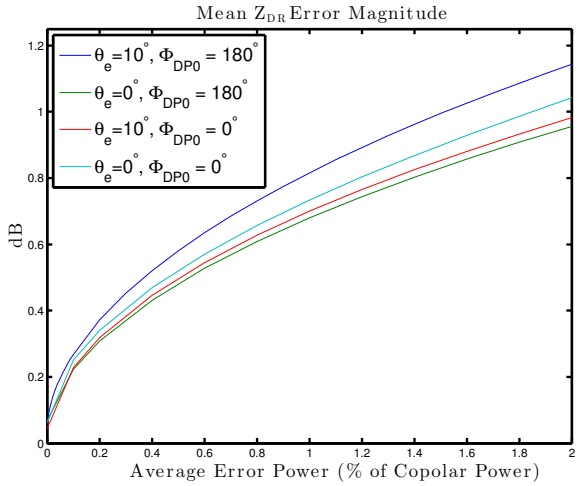

Figure 5.3: Mean Z_{DR} measurement errors over a range of average error powers. The mean Z_{DR} error at each simulated measurement error power represesnts an average over the entire PPI. In addition to showing the relationship between the pattern measurement errors and resulting Z_{DR} errors, this figure also shows the degree of retained dependence on mechanical tilt and differential phase, as well as the manner in which that dependence scales with error magnitude.

average error powers. The set of data points used to produce each box plot is the set of mean Z_{DR} error magnitudes at each azimuth (corresponding to each independent realization of the random error). The gates used to obtain these averages were again thresholded at 30 dB SNR.

We will conclude this study with an examination of a simplified model for the received signal in order to gain some insight into the path by which the correction matrix propagates to the received signal. First, we will write an expression for the signal, normalized for range effects, received when observing a point target at beam peak.

$$\mathbf{V_{Rx}} = \mathbf{C'_{Rx}F_{Rx}P^{T}S'PF_{Tx}C'_{Tx}V_{Tx}} \tag{5.13}$$

Next, the correction matrices with errors included are rewritten in terms of the ideal correction matrices. For C'_{Tx} we have:

$$\mathbf{C'_{Tx}} = \mathbf{P}(\mathbf{F_{Tx}} + \mathbf{E_{Tx}})^{-1} \tag{5.14}$$

$$= \mathbf{P}\begin{bmatrix} F_{\mathrm{hh}}^{\mathrm{Tx}} + \epsilon_1 & F_{\mathrm{hv}}^{\mathrm{Tx}} + \epsilon_2 \\ F_{\mathrm{vh}}^{\mathrm{Tx}} + \epsilon_3 & F_{\mathrm{vv}}^{\mathrm{Tx}} + \epsilon_4 \end{bmatrix}^{-1} \tag{5.15}$$

$$= \frac{1}{\det(\mathbf{F_{Tx}} + \mathbf{E_{Tx}})}\mathbf{P}\begin{bmatrix} F_{\mathrm{vv}}^{\mathrm{Tx}} + \epsilon_4 & -(F_{\mathrm{hv}}^{\mathrm{Tx}} + \epsilon_2) \\ -(F_{\mathrm{vh}}^{\mathrm{Tx}} + \epsilon_3) & F_{\mathrm{hh}}^{\mathrm{Tx}} + \epsilon_1 \end{bmatrix} \tag{5.16}$$

$$= \frac{1}{\det(\mathbf{F_{Tx}} + \mathbf{E_{Tx}})}P(\det(\mathbf{F_{Tx}})\mathbf{F_{Tx}^{-1}} + \mathbf{E'_{Tx}}) \tag{5.17}$$

$$= \frac{\det(\mathbf{F_{Tx}})}{\det(\mathbf{F_{Tx}} + \mathbf{E_{Tx}})}\left(\mathbf{C_{Tx}} + \frac{\mathbf{E'_{Tx}}}{\det(\mathbf{F_{Tx}})}\right) \tag{5.18}$$

It should be noted that since every element ϵ_n of the $\mathbf{E_{Tx}}$ and $\mathbf{E_{Rx}}$ matrices represents an independent realization of the random variable ϵ, which is symmetrically distributed about zero, each of the elements of $\mathbf{E'_{Rx}}$ and $\mathbf{E'_{Tx}}$ has the same PDF as

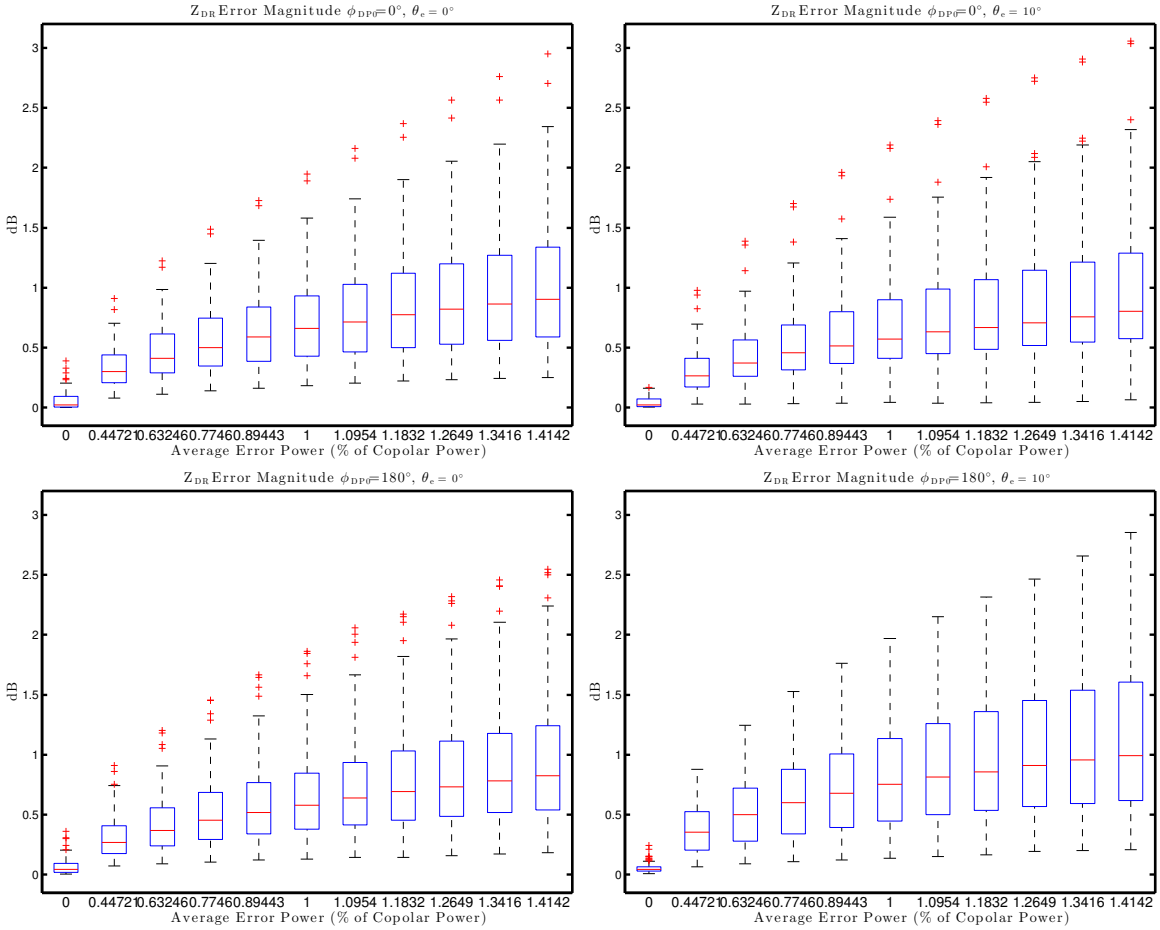

Figure 5.4: Box plots illustrating the distribution of average Z_{DR} error magnitude over azimuth (determined in a manner identical to that used to produce Figure 5.2) at selected values of average error power. The red line corresponds to the median, and the blue box delineates the interquartile range (IQR). The whiskers extend to the minimum and maximum within 1.5 IQR of the lower and upper quartiles respectively, and the red crosses denote data points outside of that range.

the corresponding element of the original error matrix. Thus we will replace the modified matrices with the original matrices. Then, supposing that the copolar radiation pattern magnitudes are much greater than both the cross-polar pattern and error magnitudes we obtain:

$$\det(\mathbf{F_{Tx}}) \approx \det(\mathbf{F_{Tx}} + \mathbf{E_{Tx}}) \approx 1 \tag{5.19}$$

$$\mathbf{C'_{Tx}} \approx \mathbf{C_{Tx}} + \mathbf{E_{Tx}} \tag{5.20}$$

An identical procedure can be used to rewrite the correction matrix on receive, yielding:

$$\mathbf{C'_{Rx}} \approx \mathbf{C_{Rx}} + \mathbf{E_{Tx}} \tag{5.21}$$

These expressions can then be substituted back into Equation 5.13:

$$\mathbf{V_{Rx}} = (\mathbf{C_{Rx}} + \mathbf{E_{Rx}})\mathbf{F^T P^T S' P F}(\mathbf{C_{Tx}} + \mathbf{E_{Tx}})\mathbf{V_{Tx}} \tag{5.22}$$

$$= (\mathbf{C_{Rx}} + \mathbf{E_{Rx}})(\mathbf{F^T P^T S' P F C_{Tx}} + \mathbf{F^T P^T S' P F E_{Tx}})\mathbf{V_{Tx}} \tag{5.23}$$

$$\begin{aligned} = (&\mathbf{C_{Rx}F^T P^T S' P F C_{Tx}} + \mathbf{C_{Rx}F^T P^T S' P F E_{Tx}} + \\ &\mathbf{E_{Rx}F^T P^T S' P F C_{Tx}} + \mathbf{E_{Rx}F^T P^T S' P F E_{Tx}})\mathbf{V_{Tx}} \end{aligned} \tag{5.24}$$

$$= (\mathbf{S'} + \mathbf{S' P F E_{Tx}} + \mathbf{E_{Rx}F^T P^T S'} + \mathbf{E_{Rx}F^T P^T S' P F E_{Tx}})\mathbf{V_{Tx}} \tag{5.25}$$

It is clear from inspection that every element of the 2×2 matrix resulting from carrying out the matrix multiplication $\mathbf{E'_{Rx}F^T P^T S' P F E'_{Tx}}$ will be second order with respect to the random error ϵ, while the other error terms $\mathbf{S' P F E'_{Tx}}$ and $\mathbf{E_{Rx}F^T P^T S'}$ are first order with respect to the error, and will therefore dominate. Thus, the second order error term will be discarded and the received signal can be approximated as:

$$\mathbf{V_{Rx}} \approx (\mathbf{S'} + \mathbf{S' P F_{Tx} E_{Tx}} + \mathbf{E_{Rx} F_{Rx} P^T S'})\mathbf{V_{Tx}} \tag{5.26}$$

Carrying out the matrix multiplications and additions yields the following results for the H and V signals respectively:

$$V_{\mathrm{h}}^{\mathrm{Rx}} \approx s_{\mathrm{hh}} + s_{\mathrm{hh}}\Bigg(\Big[(\epsilon_1+\epsilon_2)F_{\mathrm{hh}}^{\mathrm{Tx}} + \epsilon_5 F_{\mathrm{hh}}^{\mathrm{Rx}} + (\epsilon_3+\epsilon_4)F_{\mathrm{vh}}^{\mathrm{Tx}} + \epsilon_7 F_{\mathrm{hv}}^{\mathrm{Rx}}\Big]\cos\gamma + \Big[(\epsilon_3-\epsilon_4)F_{\mathrm{vv}}^{\mathrm{Tx}} + \epsilon_7 F_{\mathrm{vv}}^{\mathrm{Rx}} - (\epsilon_1+\epsilon_2)F_{\mathrm{hv}}^{\mathrm{Tx}} - \epsilon_5 F_{\mathrm{vh}}^{\mathrm{Rx}}\Big]\sin\gamma\Bigg) + s_{\mathrm{vv}}\Big[(\epsilon_7 F_{\mathrm{vv}}^{\mathrm{Rx}} + \epsilon_5 F_{\mathrm{vh}}^{\mathrm{Rx}})\cos\gamma - (\epsilon_5 F_{\mathrm{hh}}^{\mathrm{Rx}} + \epsilon_7 F_{\mathrm{hv}}^{\mathrm{Rx}})\sin\gamma\Big], \quad (5.27)$$

$$V_{\mathrm{v}}^{\mathrm{Rx}} \approx s_{\mathrm{vv}} + s_{\mathrm{vv}}\Bigg(\Big[(\epsilon_3+\epsilon_4)F_{\mathrm{vv}}^{\mathrm{Tx}} + \epsilon_8 F_{\mathrm{vv}}^{\mathrm{Rx}} + (\epsilon_1+\epsilon_2)F_{\mathrm{hv}}^{\mathrm{Tx}} + \epsilon_6 F_{\mathrm{vh}}^{\mathrm{Rx}}\Big]\cos\gamma + \Big[(\epsilon_1+\epsilon_2)F_{\mathrm{vv}}^{\mathrm{Tx}} - \epsilon_6 F_{\mathrm{vv}}^{\mathrm{Rx}} + (\epsilon_3+\epsilon_4)F_{\mathrm{vh}}^{\mathrm{Tx}} - \epsilon_8 F_{\mathrm{hv}}^{\mathrm{Rx}}\Big]\sin\gamma\Bigg) + s_{\mathrm{hh}}\Big[(\epsilon_6 F_{\mathrm{hh}}^{\mathrm{Rx}} + \epsilon_8 F_{\mathrm{hv}}^{\mathrm{Rx}})\cos\gamma + (\epsilon_8 F_{\mathrm{vv}}^{\mathrm{Rx}} + \epsilon_6 F_{\mathrm{vh}}^{\mathrm{Rx}})\sin\gamma\Big]. \quad (5.28)$$

Note that due to the fact that we are considering the simplified situation of a point target at beam peak, it is not necessary to integrate this result over a solid angle. Examining these expressions we see that the uncontaminated copolar signal is represented by the leading s_{hh} or s_{vv}. The other terms are all bias contributors. The Z_{DR} bias, as always, is dependent on the expected value of the magnitude squared of the received signals. Here, as before, the error in the expected squared magnitude will be dominated by the terms that represent the product between a bias term and the uncontaminated signal. These will be first order with respect to ϵ, while products of two bias terms will be second order with respect to ϵ. It should be noted that while the expected magnitude of the dominant power bias will be first order with respect to ϵ, the expected initial error in radiation pattern power measurement is second order with respect to ϵ. This nonlinear propagation of the measurement error to the received signal is responsible for the high level of sensitivity to error observed in the

simulations. The exact extent of this error propagation effect is subject to details of the steering angle, radiation pattern characteristics, mechanical tilt, and scatterer characteristics. Even then, a complete analytical characterization of this effect would have to account for the increased errors occuring in contributions from targets away from the beam peak. Such a study is beyond the scope of what is presented in this thesis.

Results such as those obtained here can be used to provide some practical insight into what kinds of accuracy requirements might need to be met to meet a particular design goal. For example the MPAR notional functional requirements require Z_{DR} biases not to exceed 0.1 dB. Pang et al. (2016) suggests that this goal may be achieved by maintaining error amplitudes below 1% of the copolar amplitude, which translates to 0.01% of the copolar power. However, achieving that number makes some very optimistic assumptions about operating conditions, notably a perfectly homogenous 0 dB Z_{DR} field of observed scatterers. Here we can see, that in realistic weather conditions, this specification is not even met under ideal correction. Under those conditions, the upper boundary of the IQR remains below 0.1 dB, but the maximum (neglecting outliers) extends as far as 0.2 dB. Meanwhile, the bias levels at the "achievable" error level of 0.25% of the copolar power are well outside of the specification, with mean error levels across the entire PPI of approximately 0.34 dB for the best case simulated scenario. These findings may suggest some sort of hybrid approach combining correction matrices and PCSHV, which may help mitigate first order biases contributed from regions away from the beam peak. Alternatively, they

may necessitate the use of another technique altogether, or some reconsideration of the realism of the technical requirements.

5.3 Conclusions

The studies in this chapter demonstrated several advantages and drawbacks of both the CM and PCSHV methods that have received little attention in the existing literature. It was shown that phase coding can allow problematic levels of residual error given a typical operational level of mechanical tilt on the face of the PPAR. While the effects of mechanical tilt (Orzel 2015) and second order residual bias in the PCSHV scheme (Ivić and Doviak 2016) have been discussed, their interaction has not been explored in depth. Although correction matrices performed better with respect to the application of mechanical tilt, the need for highly precise radiation pattern measurements in any successful implementation of this method was clearly illustrated by the simulation results, and it represents a serious technical challenge. While the effects of measurement error on the correction matrix method have been previously discussed in the literature (Fulton and Chappell 2010; Pang et al. 2016), a study of the effects has not been carried out in the context of realistic weather simulations. In addition to providing some insight into interesting aspects of these techniques, this chapter also showcased the utility of the simulator in modeling and evaluating bias mitigation methods.

Finally, it is important to be clear that these studies do not represent an exhaustive study of these methods. Only a single weather scenario was studied, and the

experiments were limited to very specific aspects of the performance of these bias mitigation methods. Perhaps most obviously, the study was limited to effects only on Z_{DR}. These methods can, however, have effects on other polarimetric variables. Notably, PCSHV is known to exhibit a detrimental effect on $|\rho_{\mathrm{HV}}(0)|$ estimates (Ivić and Zrnić 2013). Similarly, the mathematical analysis provided is highly simplified and qualitative, intended primarily to give a general sense of the origins of the results produced by the simulator. An exhaustive study of these mitigation methods, either through simulation or analytical mathematics, is beyond the scope of this work.

Chapter 6

Conclusions and Recommendations for Future Work

6.1 Conclusions

The primary objective of this thesis was to present a method for the simulation of polarimetric phased array weather radars that combines a highly flexible radar system model with realistic weather simulations. The simulator presented combines the Lagrangian scattering center framework demonstrated by Cheong et al. (2008b) with realistic antenna patterns, as well as the method of time series generation developed by Zrnić (1975) and extended by Galati and Pavan (1995) in order to produce time series which account for the existence of cross-polar fields. ARPS data is used to generate fields of simulated weather such that the performance of the simulated radar systems may be characterized in realistic operational scenarios. The radar system model includes easily configurable polar element patterns, array geometry, and waveform design, as well as SHV, AHV, PCSHV, and QSHV transmit schemes. The combination of the most current techniques for weather simulation with this level of detail and flexibility in modeling radar systems allows for realistic emulation of the challenges and mitigation techniques that have been theorized for PPAR weather observation.

In order to demonstrate the utility of the simulator and provide some insight into aspects of bias mitigation techniques that had largely remained unexamined, a set of simulated experiments were carried out to study the Z_{DR} measurement performance of the PCSHV and CM cross-polar bias mitigation methods. The first experiment compared the performance of these two techniques on an untilted array, and one with a typical mechanical elevation tilt of 10°. The results highlighted the notable sensitivity of residual errors in the PCSHV method to mechanical tilt on the array face. The second experiment set out to characterize the deleterious effects of random error in the antenna pattern measurements used to formulate correction matrices. The results demonstrated the necessity for precise antenna characterization in any attempt to implement the CM bias mitigation method.

6.2 Recommendations for Future Work

6.2.1 Simulator Development

There are a number of potential improvements to the simulator that could be made in the course of future work. One limitation of the current framework is the fact that the simulator models transmitted signals as single complex values in order to generate time series signals more directly. Waveform design is accounted for in the simulator through precalculation of a range weighting function that is applied to the scatterers within each resolution volume. While the current approach offers major reductions in computational demand, it also severely limits the ability of the simulator

to model system configurations that feature waveform diversity, such as multiple-input and multiple-output (MIMO) techniques (Li and Stoica 2007), or the use of waveform design to gain isolation between array faces (Kurdzo et al. 2015) or polarizations (Pezeshki et al. 2008). Consequently, significant architectural changes would be needed to accurately simulate waveform diversity. One possible implementation, which would retain the current system of modeling transmitted signals as single values, would be to run a separate simulation for each transmitted waveform. Every waveform would have its own range weighting function, and the cross-correlation between each given waveform and all other waveforms would be precalculated and used during simulation to accurately model the cross-talk between transmitted signals. An alternative would be to change the simulation architecture, such that the transmitted signal is modeled not as a single complex value, but as a densely sampled baseband waveform. Each transmitted waveform would be phase shifted and attenuated through the simulator's model of transmission, backscattering, and reception, much like the complex excitation values V_{H} and V_{V} in the current architecture. However, each received waveform would also need to be appropriately time delayed based on 2-way propagation time to compose the received signal (an operation corresponding to the division of the scatterers into range gates when simulating using a single-value transmitted signal). The results of this operation for all waveforms would be summed to form a single composite signal. A matched filtering operation would then be performed for each waveform to produce separate streams of time-series values. This operation would eliminate the need to precalculate range weighting functions for each waveform and cross-correlations for each waveform pair.

Additionally, there are a pair of limitations related to the forward operator used to derive radar observable parameters from the ARPS model data. The first is the use of fixed closed-form expressions to determine the scattering characteristics of hydrometeors. The equations from Jung et al. (2008) used to calculate Z_{H}, Z_{V}, and K_{DP} contain constants derived from T-matrix calculations at S-band. Therefore, the simulator will not accurately reflect non-Rayleigh scattering effects that would occur at shorter operating wavelengths. The same limitation exists for the Rayleigh-Gans assumption used to calculate $|\rho_{\mathrm{HV}}(0)|$. In order to accurately study polarimetric signatures of rain at shorter wavelengths, or of very large hydrometeors at S-band, the simulator could be modified to allow for radar observable calculations based on user-provided scattering parameter data. The second forward operator limitation is the highly constrained DSD model. In order to improve the accuracy of the polarimetric signatures derived from the model data, the fixed-intercept, single-moment variant of the constrained gamma DSD currently in use could be replaced with the more flexible and more widely utilized 2-moment form (Ulbrich 1983). While the current version of the simulator is very useful for characterizing the effects of system design on the accurate measurement of Z_{DR}, ϕ_{DP}, and $|\rho_{\mathrm{HV}}(0)|$, improvements to the forward operator should be strongly considered before utilizing the simulator to estimate the effects of system design on the accuracy of microphysical information retrieval (such as the performance of QPE, HCAs, or DSD retrieval algorithms). Any study of HCA performance using this simulator would also, of course, mandate an expansion of the weather model to include a variety of hydrometeor types other than rain. Finally, it would undoubtedly be of interest to implement an attenuation model, both to obtain

more realistic performance data, and to allow for the study of attenuation correction through the use of polarimetric products obtained by PPARs.

6.2.2 Simulator Applications

There are many possibilities for future quantitative studies using this simulation framework. One of the most obvious is a thorough evaluation and comparison of biases incurred in polarimetric products (including $|\rho_{\mathrm{HV}}(0)|$ and ϕ_{DP}) that occur when using correction methods beyond just the CM and PCSHV methods. Even for those two methods, the investigation carried out in Chapter 5 was relatively limited in its depth. It did not investigate the effects on variance of polarimetric product estimates when using those methods, or their dependence on such factors as SNR, spectrum width, $|\rho_{\mathrm{HV}}(0)|$, or gradients in reflectivity in the field of observed weather. All of these are worthy subjects of investigation. Similarly, the studies conducted here utilized only a single weather scenario and set of element patterns. For a more complete characterization of the methods presented, these parameters could also be varied in order to study the variation in biases with cross-polar isolation in the radiating element, as well as dependencies on the structure of the observed weather.

Studies could also be carried out to investigate the effects of copolar mismatch and methods for quantifying and mitigating its effects. While much has been made of the problem of cross-polar biases, the fact that real antennas do not have perfectly matched copolar radiation patterns presents a non-trivial technical challenge. Another possibility is that the simulator could be used to evaluate polarimetric array

calibration procedures, which are another area of open investigation in PPAR development. The ability to generate time series data for individual elements could also be used to explore the possibilities of advanced beamforming with PPARs. Finally, the simulator could be utilized to develop a system for effectively benchmarking PPAR data quality through comparisons with a colocated parabolic dish with a significantly different beamwidth. Such a procedure would promise to be extremely useful in evaluating the performance of the first experimental PPARs.

In summary, there is a wide variety of open questions remaining with regard to the development of effective polarimetric phased array radars. Efforts to better answer many of these questions could benefit by leveraging a simulation framework such as the one presented herein. PPAR observations of realistic weather are difficult to model analytically, as they combine the complexities of the radar system itself with those of an inhomogenous, dynamic field of scatterers. Any attempt to quantify such a scenario mathematically realistically requires a large number of simplifying assumptions. As such, it is extremely helpful to have a method of verifying the validity of those assumptions through numerical simulation. Field experiments are also invaluable in that regard, and will ultimately provide the final validation for solutions to any of the technical problems presented by PPARs. However, the construction of new PPARs and the process of conducting field experiments is both costly and time consuming. Furthermore, there is no way to access, manipulate, or replicate "ground truth" values for real weather. Therefore, numerical simulations can and should play an important role is assisting the design of new systems and experiments, as well as in the verification of experimental results.

Bibliography

Anagnostou, E. N. and W. F. Krajewski, 1997: Simulation of radar reflectivity fields: Algorithm formulation and evaluation. *Water Resources Research*, **33**, 1419–1428.

Augros, C., O. Caumont, V. Ducrocq, and P. Tabary, 2013: Development and validation of a full polarimetric radar simulator. *36th Conference on Radar Meteorology, Breckenridge, Colorado, Amer. Meteor. Soc*, volume 387.

Balanis, C. A., 2016: *Antenna theory: analysis and design*. John Wiley & Sons, Inc.

Barratt, P. and I. C. Browne, 1953: A new method for measuring vertical air currents. *Quarterly Journal of the Royal Meteorological Society*, **79**, 550.

Bhattacharyya, A. K., 2006: *Phased array antennas: Floquet analysis, synthesis, BFNs and active array systems*, volume 179. John Wiley & Sons.

Bluestein, H. B., M. M. French, I. Popstefanija, R. T. Bluth, and J. B. Knorr, 2010: A mobile, phased-array Doppler radar for the study of severe convective storms. *Bull. Amer. Meteor. Soc.*, **91**, 579–600.

Booker, H. G. and Others, 1946: Slot aerials and their relation to complementary wire aerials (Babinet's principle). *J. IEE*, **93**, 620–626.

Brandes, E. A., G. Zhang, and J. Vivekanandan, 2002: Experiments in rainfall estimation with a polarimetric radar in a subtropical environment. *Journal of Applied Meteorology*, **41**, 674–685.

Breit, G. and M. A. Tuve, 1926: A test of the existence of the conducting layer. *Physical Review*, **28**, 554.

Bringi, V. N. and V. Chandrasekar, 2001: *Polarimetric Doppler Weather Radar: Principles and Applications*. Cambridge University Press.

Bringi, V. N., T. D. Keenan, and V. Chandrasekar, 2001: Correcting C-band radar reflectivity and differential reflectivity data for rain attenuation: A self-consistent method with constraints. *Geoscience and Remote Sensing, IEEE Transactions on*, **39**, 1906–1915.

Button, K. J., 1984: Microwave ferrite devices: The first ten years. *Microwave Theory and Techniques, IEEE Transactions on*, **32**, 1088–1096.

Byrd, A. D., I. R. Ivic, R. D. Palmer, B. M. Isom, B. L. Cheong, A. D. Schenkman, and M. Xue, 2016: A Weather Radar Simulator for the Evaluation of Polarimetric Phased Array Performance. *IEEE Transactions on Geoscience and Remote Sensing*, **In press.**

Capsoni, C. and M. D'Amico, 1998: A physically based radar simulator. *Journal of Atmospheric and Oceanic ...*, **15**, 593–598.

Capsoni, C., M. D'Amico, and R. Nebuloni, 2001: A multiparameter polarimetric radar simulator. *Journal of Atmospheric and Oceanic Technology*, **18**, 1799–1809.

Caumont, O., V. Ducrocq, G. Delrieu, M. Gosset, J.-P. Pinty, J. du Châtelet, H. Andrieu, Y. Lemaître, and G. Scialom, 2006: A radar simulator for high-resolution nonhydrostatic models. *Journal of Atmospheric and Oceanic Technology*, **23**, 1049–1067.

Chandrasekar, V. and N. Bharadwaj, 2009: Orthogonal channel coding for simultaneous co- and cross-polarization measurements. *Journal of Atmospheric and Oceanic Technology*, **26**, 45–56.

Chandrasekar, V. and V. N. Bringi, 1987: Simulation of radar reflectivity and surface measurements of rainfall. *Journal of Atmospheric and Oceanic Technology*, **4**, 464–478.

Cheong, B., R. Palmer, and C. Curtis, 2008a: Refractivity retrieval using the phased-array radar: First results and potential for multimission operation. *and Remote Sensing ....*

Cheong, B. L., M. W. Hoffman, and R. D. Palmer, 2004: Efficient atmospheric simulation for high-resolution radar imaging applications. *Journal of Atmospheric and Oceanic Technology*, **21**, 374–378.

Cheong, B. L., R. D. Palmer, and M. Xue, 2008b: A time series weather radar simulator based on high-resolution atmospheric models. *Journal of Atmospheric and Oceanic Technology*, **25**, 230–243.

Deschamps, G. A., 1953: Microstrip microwave antennas. *Third USAF symposium on Antennas*, volume 84.

Doviak, R. J., V. Bringi, A. Ryzhkov, A. Zahrai, and D. Zrnic, 2000: Considerations for polarimetric upgrades to operational WSR-88D radars. *Journal of Atmospheric and Oceanic Technology*, **17**, 257–278.

Doviak, R. J., L. Lei, G. Zhang, J. Meier, and C. Curtis, 2011: Comparing theory and measurements of cross-polar fields of a phased-array weather radar. *Geoscience and Remote Sensing Letters, IEEE*, **8**, 1002–1006.

Doviak, R. J. and D. S. Zrnić, 2006: *Doppler Radar & Weather Observations*. Dover Publications, Inc.

Forsyth, D. E., J. F. Kimpel, D. S. Zrnic, R. Ferek, J. F. Heimmer, T. McNellis, J. E. Crain, A. M. Shapiro, R. J. Vogt, and W. Benner, 2005: The National Weather Radar Testbed (Phased-Array). *32nd Conference on Radar Meteorology*, 24–29.

Friis, H. T., 1925: A new directional receiving system. *Radio Engineers, Proceedings of the Institute of*, **13**, 685–707.

Friis, H. T. and C. B. Feldman, 1937: A multiple unit steerable antenna for short-wave reception. *Radio Engineers, Proceedings of the Institute of*, **25**, 841–917.

Fulton, C. and W. Chappell, 2010: Calibration of panelized polarimetric phased array radar antennas: A case study. *2010 IEEE International Symposium on Phased Array Systems and Technology*, IEEE, 860–867.

Fulton, C., J. Salazar, Y. Zhang, G. Zhang, R. Kelley, J. Meier, M. McCord, D. Schmidt, A. D. Byrd, L. M. Bhowmik, S. Karimkashi, D. S. Zrnić, R. J. Doviak, A. Zahrai, M. Yeary, and R. Palmer, 2016: Cylindrical Polarimetric Phased Array Radar (CPPAR): Beamforming and Calibration for Weather Applications. *In Preparation*.

Fulton, C. J., 2011: *Digital Array Radar Calibration and Performance Monitoring Techniques for Direct Conversion and Dual Polarization Architectures*. Ph.D. thesis, Purdue University.

Galati, G. and G. Pavan, 1995: Computer simulation of weather radar signals. *Simulation Practice and Theory*, **3**, 17–44.

Ge, L. and K. M. Luk, 2012: A low-profile magneto-electric dipole antenna. *Antennas and Propagation, IEEE Transactions on*, **60**, 1684–1689.

—, 2015: A Three-Element Linear Magneto-Electric Dipole Array With Beamwidth Reconfiguration. *Antennas and Wireless Propagation Letters, IEEE*, **14**, 28–31.

Giangrande, S. E. and A. V. Ryzhkov, 2008: Estimation of rainfall based on the results of polarimetric echo classification. *Journal of Applied Meteorology and Climatology*, **47**, 2445–2462.

Giuli, D., L. Facheris, M. Fossi, and A. Rossettini, 1990: Simultaneous scattering matrix measurement through signal coding. *Radar Conference, 1990., Record of the IEEE 1990 International*, IEEE, 258–262.

Giuli, D., L. Facheris, and A. Freni, 1993a: Integrated model for simulation of dual linear polarisation radar measurement fields. *IEEE Proceedings F (Radar and Signal Processing)*, IET, volume 140, 223–232.

Giuli, D., M. Fossi, and L. Facheris, 1993b: Radar target scattering matrix measurement through orthogonal signals. *Radar and Signal Processing, IEE Proceedings F*, IET, volume 140, 233–242.

Green, A. W., 1975: An approximation for the shapes of large raindrops. *Journal of Applied Meteorology*, **14**, 1578–1583.

Haase, G. and S. Crewell, 2000: Simulation of radar reflectivities using a mesoscale weather forecast model. *Water Resources Research*, **36**, 2221–2231.

Holdsworth, D. A. and I. M. Reid, 1995: A simple model of atmospheric radar backscatter: Description and application to the full correlation analysis of spaced antenna data. *Radio Science*, **30**, 1263–1280.

Ishimaru, A., 1978: *Wave propagation and scattering in random media*, volume 2. Academic press New York.

Isom, B., R. Palmer, R. Kelley, J. Meier, D. Bodine, M. Yeary, B.-L. Cheong, Y. Zhang, T.-Y. Yu, and M. I. Biggerstaff, 2013: The Atmospheric Imaging Radar: Simultaneous volumetric observations using a phased array weather radar. *Journal of Atmospheric and Oceanic Technology*, **30**, 655–675.

Ivić, I. and R. J. Doviak, 2016: Evaluation of Phase Coding to Mitigate Differential Reflectivity Bias in Polarimetric {PAR}. *Geoscience and Remote Sensing, IEEE Transactions on*, **54**, 431–451.

Ivić, I. and D. S. Zrnić, 2013: Statistical evaluation of pulse to pulse phase coding to suppress coupling in the polarimetric radar. *36th Conference on Radar Meteorology, Breckenridge, Colorado, Amer. Meteor. Soc.*

Ivić, I. R., 2015: Statistical Evaluation of Time Multiplexing to Mitigate Differential Reflectivity Bias Due to Cross-Polar Coupling. *Journal of Atmospheric and Oceanic Technology*.

—, 2016: An Approach to Simulate the Effects of Antenna Patterns on Polarimetric Variable Estimates.

Ivić, I. R. and A. D. Byrd, 2015: A first look at the MPAR dual-polarization phased-array-radar mobile demonstrator. *AMS 37th Conference on Radar Meteorology*.

Jung, Y., G. Zhang, and M. Xue, 2008: Assimilation of simulated polarimetric radar data for a convective storm using the ensemble Kalman filter. Part I: Observation operators for reflectivity and polarimetric variables. *Monthly Weather Review*, **136**, 2228–2245.

Krajewski, W. F., R. Raghavan, and V. Chandrasekar, 1993: Physically based simulation of radar rainfall data using a space–time rainfall model. *Journal of Applied Meteorology*, **32**, 268–283.

Kurdzo, J. M., R. D. Palmer, B. L. Cheong, and M. E. Weber, 2015: Adaptive Waveform Design for Multi-Sector Array Isolations.

Lei, L., G. Zhang, and R. J. Doviak, 2013: Bias correction for polarimetric phased-array radar with idealized aperture and patch antenna elements. *Geoscience and Remote Sensing, IEEE Transactions on*, **51**, 473–486.

Li, J. and P. Stoica, 2007: MIMO radar with colocated antennas. *Signal Processing Magazine, IEEE*, **24**, 106–114.

Li, Z., Y. Zhang, G. Zhang, K. Brewster, and Others, 2011: A microphysics-based simulator for advanced airborne weather radar development. *Geoscience and Remote Sensing, IEEE Transactions on*, **49**, 1356–1373.

Lin, Y.-L., R. D. Farley, and H. D. Orville, 1983: Bulk parameterization of the snow field in a cloud model. *Journal of Climate and Applied Meteorology*, **22**, 1065–1092.

Lischi, S., A. Lupidi, M. Martorella, F. Cuccoli, L. Facheris, and L. Baldini, 2014: Advanced polarimetric Doppler weather radar simulator. *Radar Symposium (IRS), 2014 15th International*, IEEE, 1–6.

Ludwig, A., 1973: The definition of cross polarization. *IEEE Transactions on Antennas and Propagation*, **21**, 116–119.

Lupidi, A., C. Moscardini, A. Garzelli, F. Berizzi, F. Cuccoli, and M. Bernabò, 2011: Polarimetry applied to avionic weather radar: Improvement on meteorological phenomena detection and classification. *Digital Communications - Enhanced Surveillance of Aircraft and Vehicles (TIWD/ESAV), Tyrrhenian International Workshop on*, Capri, Italy, 73–77.

May, R. M., 2014: *Estimating and Mitigating Errors in Dual-polarization Radar Attenuation Correction*. Ph.D. thesis, University of Oklahoma.

May, R. M., M. I. Biggerstaff, and M. Xue, 2007: A Doppler radar emulator with an application to the detectability of tornadic signatures. *Journal of Atmospheric and Oceanic Technology*, **24**, 1973–1996.

Muschinski, A., P. P. Sullivan, D. B. Wuertz, R. J. Hill, S. A. Cohn, D. H. Lenschow, and R. J. Doviak, 1999: First synthesis of wind-profiler signals on the basis of large-eddy simulation data. *Radio Science*, **34**, 1437–1459.

Newell, R. E. and S. G. Geotis, 1955: *Meteorological measurements with a radar provided with variable polarization*. MIT Department of Meteorology.

Orzel, K., 2015: X-band Dual Polarization Phased-Array Radar for Meteorological Applications.

Pang, C., P. Hoogeboom, F. Le Chevalier, H. W. J. Russchenberg, J. Dong, T. Wang, and X. Wang, 2016: Polarimetric Bias Correction of Practical Planar Scanned Antennas for Meteorological Applications. *IEEE Transactions on Geoscience and Remote Sensing*, **54**, 1488–1504.

Pezeshki, A., W. Moran, S. D. Howard, and Others, 2008: Doppler resilient Golay complementary waveforms. *Information Theory, IEEE Transactions on*, **54**, 4254–4266.

Richards, M. A., 2005: *Fundamentals of radar signal processing*. Tata McGraw-Hill Education.

Ryzhkov, A. V., S. E. Giangrande, and T. J. Schuur, 2005: Rainfall estimation with a polarimetric prototype of {WSR-88D}. *Journal of Applied Meteorology*, **44**, 502–515.

Ryzhkov, A. V. and D. S. Zrnić, 1995: Comparison of dual-polarization radar estimators of rain. *Journal of Atmospheric and Oceanic Technology*, **12**, 249–256.

Sachidananda, M. and D. S. Zrnić, 1986: Differential propagation phase shift and rainfall rate estimation. *Radio Science*, **21**, 235–247.

—, 1987: Rain rate estimates from differential polarization measurements. *Journal of Atmospheric and Oceanic Technology*, **4**, 588–598.

—, 1989: Efficient processing of alternately polarized radar signals. *Journal of Atmospheric and Oceanic Technology*, **6**, 173–181.

Sánchez-Barbetty, M., R. W. Jackson, and S. Frasier, 2012: Interleaved sparse arrays for polarization control of electronically steered phased arrays for meteorological applications. *Geoscience and Remote Sensing, IEEE Transactions on*, **50**, 1283–1290.

Sarkar, T. K., R. J. Mailloux, A. A. Oliner, M. Salazar-Palma, and D. L. Sengupta, 2006: *A History of Phased Array Antennas*, John Wiley & Sons, Inc. 567–603.

Seliga, T. A., K. Aydin, and H. Direskeneli, 1986: Disdrometer measurements during an intense rainfall event in central Illinois: Implications for differential reflectivity radar observations. *Journal of climate and applied meteorology*, **25**, 835–846.

Seliga, T. A. and V. N. Bringi, 1976: Potential use of radar differential reflectivity measurements at orthogonal polarizations for measuring precipitation. *Journal of Applied Meteorology*, **15**, 69–76.

—, 1978: Differential reflectivity and differential phase shift: Applications in radar meteorology. *Radio Science*, **13**, 271–275.

Skolnik, M. I., 2001: Radar handbook.

Snyder, J. C., H. B. Bluestein, G. Zhang, and S. J. Frasier, 2010: Attenuation correction and hydrometeor classification of high-resolution, X-band, dual-polarized mobile radar measurements in severe convective storms. *Journal of Atmospheric and Oceanic Technology*, **27**, 1979–2001.

Straka, J. M., D. S. Zrnić, and A. V. Ryzhkov, 2000: Bulk Hydrometeor Classification and Quantification Using Polarimetric Radar Data: Synthesis of Relations. *J. Appl. Meteor. Climatol.*, **39**, 1341–1372.

Swords, S. S., 1986: Technical History of the Beginnings of RADAR. Institution of Electrical Engineers.

Tesla, N., 1900: The problem of increasing human energy. *Century Magazine*, **LX**, 175–211.

Testud, J., E. Le Bouar, E. Obligis, and M. Ali-Mehenni, 2000: The rain profiling algorithm applied to polarimetric weather radar. *Journal of Atmospheric and Oceanic Technology*, **17**, 332–356.

Torres, S. M., 2001: *Estimation of Doppler and Polarimetric Variables for Weather Radars*. Ph.D. thesis, University of Oklahoma.

Ulbrich, C. W., 1983: Natural variations in the analytical form of the raindrop size distribution. *Journal of Climate and Applied Meteorology*, **22**, 1764–1775.

Van de Hulst, H. C., 2012: *Light scattering by small particles*. Courier Corporation.

Venkatesh, V. and S. J. Frasier, 2013: Simulation of Spaced Antenna Wind Retrieval Performance on an X-Band Active Phased Array Weather Radar. *Journal of Atmospheric and Oceanic Technology*, **30**, 1447–1459.

Vivekanandan, J., S. M. Ellis, R. Oye, D. S. Zrnić, A. V. Ryzhkov, and J. Straka, 1999: Cloud microphysics retrieval using S-band dual-polarization radar measurements. *Bulletin of the american meteorological society*, **80**, 381–388.

Wang, Q. and Q.-Q. He, 2010: An arbitrary conformal array pattern synthesis method that include mutual coupling and platform effects. *Progress In Electromagnetics Research*, **110**, 297–311.

Watson-Watt, R., 1957: *Three steps to victory*. Odhams Press.

Weber, M. E., J. Y. N. Cho, J. S. Herd, J. M. Flavin, W. E. Benner, and G. S. Torok, 2007: The next-generation multimission US surveillance radar network. *Bulletin of the American Meteorological Society*, **88**, 1739–1751.

Whiton, R. C., P. L. Smith, S. G. Bigler, K. E. Wilk, and A. C. Harbuck, 1998a: History of operational use of weather radar by US weather services. Part I: the pre-NEXRAD era. *Weather and Forecasting*, **13**, 219–243.

—, 1998b: History of operational use of weather radar by US weather services. Part II: Development of operational Doppler weather radars. *Weather and forecasting*, **13**, 244–252.

Wu, B. Q. and K.-M. Luk, 2009: A broadband dual-polarized magneto-electric dipole antenna with simple feeds. *Antennas and Wireless Propagation Letters, IEEE*, **8**, 60–63.

Xue, M., K. K. Droegemeier, and V. Wong, 2000: The Advanced Regional Prediction System (ARPS)–A multi-scale nonhydrostatic atmospheric simulation and prediction model. Part I: Model dynamics and verification. *Meteorology and atmospheric physics*, **75**, 161–193.

Xue, M., K. K. Droegemeier, V. Wong, A. Shapiro, K. Brewster, F. Carr, D. Weber, Y. Liu, and D. Wang, 2001: The Advanced Regional Prediction System (ARPS)– A multi-scale nonhydrostatic atmospheric simulation and prediction tool. Part II: Model physics and applications. *Meteorology and atmospheric physics*, **76**, 143–165.

Xue, M., M. Hu, and A. D. Schenkman, 2014: Numerical prediction of the 8 May 2003 Oklahoma City tornadic supercell and embedded tornado using ARPS with the assimilation of WSR-88D data. *Weather and Forecasting*, **29**, 39–62.

Xue, M., D. Wang, J. Gao, K. Brewster, and K. K. Droegemeier, 2003: The Advanced Regional Prediction System (ARPS), storm-scale numerical weather prediction and data assimilation. *Meteorology and Atmospheric Physics*, **82**, 139–170.

Zahrai, A. and D. S. Zrnić, 1993: The 10-cm-wavelength polarimetric weather radar at NOAA's National Severe Storms Laboratory. *Journal of Atmospheric and Oceanic Technology*, **10**, 649–662.

Zhang, G., 2016: Weather Radar Polarimetry with MATLAB.

Zhang, G., R. Doviak, D. Zrnic, and J. Crain, 2008: Phased array radar polarimetry for weather sensing: Challenges and opportunities. *Geoscience and Remote Sensing Symposium, 2008. IGARSS 2008. IEEE International*, IEEE, volume 5, V—-449.

Zhang, G., R. J. Doviak, D. S. Zrnic, J. Crain, D. Staiman, and Y. Al-Rashid, 2009: Phased array radar polarimetry for weather sensing: A theoretical formulation for bias corrections. *Geoscience and Remote Sensing, IEEE Transactions on*, **47**, 3679–3689.

Zhang, G., R. J. Doviak, D. S. Zrnic, R. Palmer, L. Lei, and Y. Al-Rashid, 2011: Polarimetric phased-array radar for weather measurement: A planar or cylindrical configuration? *Journal of Atmospheric and Oceanic Technology*, **28**, 63–73.

Zhang, G., J. Vivekanandan, and E. Brandes, 2001: A method for estimating rain rate and drop size distribution from polarimetric radar measurements. *Geoscience and Remote Sensing, IEEE Transactions on*, **39**, 830–841.

Zrnić, D. S., 1975: Simulation of weatherlike Doppler spectra and signals. *Journal of Applied Meteorology*, **14**, 619–620.

Zrnić, D. S., R. Doviak, G. Zhang, and A. Ryzhkov, 2010: Bias in differential reflectivity due to cross coupling through the radiation patterns of polarimetric weather radars. *Journal of Atmospheric and Oceanic Technology*, **27**, 1624–1637.

Zrnić, D. S., R. J. Doviak, V. M. Melnikov, and I. R. Ivić, 2014: Signal design to suppress coupling in the polarimetric phased array radar. *Journal of Atmospheric and Oceanic Technology*, **31**, 1063–1077.

Zrnić, D. S., J. F. Kimpel, D. E. Forsyth, A. Shapiro, G. Crain, R. Ferek, J. Heimmer, W. Benner, T. J. McNellis, and R. J. Vogt, 2007: Agile-beam phased array radar for weather observations. *Bulletin of the American Meteorological Society*, **88**, 1753–1766.

Zrnić, D. S., V. Melnikov, and R. Doviak, 2012: Issues and challenges for polarimetric measurement of weather with an agile beam phased array radar. *NOAA/NSSL Report*.

Zrnić, D. S., A. Ryzhkov, J. Straka, Y. Liu, and J. Vivekanandan, 2001: Testing a procedure for automatic classification of hydrometeor types. *Journal of Atmospheric and Oceanic Technology*, **18**, 892–913.

Zrnić, D. S., G. Zhang, and R. J. Doviak, 2011: Bias correction and Doppler measurement for polarimetric phased-array radar. *Geoscience and Remote Sensing, IEEE Transactions on*, **49**, 843–853.